Star Formation in Molecular Clouds Associated with H II Regions

by

Mohaddesseh Azimlu Shanjani

A thesis
presented to the University of Waterloo
in fulfillment of the
thesis requirement for the degree of
Doctor of Philosophy
in
Physics

Waterloo, Ontario, Canada, 2009

I hereby declare that I am the sole author of this thesis. This is a true copy of the thesis, including any required final revisions, as accepted by my examiners.

I understand that my thesis may be made electronically available to the public.

Abstract

We have studied the properties of molecular clouds and the stellar population associated with 10 H II regions. We used the James Clerk Maxwell Telescope (JCMT) to make ^{12}CO(2-1) maps in order to study the structure of the cloud and to identify the dense clumps within the cloud. In half of our sources we found that molecular gas appears to have been pushed and compressed into the shells around the expanding ionized gas and fragmented into clumps. Most of these clumps have higher temperature and density compared to the other clumps within the mapped regions. We made pointed observations in ^{13}CO(2-1) and CS(5-4) at the peak of ^{12}CO(2-1) within each clump to measure and calculate the physical properties of the clumps such as line width, excitation temperature, density and mass. Two gas components were selected in the cloud associated with S175 to investigate the influence of the H II region on the molecular gas: S175A is adjacent to the ionization fronts and probably affected by the expanding H II region while S175B is too distant to be affected. Contrary to our expectation S175B was a turbulent region with broadened line profiles. We made a sub-map in ^{12}CO(3-2) using HARP at the JCMT to search for the source of turbulence and identified a proto-stellar outflow in S175B.

We examined the relationship between gas parameters derived for the clumps within the entire sample. The identified clumps were found to be divided into two categories: "type I" sources in which we can find a relationship between size and line width and "type II" sources where there is no relation. We found

that the power law indices for type I sources are generally larger than the previous studies. Larger line widths and consequently larger indices seems to be an initial environmental characteristic of massive star forming regions

We found that mass and column density increase with line width for both type I and type II sources. We did not find any relation between the size and column density. The influence of the H II region on temperature and line widths was examined and we found that the temperature decreases with distance from the ionized fronts but no change was found for the line width. Although most of the clumps within the compressed shells around the H II region have generally larger line widths, from this test we may conclude that the internal dynamics of the cloud beyond the compressed shells is not much influenced by the expanding H II region.

Finally, our near IR study of the stellar populations using 2MASS data, shows that in half of the regions the exciting star belongs to a cluster. We also found that star formation is consistent with triggering by the expansion of the ionized gas in some of sources in our sample. At least two young embedded clusters have been identified at the same position as the dense clumps within fragmented shells around H II regions. These clumps have high temperature and density and large line widths. We identify some other hot and dense clumps very similar in molecular gas properties as candidates of cluster or massive star formation.

Most of the active star forming regions associated with H II regions have a

population of massive newborn stars compared to a star forming cloud which is distant from the massive star and the ionized gas. We conclude that more massive stars form in the molecular cloud at the peripheries of H II regions but it is not clear f this is a result of the initial conditions that have formed the massive, exciting star of the H II region or a feedback of the massive star itself and the expanding H II region.

Acknowledgements

I would like to acknowledge the help and guidance of my supervisor, Dr. Michel Fich. I would also like to thank Drs. Gretchen Harris, Michael Balogh, Naomi Nishimura and Carolyn M^{c}Coey whose helpful advice and support during past four years were always encouraging. I thank Drs. Martin Houde and Arsen Hajian to be external examiners in my defense session and for their useful advices. The JCMT observatory staff, especially Ming Zhu, Gerald Schieven and Jan Wouterloot are thanked for their support during the observations and their helpful assistance to reduce data.

I thank my friends and family for their support and encouragement. Without them I could never have this accomplishment. Finally I thank Judy McDonnell, Linda Stadig and other administrative staff who were always welcoming.

When my friends and family were making green flags and participated in rallies around the world to support the Green movement in Iran, I was writing my thesis. When they were signing the green scroll to support peace and freedom, I was writing my thesis and the spot of my signature remained empty. When they had vigil around the world in memory of Neda and other martyrs, I burned a candle in balcony, came back to my desk and kept writing. This work belongs to all those people who take a role in supporting freedom and peace all around the world.

Contents

List of Tables

List of Figures

Chapter 1

Introduction

Stars, these sparkling tiny points have been studied for thousands of years. In ancient Greece, constellations were created after the gods, goddesses and other mythological characters who were believed to govern our universe. They were later used as guide points. Stargazing and astrometry, developed in the Islamic astronomy period, became the most accurate method in navigation and thus most of the bright stars are known by their Arabic names.

Modern astronomy was started by the Copernicus heliocentric model which changed our image of the universe. Moving the centre of the universe from the Earth to the Sun made it easier to explain the complicated movements of the planets on the solid background of stars. It was the time for Kepler to formulate the laws that govern the orbits of moving objects. It was all an incredible achievement, but the nature of the universe and celestial objects

within it remained a mystery until the optical revolution by large telescopes. By the twentieth century our picture of the universe had expanded beyond the borders of the Milky Way. New technology and instrumentation provided the opportunity to look beyond the visible universe and discover the invisible face of the nature in a wide range of electromagnetic wavelengths from radio emissions to energetic gamma rays. Our knowledge of the universe through these new windows increased dramatically and many new kinds of celestial objects and features which could never be observed in optical wavelengths, were detected in radio emission and infrared.

Most of the universe, such as hydrogen molecular clouds, is made up of cold regions that do not emit in visible light. To study these regions we need to use longer electromagnetic wavelengths such as radio or infrared. Figure 1.1 compares the Orion constellation area in visible light and infrared. These images show a large amount of gas containing star-forming regions and many proto-stars that cannot be seen by optical telescopes.

A new generation of ground based and space telescopes opened new eyes on studying the cold gaseous regions in the Milky Way and other galaxies. In addition, new instruments such as spectrometers in different wave bands, made it possible to get detailed information about the physical properties and chemical compositions of various regions in the universe from the atmosphere of planets in solar system to the most distant galaxies.

This precious information brought us back to the essential questions: how

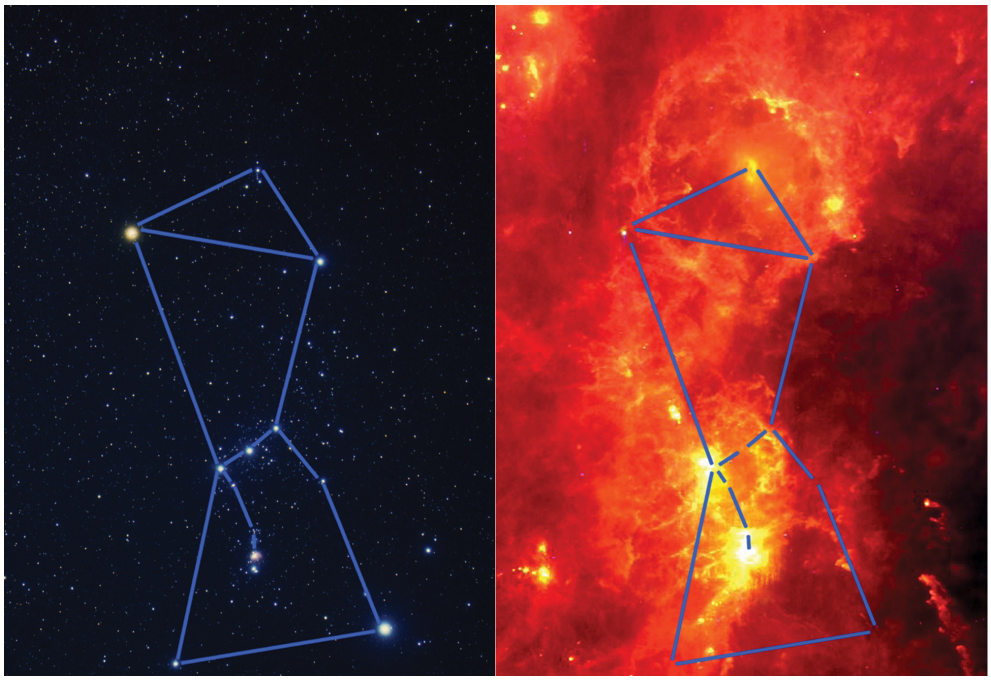

Figure 1.1 The visible light (left) and infrared (right) images of the constellation Orion shown here are of the exact same area. These images dramatically illustrate how features that cannot be seen in visible light appear very bright in the infrared. (Credits: Visible light image: Akira Fujii; infrared image: AKARI, infrared Astronomical Satellite)

is the universe formed and how does it evolve? What makes the variety in galaxies morphology? What is the origin of stars and how do they produce energy? Thanks to both theoretical and observational astronomers we now have developed models of the universe (rather than a turtle standing on the back of four elephants!) and we are looking for the nature of the dark matter and dark energy. We know stars originate in molecular hydrogen (H_2) clouds and that most of the elements in our planet and our body have been formed through nuclear reactions in massive stars or during their dramatic death as supernovae. Yet the complicated process of star formation remains as a basic problem in astronomy.

The initial physical conditions of the molecular clouds determine the star formation process, rate and efficiency. Stars may form individually or within clusters. The process is strongly dependent on the mass of the star. Low mass stars (a few solar masses or smaller) may form in isolation or within clusters of stars. Massive stars (8 solar mass or larger) are believed mostly to form in clustered environments (e.g Smith et al., 2009, Lada & Lada 2003). In different studies, intermediate mass stars may be considered in a separate category or just considered as low mass stars (Lada & Lada, 2003 and references therein). Like massive stars, the process that produces intermediate mass stars is not very well understood.

Theoretical models are more developed for isolated star formation and the observation of individual collapsing cores is almost consistent with theory (Har-

tigan et al. 1995, Reipurth & Bally 2001). Clustered star formation is more complicated and therefore less well understood theoretically. Massive stars are believed to form in Giant Molecular Clouds (GMCs) in rich clusters formed in dense, massive, turbulent clumps. Unfortunately such regions are much less common than the low mass star-forming regions and consequently fewer in number in nearby clouds. Therefore, the detailed study of high mass star formation is demanding compared to the study of low mass stars.

It is not only the molecular clouds that govern star formation. Newborn stars also affect their original environment by feedbacks. Low mass stars form gently in more quiescent regions and do not significantly affect their environment during their slow formation and evolution process. By contrast, high mass stars form in turbulent dense cores and evolve very quickly (e.g. McKee & Tan 2003). They influence the environment through strong winds, jets and outflows which change physical conditions such as the temperature and density of the cloud. They also ionize the surrounding gas (forming an H II region) around the stars. Expansion of the ionized gas affects further star formation in the cloud and may cause the formation of more stars (e.g Deharveng et. al, 2005).

In this thesis we study the impact of H II regions on star formation in their associated molecular clouds. Molecular hydrogen gas in young star-forming regions is extremely cold and have no emission in optical wavelengths. Hydrogen is also a symmetric molecule and has no (electric/dipole) emission at low

temperatures. Molecular clouds are best studied in radio and sub-millimeter emission of other abundant tracers such as carbon monoxide (CO) which is the most abundant molecule after H_2 in star-forming regions. We use the 15 meter James Clerk Maxwell Telescope (JCMT) to investigate the structure and physical conditions of molecular clouds associated with a selected sample of 10 H II regions. We aim to understand how these conditions have been affected by the massive stars and how these conditions may affect future star formation.

The thesis is organized as follows. In the rest of this chapter I review the basics about molecular clouds, the physical conditions in various star-forming regions and current theories and observational results. Then I discuss the questions have been addressed in this thesis and how this work has improved our knowledge about the star formation process. Chapter 2 contains the data reduction methods and calculations. This chapter which is a reprint of a published paper, compares the physical characteristics of two identified components of the molecular cloud associated with S175 H II region: one near the massive star and partially over the H II region and the other distant enough that is unlikely to be influenced by the massive star and the H II region. Chapter 3 is a reprint of a paper being submitted which summarizes all derived parameters for the entire sample. In this paper we discuss the relation between different physical parameters and their variations within the sample. Stellar populations in the near infrared are presented in Chapter 4. In this study I determine how the stellar distribution is affected by the environmental conditions, especially

under influence of the massive star and the H II region.

1.1 Molecular Clouds: Birthplace of Stars

Stars are not the only objects seen in the dark night sky. For many years it has been noticed that there are some extended objects that could not be categorized as stars. All of these extended astronomical objects were originally called *nebulae*. Even galaxies beyond the Milky Way such as Andromeda were not distinguished from the Galactic clouds before Edwin Hubble identified them as huge complexes of stars and gas very far from us and moving away from us. Now the term nebula is used for extended interstellar gas and dust in various forms of size, mass, density and other physical conditions. The nebulae could be diffuse low density interstellar gas, a high density star-forming region, an expanding ring shape gas ejected by a red giant (planetary nebula) or remnants of a supernova explosion. In this chapter we discuss the physical properties of the Interstellar Medium (ISM) and its major components with special emphasize on the physical conditions of star-forming regions.

1.2 Interstellar Medium

New technology and larger telescopes have enabled us to look deeper and detect fainter objects in the universe. Yet there is lots of space between stars with

particle density much smaller than the best possible laboratory vacuum on the Earth, but still not empty. The ISM in the Milky Way is filled with mostly hydrogen gas (≈90% of mass) mixed with helium (≈9%), and 1% of other elements, molecules and dust particles. Some candidates of dust grain materials are silicates, carbonaceous material like graphite, amorphous or glassy carbon, polycyclic aromatic hydrocarbons (PAHs), chain-like hydrocarbons, silicon carbide (SiC) and carbonates (Draine 2003).

The early models classified the gas in the ISM into three categories: cold atomic hydrogen clouds, cold molecular hydrogen clouds and warm-hot ionized gas (e.g. McKee & Ostriker 1977). Its density varies in a wide range from 10^{-6} particles cm^{-3} in the hottest ionized regions to $\sim$ 10^{10} particle cm^{-3} in dense cores containing masers; these point to a very in-homogenous environment. These phases are thought to be in approximate pressure equilibrium with one another. Most of the ISM lies close to the galactic disc. It contains $\sim 10-15\%$ of the total mass of the Galactic disk but half of this mass is concentrated in dense clouds that occupy only one to two percent of the total interstellar volume (Ferriere 2001). Other authors have defined slightly different categories. Table 1.1 summarizes different types of the ISM and the property of each component, as given by Stahler & Palla (2004). The first column in this table shows different phases of interstellar medium and the second column is the volume particle number density. Note that the cold molecular gas that forms into stars makes up approximately 20% of the mass of the ISM but fills only one percent of the

Table 1.1. Phases of Interstellar Medium (ISM)

Phase	n_{tot} (cm^{-3})	T (K)	M ($10^9 M_\odot$)	f [a]
Molecular	> 300	10	2.0	0.01
Cold neutral	50	80	3.0	0.04
Warm neutral	0.5	8×10^3	4.0	0.30
Warm ionized	0.3	8×10^3	1.0	0.15
Hot ionized	3×10^{-3}	5×10^5	—	0.50

[a] f is the volume filling factor.

Note. — Table from Stahler & Palla (2004)

volume.

The Orion nebula is probably the most famous non-stellar object that is easily recognized by the naked eye in the winter sky. The Orion nebula is a cloud of hydrogen gas illuminated by a young embedded cluster of stars named the Trapezium. Some of these newborn stars are recognized even with a small telescope (Figure 1.2).

As discussed earlier, most of the stars, and especially massive stars, form in clusters. A huge amount of molecular hydrogen is required to form a stellar cluster such as the Trapezium. Thousands of such gas complexes known as Giant Molecular Clouds (GMCs) have been detected in the Milky Way. Each complex

Figure 1.2 Optical images reveal clouds of gas and dust in the Orion Nebula; an infrared image (right) reveals the new stars shining within. Credit: C. R. O'Dell-Vanderbilt University, NASA, and ESA.

has a total mass of $\sim 10^5$ $M_\odot$ (although a few are known with masses approaching 10^6 $M_\odot$) which is mainly molecular hydrogen. These clouds are very cold and cannot be observed in visible light. Some non-symmetric molecules like CO which are highly abundant and strongly emitting, are therefore the best tracers to investigate molecular clouds. Molecular clouds are mixed with tiny particles of silicate or carbonaceous material known as interstellar dust. The dust grains have typically a size of ~ 0.1 μm and absorb any light with wavelength smaller than their diameters. They radiate this absorbed energy in the infrared and sub-millimeter (for example Figure 1.1).

1.3 Molecular Clouds: Nature and Structure

The molecular cloud component of the ISM has a complicated structure and exists in a wide range of size, mass, density and other physical characteristics. Table 1.2 summarizes the physical properties of different Galactic molecular clouds. In this table A_V is the extinction caused by the gas in visible wavelength, n_{tot} gives the number of particles volume density, and L is the typical size of the cloud. In some cases, a large fraction of the cloud might have constant density and temperature while in most of the observed regions the structure is a complex of various cloud types. For example it may have an onion-like structure, with dense cloud material in the centre, surrounded by translucent gas, which is surrounded by a halo of diffuse gas (Snow & McCall 2006).

Interstellar molecules and atoms can be identified through their emission from orbital, vibrational, or rotational transitions. Typically, electronic transitions of simple molecules emit photons in the ultraviolet (UV) or visible light; vibrational transitions produce infrared wavelengths; and rotational lines are seen at millimeter, sub-millimeter and radio wavelengths. Therefore a wide range of observational techniques and instrumentation is required to study the entire molecular gas portion of the ISM.

Diffuse clouds are relatively isolated regions that contain both atomic and molecular hydrogen. The absorption of visible emission within diffuse clouds is

Table 1.2. Classification of interstellar cloud types and their physical properties.

Cloud Type	A_V mag	n_{tot} (cm^{-3})	L (pc)	T (K)	M ($M_\odot$)	Example
Diffuse	1	500	3	50	50	ζOphiuchi
Giant Molecular Clouds	2	100	50	15	10^5	Orion
Dark Clouds						
Complexes	5	500	10	10	10^4	Taurus-Auriga
Individuals	10	10^3	2	10	30	B1
Dense Cores/Bok Globules	10	10^4	0.1	10	10	TMC-1/B335

Note. — Table from Stahler & Palla (2004)

very small and they are mostly transparent to the background stars. Although these regions are excellent laboratories to use a large number of absorption lines, especially in the UV, to study the molecular abundances and chemical reactions, their masses and densities are very small and they are not active sites of star-forming regions.

GMCs are the largest known structures in the ISM which are gravitationally bound. More than 3000 GMCs have been identified in the Galaxy. Their sizes are typically tens of parsecs which represents only one percent of the ISM volume but contains almost half of its mass. The typical mass of GMCs varies between 10^4 and 10^7 $M_\odot$. Self gravity is the dominant force in GMCs and internal thermal pressure is not enough to keep the balance against gravitational collapse, but there are other forces that should be considered. Turbulent regions have an extra internal dynamics and therefore an extra kinetic energy. Magnetic fields also can play an important role to support the cloud against collapse. The stability of the cloud can be described by the Virial theorem:

$$2T + 2U + W + M = 0 \tag{1.1}$$

where T is the total kinetic energy of the bulk motion, U contains the thermal random motion of the molecules, W is the gravitational potential energy and M presents the energy associated with magnetic fields. Except W, all other energies are positive. If they all together can not compensate W, then the cloud will gravitationally collapse and may also fragment during this process.

Figure 1.3 presents a schematic of a molecular cloud. Each cloud con-

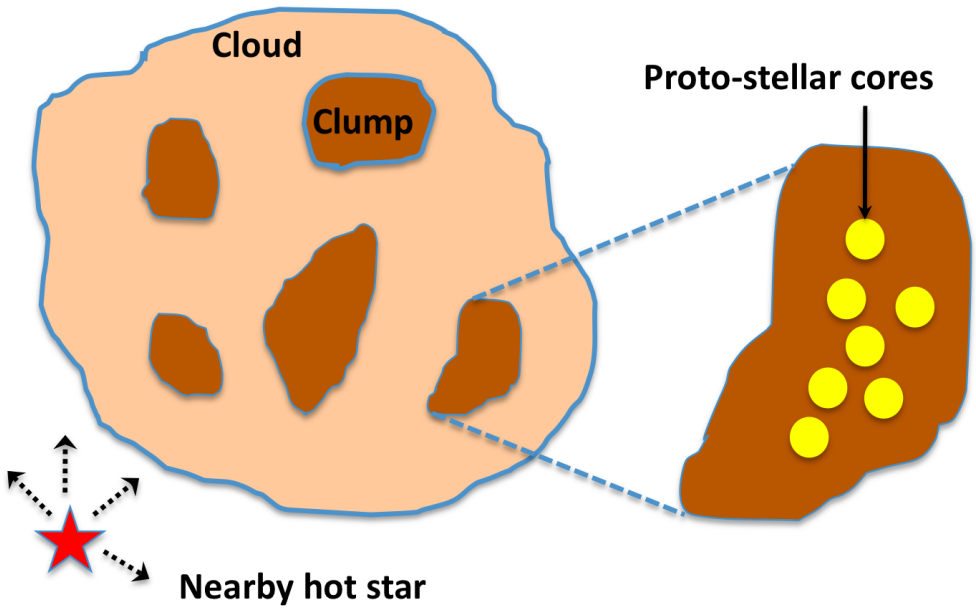

Figure 1.3 graphical presentation of a molecular cloud. Each cloud may contain several dense clumps. While the whole cloud might be gravitationally bound, most of the internal clumps are not. They fragment into smaller pieces and produce several proto-stellar cores. The number and mass distribution of resulted stars are determined by the physical conditions of the clumps.

tains several dense "clumps" which may contain or produce several proto-stars. While the total cloud might be in balance, internal clumps have higher densities and maybe unstable against gravitational collapse, as a result, the clump may fragment into many pre-stellar "cores".

The clumpy structure of molecular clouds has been well studied (e.g Jorgenssen et al. 2008, Reid & Wilson 2005, 2006) and the physical characteristics of the clumps such as clump mass function, have been derived in several regions. However derived parameters are highly affected by the poor resolution of observations in the sub-mm, the uncertainty in estimating source distances and the identification of the edge of the clump. The space between the clumps within a cloud is occupied by a cold low density gas. This low density molecular gas has been mapped in different CO isotopes and emission lines, and found to contain only a small fraction of the cloud mass.

Individual clumps may have large masses up to a few thousand solar masses, but even more massive structures within molecular clouds have been identified as "dark clouds". Most of these clouds are dark in wavelengths of 7-100 μm, presumably because they do not contain any young stellar objects or any newly formed stars are very deeply embedded (Ragan et al. 2006). infrared dark clouds (IRDC) might be quiescent intermediate or massive star-forming potentials known as pre-proto-stellar cores.

Bok globules (Bok & Reilly 1947) are isolated molecular clouds with small masses (2-100 $M_{\odot}$), small sizes (0.1-1 pc) and high densities (10^4 cm^{-3}). They

are easily identified as dark compact clouds against a background of diffuse gas or background stars (Fig. 1.4). They may form spontaneously from small local fluctuations, or be triggered by an external source such as strong stellar winds, or be a result of the fragmentation of a larger molecular cloud. Therefore they may not be perfectly isolated and some connections to distant molecular clouds has been found (Khanzadyan et al. 2002). Bok globules may form individual low mass stars or small groups of stars.

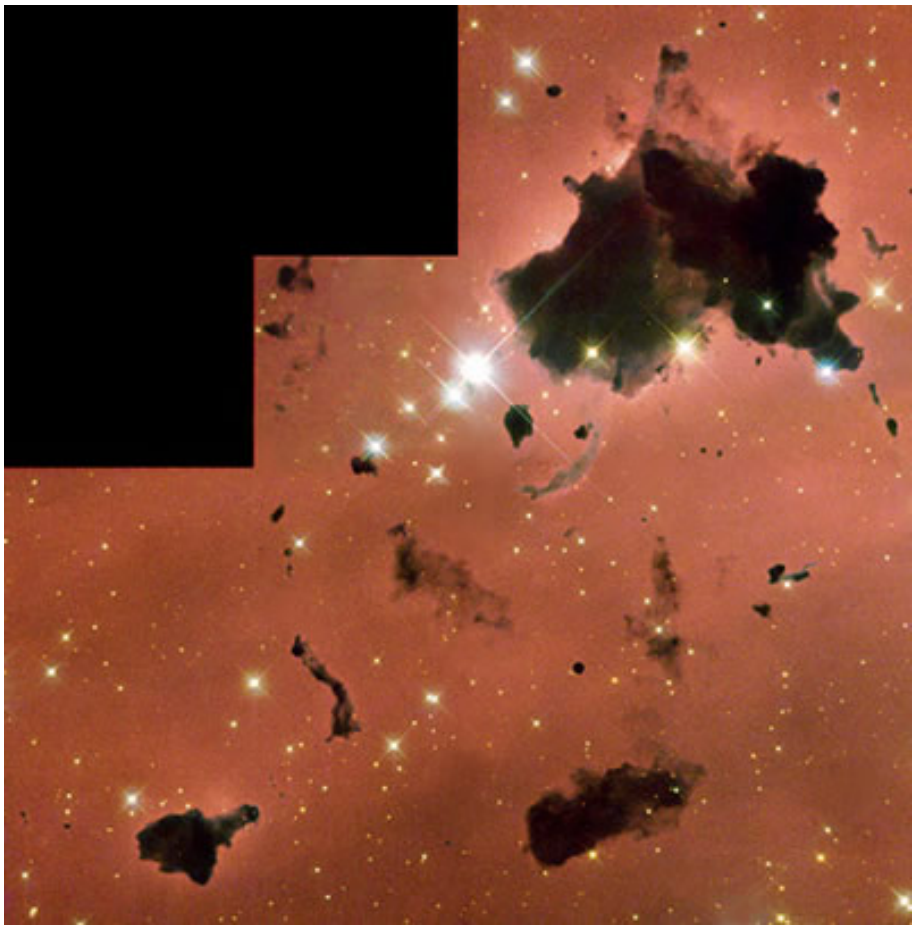

Figure 1.4 Bok Globules (two large dark clouds in top right corner) block the emissions from a bright background H II region.

Credit: NASA and The Hubble Heritage Team (STScI/AURA)

1.4 From Clouds to Stars

As discussed above, star formation may originate in molecular clouds with a wide range of size and internal dynamics but similar temperature and density. The environmental conditions and presence of external sources such as massive stars affect the process of star formation and may change the star formation rate, efficiency and mass distribution of the proto-stars. For example, warmer regions are more stable against gravitational collapse and may produce more massive stars. A simulation of the star formation process within two regions with Jeans mass (the maximum mass that a clump can have and still be stable against gravitational collapse) of 1 $M_{\odot}$ and 1/3 $M_{\odot}$ as initial conditions found that the accretion time and consequently star formation rate and efficiency is not similar in the two regions (Bate & Bonnell 2005). The mass function (number of stars vs. mass) was also dissimilar for the two calculations: the region with smaller Jeans mass had larger number of brown dwarfs and wider range of stellar mass (Figure 1.5). The low-mass and high-mass cut-offs are also different and slightly smaller and larger respectively for lower Jeans mass regions.

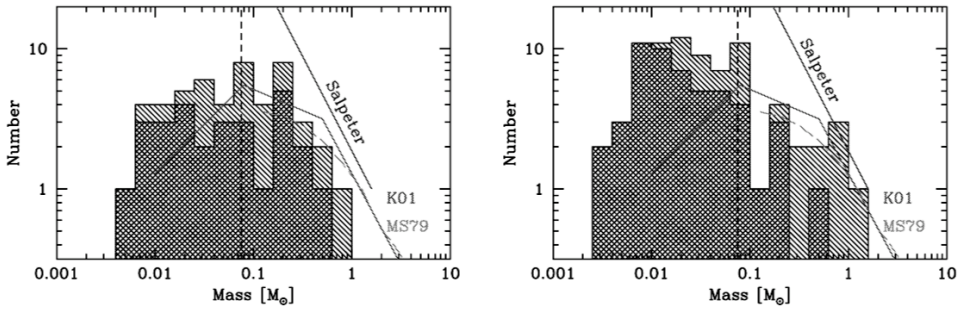

Figure 1.5 The Initial Mass Function of two simulated groups of stars. The left panel had the larger initial Jeans mass (1 $M_\odot$ vs. 1/3 $M_\odot$ in the right). The single shaded histograms show all of the objects and the double shaded show only the regions that have finished accretion. Different IMFs have been superimposed on the simulation (Salpeter 1955, Kroupa 2001 and Miller & Scalo 1979). The vertical dashed line is the boundary between stars and brown dwarfs. The region with smaller Jeans mass (right panel) has produced much higher fraction of brown dwarfs. (Diagrams from Bate & Bonnel 2005)

1.4.1 Isolated Low-Mass Star Formation

Low mass isolated star formation is the simplest mode that can be modelled. The term "isolated" means that the individual forming star has not been affected by external agents and is governed only by its own gravity and internal pressure. In such conditions low mass stars are expected to form. These conditions may also occur within a larger cloud while a small isolated clump collapses on its own gravity and has negligible interaction with the parent cloud; many low mass stars are formed within massive star-forming regions as well. Gravity is the most important agent in all star formation processes but in an isolated region this is the only "collapsing" force. Sometimes, collapse in a large cloud causes fragmentation.

A simple isolated spherical model assuming a decreasing volume density proportional to r^{-2} has been discussed by Shu (1977). This model provides a simple analytical description of proto-stellar collapse, but it is far from reality and especially faces the problem of a singularity at the core centre. In two different studies Bonnor (1956) and Ebert (1955) assumed that an external pressure helps gravity keep the isolated sphere bound. A detailed study of the collapse of molecular cloud cores using a high-resolution three-dimensional numerical simulation of the Bonnor-Ebert model shows that formation of both low-mass and high-mass proto-stellar disks can be explained with this model (Banerjee 2004). Adding rotation to this simulation produced solid disks that do not fragment and ring disks that fragmented into two proto-stellar cores.

However the Bonnor-Ebert model requires assumptions and can be solved only numerically for selected circumstances. In a recent model, Dapp and Basu (2009) considered a Bonnor-Ebert like sphere which is not in equilibrium. Their model sphere has a flat density at a central region that declines with r^{-2} beyond the small central part. In this model they can determine the dynamical state (expansion, equilibrium, collapse) of the core. They showed that for example L1689B pre-stellar core cannot be in equilibrium but instead appears to be collapsing, while their model verifies that another pre-stellar core, B68, is close to being in equilibrium.

Small dark clouds, or Bok globules, are the best places to look for isolated star formation. Particularly the nearby clouds are ideal places where we can measure the size and resolve the cores. However their distances are very uncertain. A study of a sample of six typical globules in CS emission lines estimates an average size of 0.33±0.15 pc (Launhardt et al. 1998). The same objects mapped in $C^{18}O$ gave smaller average sizes of 2.9±1.6 (Wang et al. 1995). CS and $C^{18}O$ have different opacities and CS traces higher densities. Therefore the two different measured sizes show the internal density profiles.

The uncertainty in measuring size affects the calculated masses. For the sample studied by Launhardt (1998), the CS(2-1) gave an average mass of 26±12 $M_\odot$ while $C^{18}O$(2-1) data gave M = 10±6 $M_\odot$. Other studies suggest the same range of mass and dissimilarity using different tracers (e.g Onishi et al. 1998) pointing out that larger cores may contain more than one proto-star.

They are cold with an average kinematic temperature of ~ 10 K and average density of $n \sim 10^4 - 10^5$ cm^{-3}. Distinct cores may form individually or within larger clouds.

1.4.2 Clustered Star Formation and Massive Stars

Individual low-mass star formation has been studied theoretically in detail and is well described. Unfortunately, only a small fraction of stars form in individual cores. Instead most of them originate in stellar clusters (Lada & Lada 2003). The scenario for low-mass star formation may be valid for intermediate stars with masses up to 10 $M_\odot$, but more massive stars, up to 150 $M_\odot$, seem to exist. The simple accretion model fails to explain the formation of massive stars because the radiation pressure of such stars will stop accretion before their pre-stellar disk can collect such a large amount of mass. Another main question in clustered star formation that yet remains to be investigated is: what is the (minimum) sufficient mass and density to form clusters containing massive stars, and how is the mass distribution of the forming stars affected by the previously formed stars? A power-law mass distribution for stars has been observed in many star forming regions and clusters as:

$$dN(M) \propto M^{-\alpha} dM. \tag{1.2}$$

Slightly different slopes have been reported (e.g Kroupa 2001, Scalo 1998), but there is no evidence of variation in different star forming regions (Massey 1998) and different mass ranges (Elmegreen 2000). Some studies also derive a clump mass function similar to the stellar IMF (Alves et al. 2006), while others suggest a different slope, considering various collapse times for clumps over a large mass range (Larson 2005). Brand & Wouterloot (1995) found 1.4 $\leq \alpha \leq$ 1.8 for star-forming regions for both the inner and outer Galaxy. Why the mass spectrum is almost universal and how the most massive stars can form are still unanswered questions.

The observed mass distribution supports the idea that most stars form in dense massive clumps (Evans 1999), with high column density ($\sim 10^{23}$ cm^{-2}) and large velocity dispersions ($\Delta V \geq 6$ km s^{-1}) within scales smaller than 1 pc. However, the star formation rate per unit mass seems to be independent of the cloud mass (Evans 1991).

The observations suggest two major scenarios for massive star formation. That the most massive stars have been found within or close to forming clusters, suggests that they are probably built by the collision and merger of smaller stars and proto-stars (e.g. Bonnell et al. 1998). That requires high density rich clusters, which have been frequently observed. The Orion nebula cluster is one of the most famous ones. This model is known as the Competitive Accretion. On the other hand a Turbulent Radiation-Hydrodynamic model suggests that even radiation pressure or ionization cannot prevent massive stars forming from

massive turbulent cores (Krumholz et al., 2007). Here we compare these two models and the observational facts and predictions that support each model.

1.4.3 Competitive Accretion versus Turbulent Radiation Hydrodynamic Models

The competitive accretion model simply explains the formation of massive stars and massive binaries up to 30 $M_{\odot}$ that would be likely to merge using only gravity and hydrodynamics.In the competitive accretion model all stars first form in dense molecular clumps as small fragments or "seeds" in a mass range of 0.003-0.5 $M_{\odot}$ (Bate & Bonnell 2005). The "seeds" accrete mass rapidly while the clump is also collapsing to high stellar densities as large as $10^6 - 10^8$ pc^{-3} (Krumholz 2006) at which the merging starts.

The model offers potential observational test and predictions. For example mergers should produce infrared flares that can survive for centuries (Bally & Zinnecker 2005). However there is no infrared data set available that shows such flares. The mergers should also produce eruptive outflows with random orientations, but there is no detailed modelling of how the outflow would form and how common they are (Krumholz 2006a). Another direct observational test is to look for high density embedded clusters which are required for mergers. These objects should be rare as they evolve very fast but their high column density would produce a specific spectral shape that might be observable with

recent space telescopes (Krumholz 2006a). Finally, if massive stars form in mergers, their accretion disks cannot survive the collision and therefore they cannot produce highly collimated outflows. Contrarily, interferometric observations of early B stars confirm that they have highly collimated outflows.

The turbulent hydrodynamic model considers the possibility of forming massive stars with roughly the same accretion scenario as for low mass stars but adding turbulence to the initial conditions. The similarity between clump/core mass function and the IMF suggests s that massive cores can form in fragmentation processes in turbulent regions; this has been confirmed analytically (e.g. Li et al 2004) and observationally (Reid & Wilson 2005). Massive cores need to be turbulent to stay in balance with gravitational collapse and external pressure (McKee & Tan 2003). They must be very compact ($\leq$ 0.1 pc) with high column density ($\sim 10^{24}$cm^{-2}) which produces the accretion rates of $10^{-3} M_{\odot}$ yr^{-1} to embedded pre-stellar cores, which may produce a massive star in $\sim 10^5$ yr (Krumholz 2006a). A simulation of turbulent massive cores predicts that they fragment into smaller cores and form several low mass stars instead of a few massive stars (Dobbs et al. 2005) but Krumholz (2006b) included radiative transfer to the same simulation and concluded that the rapid heating may prevent the fragmentation. The outflows from massive proto-stars come from close to the hot core where most dust has vaporized; therefore the outflows are dust-free and optically thin and can work as cavities to release the radiation pressure and make it weaker than gravity even in a 50 $M_{\odot}$ proto-star

(Krumholz 2005).

Competitive accretion and turbulent hydrodynamic models both give an explanation of how massive star may form, but none of their simulations consider the effect of magnetic fields in the process. They also do not predict a cut-off for the highest possible mass for a star especially the merger scenario which seems to be a scale free process; it is difficult to put an end to the collisions while merging two 150 $M_{\odot}$ might produce a black hole rather than a star (Krumholz 2006a).

1.5 Cloud Dynamics and Emission Line Profiles

Various molecules and several transition emission lines are used to probe the density of the gas in star forming regions. Each emission line has a specific critical density which is defined as:

$$n_c(jk) = A_{jk}/\gamma_{jk}. \tag{1.3}$$

where A_{jk} is the Einstein coefficient for spontaneous emission rate and γ_{jk} is the collisional de-excitation rate per molecule in level j. A list of common density probes and their properties is given by Evans (1999). Detection of a specific line indicates that the density of that region is higher than the critical

density of the detected emission, although it also depends on the observational sensitivity, the frequency and the optical depth.

Analyzing the profile of various molecular emission lines provides information about the internal dynamics of the cloud. Each emission line has a thermal line width due to the thermal gas motion, but it is smaller than the line broadening caused by strong internal motions or turbulence or even a proto-stellar outflow. A rotating clump also have widened emission lines which are red-shifted and blue-shifted on the opposite sides of the clump. Observing dense cores in different density tracers may show signatures of in-fall motions or expansion. For example CS is a high density tracer while CO is optically thick and traces only the low density gas of the envelope around the dense core. A significant difference between the velocities where the emission line peaks indicates a velocity gradient inside the cloud.

Sometimes the emission lines are complicated and have a double peaked or multiple peaked structure. The multiple peaked profiles may be due to multiple cores at different distances with different central velocities in the line of sight, but there are several physical and dynamical conditions that may cause such profiles. For example, a double peaked profile in an optically thick emission line such as CO may occur by self absorption if the internal core is hotter than the surrounding envelope. Observing the same core in higher density tracers may show a peak at the same velocity/frequency of the absorbed portion of the optically thick line (e.g Figure 2.6 in chapter 2, Brand et al. 2001).

A double peaked profile may also indicate a contracting cloud. Myers et al. (1996) simulated more complicated profiles in good agreement with observed lines for various molecules. A simple model of inside-out collapse discussed by Evans (1999) is shown in Figure 1.6. The outer static envelope emission has no Doppler shift. The emission from the rear side of the core creates the blue-shifted peak while the emissions from in-falling material at the front side produce the red-shifted peak. This simple model fits a variety of profiles for infall candidate cores.

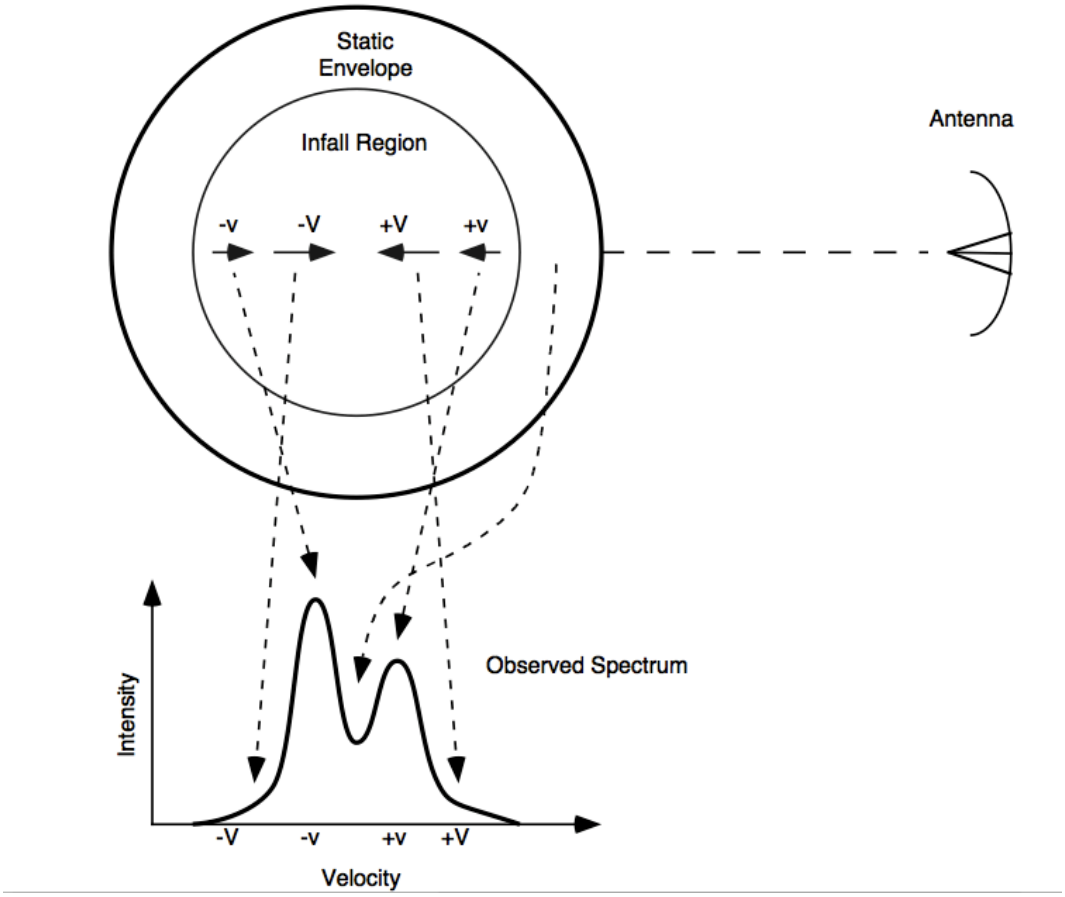

Figure 1.6 A simple diagram to show the origin of double peaked line profiles in collapsing cores. The static envelope produces the central deep, The blue peak comes from the infall of the back side materials and the red peak from the front side. (picture from Evans 1999)

1.6 Embedded Clusters in Molecular Clouds

Studies using 2MASS data (Carpenter 2000) suggest that a large fraction of stars are formed in embedded stellar clusters (Lada et.al 1991, Li et.al. 1997). Therefore the study of young clusters may answer fundamental questions about the star formation process. These stellar systems are young enough that they still have most of their massive stars and the low mass stars are mostly Pre Main Sequence (PMS) stars and are therefore brighter than at any other time in their lives. For these reasons dense cores are perhaps the best places to study a complete initial mass function (IMF). infrared observations in such regions can record the entire range of stellar masses from 0.01 to 100 $M_{\odot}$ (Lada & Lada 2003). In the early stages of evolution young stellar objects are embedded within dense gas and a large fraction of the visible light is absorbed by surrounding dust and gas. Such young clusters can be detected only in near infrared (NIR) emission which has a smaller extinction. For example, a photon in the K band (at 2.22 mu m), has an extinction 10 times smaller that of a V-band photon (at 0.55 μ m). Therefore, a T Tauri star of spectral type of K7, with M_V=+6.5 and M_K=+2.2 at a distance of 200 pc in a cloud with $A_V > 12$, has an apparent magnitude of +25 which is fainter than the detection threshold but the same star could be in a cloud with $A_V = 100$ and still be detectable at K band, considering a detection limit of +20 on ground base telescopes (Stahler & Palla 2004, equation 2.12).

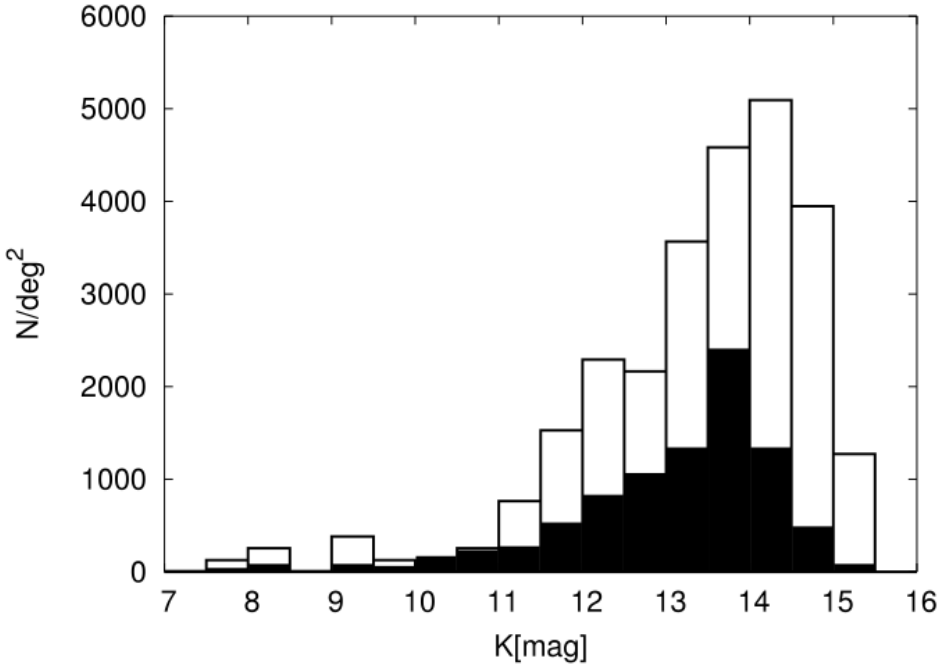

Figure 1.7 The K-band luminosity function for members of embedded clusters within NGC 7538 (filled histogram) compared to all stars in the field (open histogram). The KLF for cluster members peaks at a magnitude smaller than the total sample of stars in the field (Balog et al. 2004)

Stars formed in a cluster share the same initial conditions and they probably have the same age. Therefore, they provide a good laboratory to test different theoretical models. Embedded clusters evolve very fast, with significant changes in observable properties, in only two or three million years, and clusters older than 5 Myrs are probably not associated with molecular gas any more (Leisawitz et al. 1989). Only approximately 7% of all clusters survive to ages of $\sim 10^8$ yr and these longer lived clusters are likely massive clusters with a total mass larger than 500 $M_\odot$ (Lada & Lada 2003). The Pleiades is a good example of such long lasting open clusters. Clusters older than 10 Myrs may lose some of their original members due to evolution and dynamical interactions. It is also important to consider that the cluster evolution depends on the distance from the Galactic centre which contains more gas and stars. The larger amount of mass causes larger tidal forces that can destroy the cluster. Consequently most of the older open clusters lie in the outer Galaxy (van den Bergh & McClure 1980).

The ages of clusters can be determined by luminosity function analysis. Three broad band filters J (1.25 μm), H(1.65 μm) and K (2.16 μm) or K_s (2.17 μm) are common in NIR studies. Figure 1.7 presents the K band luminosity function (KLF) of an embedded cluster in NGC 7538 compared to the field stars. The open histogram shows all stars and the filled histogram the cluster members. The KLF peaks at one magnitude brighter for cluster members. The KLF is different from the field stars for young embedded clusters, but is not

a unique function. Figure 1.8 presents the KLF for three different clusters: Trapezium, IC 348 and NGC 2362. Even if the clusters start with the same initial conditions and the same IMF, they may not have the same KLF at different evolutionary stages. Muench et al. (2000) simulated the KLF for embedded clusters at different ages. Figure 1.9 displays the model luminosity function for clusters at ages of 1 Myrs, 3 Myrs and 10 Myrs. The younger cluster has more young stellar objects which are brighter in K magnitude and as they evolve they become fainter. Therefore the KLF peak shifts to fainter magnitudes for older clusters.

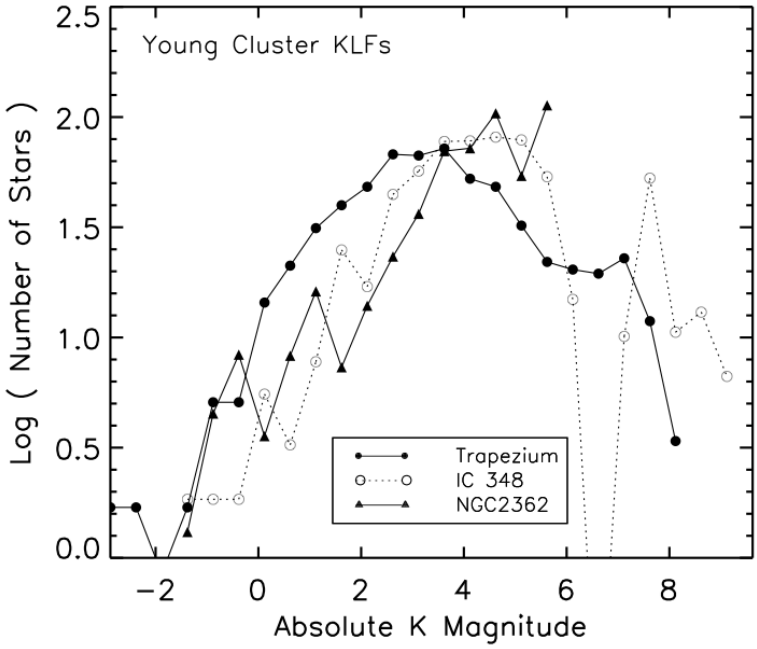

Figure 1.8 Observed KLFs for three young clusters adjusted to the same distance. The KLF peak trends to lower luminosity for older clusters (Trapezium, 10^6 yrs; IC 348, $3{\times}10^6$yrs and NGC 2362, 5×10^6yrs.

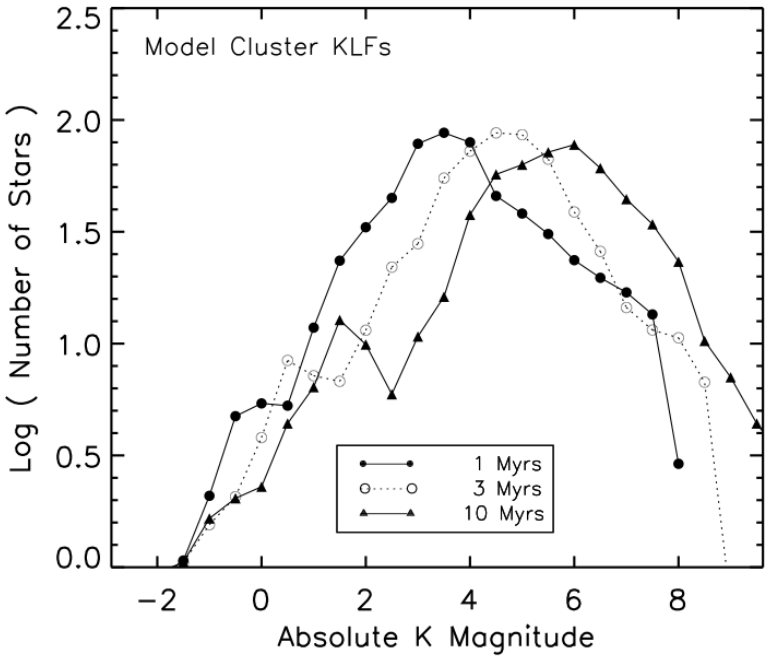

Figure 1.9 Model KLF for clusters originate from the same IMF but at different evolutionary stages. The younger cluster has higher K luminosity peak which is consistent with observations. The pre main sequence stars become fainter in K band as they evolve to main sequence stars. (Lada & Lada 2003)

1.7 Star Formation in Molecular Clouds Associated with H II Regions

1.7.1 Questions to be Addressed

As discussed before, there are several agents that govern the star formation process and variation of these parameters may result in totally different star formation mechanisms. For example high mass stars in particular require specific initial conditions such as high density gas and turbulence to form while the low mass stars can form through a more simple mechanism with initial conditions (temperature, density, etc.) as found in molecular clouds. The presence of massive stars itself highly influences the environmental conditions which may favour further (massive) star formation or prevent it. Stellar winds from the massive star and the expansion of the H II region may compress the gas in dense shells which may collapse to dense clumps and trigger star formation in a "Collect & Collapse" process (e.g. Elmegreen & Lada 1977, Deharveng et al. 2005). They also may affect the molecular gas internal motions and even initiate turbulence within the nearby gas. Radiation from the massive star and the ionized gas is another important agent that influences the fragmentation process in molecular clouds. As discussed before (section 1.4) a warmer environment is more stable against gravitational collapse and not only the star formation rate (SFR) and the star formation efficiency (SFE) may change in

such environments, the stellar mass distribution may also be influenced and as shown in Figure 1.5 a different initial mass function (IMF) might be expected.

In this work we investigate how the environmental conditions, and consequently the star formation has been affected by the massive star and the H II region. First we study the structure of the cloud. The molecular gas appears in different shapes and structures as filaments or diffuse gas but in most regions it has a clumpy structure with condensations that vary in size from < 0.1 pc to > 100 pc. The clumpy structure has a hierarchal pattern and the size of identified clumps is highly dependent on the distance and the telescope resolution. In next step we measure and calculate the physical parameters such as temperature, velocity dispersion, gas density, optical depth and mass for each clump. The derived parameters in different regions will be compared to study how they change and weather the variations are made because of the presence of massive star or the H II region. For example is the number of clumps, their size and distribution the same near the H II region and far from it? How is the environment warmed up by the radiation from massive stars and the H II region? Is the internal dynamics of the clumps affected by the H II region or can we find any evidence of turbulence caused by the expansion of H II region? Do the fragmentation process and the mass distribution of the clumps vary under the influence of the H II region? Is there any relation between the derived parameters, and if so, what does it mean? Do these relations vary in different regions?

In the next step we look at the stellar population within the clouds. It is expected that the process of star formation and especially the formation of high mass stars originates in dense massive clumps. We study how the distribution of stars is associated with the structure of the gas and related to the clump distribution in each region. Where has the star formation been triggered? How does the star formation rate and efficiency vary in different clumps and do they agree with the global values? Are there any clumps that provides the required conditions to form high mass stars? If so, do they contain massive proto-stars?

In next chapter we compare two selected regions within the same cloud; one is nearby the H II region and likely affected by the radiation of massive star and the second one distant enough which is unlike to be affected. Chapter 3 reviews the entire sample and examines the relation between the derived parameters for the gas and how they have been affected by the H II regions. Then we study the stellar distribution within the mapped regions using 2MASS data and investigate how the stellar distribution is related to gas structure and what are the star formation rate and efficiency within the investigated regions? We also look for young embedded clusters, evidence of triggered star formation and also candidates of massive proto-stars.

1.7.2 Sample Selection and Observations

H II regions are the signposts of particularly active star formation. Star formation properties (e.g. the rate, the efficiency of conversion of gas mass to stellar

mass, and the resulting Initial Mass Function) are dependent on the properties of the molecular clouds where the star formation occurs. Density, temperature, turbulence and the presence of shocks are some of the major cloud parameters that may affect the star formation process. The environments around H II regions, are much hotter than in regions of low mass star formation. Different initial conditions such as a higher temperature may cause different star formation scenarios, and may finally result in different Initial Mass Functions.

We have selected 10 H II regions from the Sharpless (1959) catalog of visible H II regions. The sources were selected to be in the outer Galaxy, to minimize confusion with background sources and to provide the best estimate of kinematic distances. Figure 1.10 presents the position of most of the sources in our sample in the Galactic plane. The selected H II regions have small enough angular size ($\leq 7'$) to make it possible to completely map the molecular gas at the edges of the ionized gas in $7' \times 7'$ maps.

Observations were carried out at different stages with James Clerk Maxwell sub-millimeter Telescope. In the first stage from August to November 1998, six ^{12}CO(2-1) maps were made of $7' \times 7'$ area of molecular clouds associated with H II regions. S192/S193/S104, S196, S212, S305 and two sub-clouds, S175A and S175B associated with S175, were mapped in this period. We used these maps to study the structure of the clouds and to identify the dense clumps within the clouds. Pointed observations in ^{13}CO(2-1) on peaks of those identified dense clumps within each region were made from August 2005

to February 2006. We also made some pointed observations in CS(5-4) at the clumps with ^{12}CO(2-1) antenna temperatures larger than 20 K. We use these observations to measure and calculate physical properties of the clumps such as excitation temperature (T_{ex}), line width, density, opacity and mass. In this observing period we also made a $7' \times 7'$ ^{12}CO(2-1) map of S104 with the same observational settings as in 1998; but due to the large angular size of this H II region we missed most of the associated molecular gas in our map. Therefore, we decided to extend S104 map to a larger area.

Observations were followed with the new ACSIS system at the JCMT in four different observing runs from October 2006 to January 2009. Four more $7' \times 7'$ ^{12}CO(2-1) maps were made around S148/S149, S152, S288 and S307 and the S104 map was extended to $12' \times 12'$. We also observed most of the peaks identified in clumps within the maps in ^{13}CO(2-1) . Details of observational settings are given in chapters 2 and 3 (Paper I and Paper II).

Table 1.3 lists the selected sources in our sample. Column one gives the name of the source and columns two and three give the coordinates at the centre of each mapped region. Column four gives the distance based on the known exciting star. No exciting star has been reported for S196 and therefore we use the kinematic distance for this object. All distances are collected from the literature and cited in the table. Column five shows the molecular gas velocity from CO emission. Columns six and seven present the size of the H II region. Finally, column eight gives the known exciting star for each region.

The measured and calculated parameters of all the clumps identified within the entire sample are listed in chapter 3.

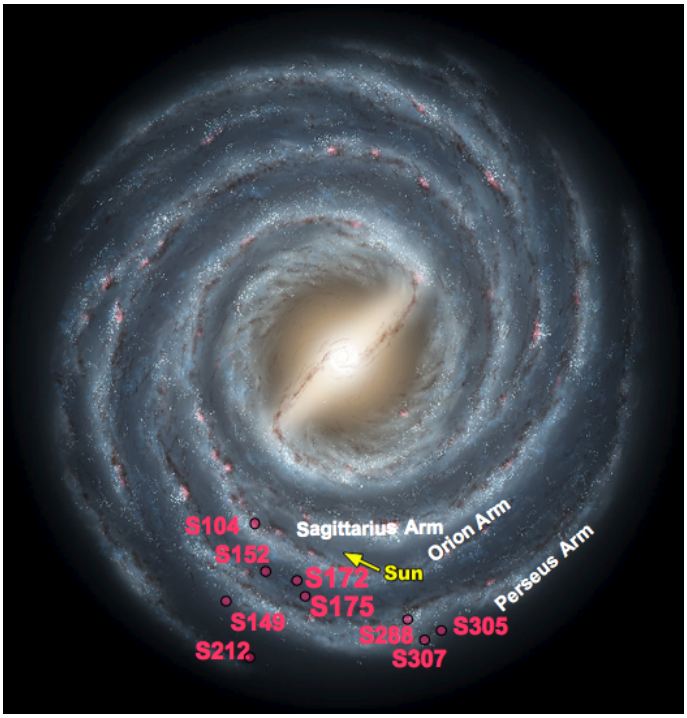

Figure 1.10 Position of some sources in our sample on a schematic picture of the Galaxy. Most of the objects have been selected at the outer Galaxy to minimize confusion with the background sources and to have an estimation of the kinematic distance of our sources (for those which we do not have a direct distance measurement). Background image credit: NASA/JPL-Caltech/R.Hurt(SSC)

1.8 Summary

The physical conditions vary within star-forming regions in a large range. Although some low-mass stars form within isolated dark clouds, the majority of stars originate in stellar clusters. Massive stars in particular, are believed to form in hot, dense, turbulent, massive clouds which fragment to several protostars. Most of the known massive stars are found within young stellar clusters.

The theories to explain isolated star formation are well developed and tested by various observations. Our understanding of massive star formation is not as complete as low-mass stars. Current observations and models suggest that massive stars form within clusters from hot, dense turbulent cores.

Magnetic fields may play an important role in dynamically active clouds. To simplify this discussion we neglected the influences of magnetic fields in this chapter. The stellar Initial Mass Function has been studied in several star-forming regions and clusters and seems to have a universal shape. However slight variations have been observed and discussed theoretically. Studies looking for a correlation between the clump mass function and the IMF have had very different results. Almost all studies report a power law function, but the power law index varies over a large range. New generation arrays such as ALMA, which enable us to resolve the stellar mass cores and clumps within molecular clouds, may provide more accurate clump mass functions. Knowing the origin of the mass distribution of the star-forming cores will provides a better understanding on the origin of IMF.

Table 1.3. Properties of selected regions

Source	RA J(2000)	Dec J(2000)	Distance (kpc)	V_{LSR} (kms^{-1})	Diameter (arcmin)	Diameter (pc)	Exciting Star
S104	20:17:42	36:45:30	3.3±0.3	0.0	7	6.7	O6V [a]
S148/S149	22:56:22	58:31:29	5.6±0.6	-53.1	1	1.6	B0V [a]
S152	22:58:41	58:47:06	2.39±0.21	-50.4	2	1.4	O9V [b]
S175A	0:27:04	64:43:35	1.09±0.21	-49.6	2	0.63	B1.5V [b]
S175B	0:26:25	64:52:36	1.09±0.21	-49.6	2	0.63	B1.5V [b]
S192/193	2:47:30	61:56:33	2.96±0.54	-46.3	1	0.86	B2.5V [b]
S196	2:51:41	62:12:19	4.7±1.0	-45.1	4	5.4	... [d]
S212	4:40:56	50:27:47	7.1±0.7	-35.3	5	10.3	O6 [a]
S288	7:8:39	-4:18:41	3.0±1.2	56.7	1	0.87	B1 [c]
S305	7:30:13	-18:31:50	5.2±1.4	44.1	4	6.1	O9.5 [c]
S307	7:35:33	-18:45:55	2.2±0.5	46.3	6	3.8	O9 [c]

[a]Data about exciting star and distance from Caplan et al. 2000

[b]Data about exciting star and distance from Russeil et al. 2007

[c]Data about exciting star and distance from Moffat et al. 1997

[d]No exciting star identified for this H II region. The kinematic distance is reported here. Note that S196 is close to S192/S193 in position and velocity and is likely to be at the same distance.

Note. — Table reprinted from Paper II.

Chapter 2

Molecular Clouds and H II Regions: S175

This chapter is a reprint of the paper **Molecular Clouds and H II Regions I: S175** by Azimlu M., Fich M., and M^{c}Coey C. which was published in the Astronomical Journal in June 2009 (Volume 137, Issue 6, pp. 4897-4910)

2.1 Overview

We are studying the impact of H II regions on star formation in their associated molecular clouds. In this paper we present JCMT RxA molecular line observations of S175 and environs. This is the first object within a sample of ten H II regions and their surrounding molecular clouds selected for our study. We first make $7' \times 7'$ maps in ^{12}CO(2-1), which are used to investigate the structure of the cloud and to identify individual clumps. Single point observations were made in ^{13}CO(2-1) and CS(5-4) at the peak of the ^{12}CO(2-1) emission within each clump in order to measure the physical properties of the gas. Densities, temperatures, clump masses, peak velocities, and line widths were measured and calculated using these observations. We have identified two condensations (S175A and S175B) in the molecular cloud associated with this H II region. S175A is adjacent to the ionization front and is expected to be affected by the H II region while S175B is too distant to be disturbed. We compare the structure and gas properties of these two regions to investigate how the molecular gas has been affected by the H II region. S175A has been heated by the H II region and partially compressed by the ionized gas front, but contrary to our expectation it is a quiescent region while S175B is very turbulent and dynamically active. Our investigation for the source of turbulence in S175B resulted in the detection of an outflow within this region.

2.2 Introduction

Molecular clouds are the birth place of stars, and it is essential to study the formation, evolution and fragmentation of molecular clouds in order to understand star formation. The star formation process in molecular clouds is driven by a variety of mechanisms and is strongly affected by the presence of high-mass stars. When massive stars form it is expected that they dominate the formation process of other stars formed later in the same cloud. Heating of the molecular cloud by high-mass stars is likely to inhibit further star formation (Scoville et al. 87). On the other hand, compression of the cloud, by the action of stellar winds or from the expansion of an H II region, will enhance star formation (Lada & Wooden 1979) or even trigger star formation (via sequential star formation or the collect and collapse process, e.g., Elmegreen & Lada 1977, Zavagno et al. 2006, Deharveng et al. 2008). Alternatively, the expansion of an H II region may even blow the cloud apart (Elmegreen & Lada 1976). These different processes not only affect the rate of star formation within the cloud, but might also be expected to have some effect on the Initial Mass Function (IMF) of the newly forming stars. For example, the Jeans mass increases with cloud temperature: consequently a warmer cloud is more stable against collapse and the process of fragmentation may result in more massive stars with different star formation rates or efficiencies [**?**].

It is instructive, therefore, to study the molecular gas associated with H II

regions. Many studies have investigated the star formation process adjacent to H II regions (e.g Deharveng et al. 2005, Kirsanova et al. 2008, Kerton 2008). Statistically, it has been shown that the most luminous proto-stars form in molecular clouds associated with H II regions (Dobashi et al. 2001). Other studies suggest that a large fraction of stars originate in clusters (Li et al. 1997), mostly at the peripheries of H II regions (e.g. Zavagno et al. 2006, Deharveng et al. 2008).

Embedded clusters are associated with clumps and dense cores within clouds, where there is sufficient gas and dust available to form stars; therefore, the spatial distribution of clumps and cores should reflect the stellar distribution of recent or future star-forming regions. There is not a well-accepted unique definition of cores and clumps. In this work, we call the whole molecular gas associated with the H II region *the cloud* in which we have resolved three main distinct regions: S175A, S175B and S175C. We define a *clump* to be condensed material within each region that forms structures larger than the telescope beam size. Each clump is expected to contain sub-structure and exhibits one or more peaks in ^{12}CO(2-1) emission: we refer to these simply as *peaks* as we can not resolve proto-stellar cores within our maps. The ^{12}CO(2-1) antenna temperature of the brightest peak within each clump is reported as the clump's temperature and is used to calculate other parameters such as column density and mass.

This is the first paper resulting from a study of ten molecular clouds as-

sociated with H II regions which are selected from the Sharpless catalog of H II regions (Sharpless 1959). We have selected objects in the outer Galaxy, primarily along the Perseus arm, in order to minimize confusion with background stars and to provide the best estimate of the kinematic distance (for those objects which have no direct distance determination). S175 is our closest source and therefore provides us with the best linear scale resolution in our sample. We used the James Clerk Maxwell Telescope (JCMT) to study how the formation of a massive star in this molecular cloud may impact the formation of future stars. Clumps within the molecular cloud are identified and their physical characteristics, such as mass, column density and temperature, are measured from the properties of ^{12}CO(2-1) and ^{13}CO(2-1) emission. We look for the influence of shock fronts on the clumps and, from analysis of line widths, study the possible effects of turbulence and dynamics around the H II region.

We describe observation details in §2 and present the results in §3. In §4 we present the calculations and the models that we applied to determine physical parameters of the observed regions. §5 contains a discussion of how the H II region has affected the cloud physical characteristics and the paper is summarized in §6.

2.3 Target Selection and Observations

2.3.1 Investigated Region

At a distance of 1.09 ± 0.21 kpc (Russeil et al. 2007), S175 is the closest source in our sample and we are able to resolve smaller structures within the molecular cloud associated with this H II region. The H II region has been excited by a B1.5V star ($M \sim 9.5\ M_{\odot}$, Holmgren et al. 1997) at $\alpha(\mathrm{J2000}) = 00^h27^m17.1^s$ and $\delta(\mathrm{J2000}) = +64^o42'18.0''$. Scaife et al. (2008) calculated a dust temperature of $T_d = 27.9$ K for S175 by fitting a modified Planck spectrum to IRAS 100 and 60 μm flux densities and, using optical recombination lines, also calculated an electron temperature of $T_e = 7000 \pm 200$ K. Fich and Rudolph (in prep.) recently calculated a density of 112 cm^{-3} and a total mass of 0.4 $M_{\odot}$ for this ionized gas. Wouterloot & Habing (1985) also had reported a T_{CO}(1-0)=2.5 K and T_{ex}=5.7 K toward the associated molecular cloud, but they had low spatial and frequency resolutions.

Two components, S175A and S175B, in the molecular cloud have previously been identified in an IRAS survey (of H II regions) by Chan & Fich (1995). Both regions have the same $V_{LSR} \approx 50$ km s^{-1} and are connected by a recently observed filament of molecular gas with the same velocity. Therefore it is reasonable to assume that S175A and S175B lie at the same distance. Figure 2.1 shows the position of the cloud in an IRAS 12 μ m map (left panel). The components of the molecular cloud associated with the S175 H II region

cannot be resolved on the IRAS map but a recent study with the Arcminute Microkelvin Imager (AMI) (Scaife et al. 2008) shows that S175A and S175B, observed at 15.8 GHz, sit on a ring of an extended emission (Figures 2 and 3 in their paper). This ring, with a diameter of $14'$ or 7 pc, is shown in green in Figure 2.1 (right panel). A third condensation, which we label S175C, in the North-East of the boxed region can be seen but it is not as intense as the two mapped regions.

S175A is adjacent to the H II region and is likely to be affected by the ionized gas while S175B, at a distance of ~ 3 pc from the visible edge of the H II region (ten times the Stromgren sphere radius), is too far away to be affected. Therefore a comparison of these two regions may provide significant insight into the effects of the formation of a massive star (and the subsequent expansion of ionized gas) on the molecular cloud environment and on the physical properties that may affect future star formation.

2.3.2 JCMT Observations

In August and November, 1998, we made JCMT observations in ^{12}CO(2-1) of the two selected regions, S175A and S175B, (Figure 2.1). We made a ^{12}CO(2-1) $7' \times 7'$ map for each of these regions, with the A3 heterodyne receiver. The beam size at this frequency is $21''$. Data was taken by driving the telescope in right ascension (sampling step of $7''$) with a 4 second exposure time at each point. We made a mosaic of 12 sub-maps to complete each of the S175A and

S175B maps. Eleven of the sub-maps consist of 5 rows and 59 columns, and one consists of 4 rows and 59 columns to complete 59×59 pixel maps.

The ^{12}CO(2-1) maps were used to study the structure of the S175A and S175B molecular cloud and to search for the ^{12}CO(2-1) peaks within the identified clumps (see the next section for clump identification rules). ^{12}CO(2-1) is optically thick and can not be used to detect the dense gas embedded within the clumps. Therefore, the position of the brightest ^{12}CO(2-1) emission in each clump were observed in the optically thinner emission lines, ^{13}CO(2-1) and CS(5-4). We made pointed observations toward these positions in August 2005, December 2007 and July 2008. ^{13}CO(2-1) was detected towards all positions but we failed to detect any CS(5-4) emission within S175A. The peaks detected in S175B display lower temperatures; therefore, no CS(5-4) emission was expected and accordingly no CS pointed observations were made for S175B.

We used a bandwidth of 267.5 MHz with 1713 frequency channels which corresponds to a velocity range of about 350 km s^{-1} with a resolution of ∼0.2 km s^{-1} for ^{12}CO(2-1). The ^{13}CO(2-1) and CS(5-4) pointed observations in S175A were made in frequency switching mode. We used a frequency switch of 8.3 MHz, a velocity resolution of ∼0.05 km s^{-1} and a velocity range of 225 km s^{-1}. Frequency switching mode was not available while observing S175B and therefore we used a position switching mode to observe ^{13}CO(2-1). The system temperature, T_{sys}, was typically 300-600 K for ^{12}CO(2-1) mapping and 400-500 K for pointed observations. The typical noise level was 2 K for ^{12}CO(2-1) and

0.3 K for ^{13}CO and CS. We used SPECX and the Starlink SPLAT and GAIA packages to reduce the data, make mosaics, remove baselines and fit Gaussian functions to determine ΔV, the FWHM of the observed line profiles.

2.4 Structure in S175A and S175B

We used the ^{12}CO(2-1) maps to study the structure and morphology of the molecular cloud associated with S175, and to identify clumps within it. The cloud consists of various clumps of gas that display one or more peaks of emission (typically towards the centre of the clump), see Figures 2.3 and 2.5. We define any separated condensation as a distinct clump, if: 1) the brightest peak within the region has an antenna temperature larger than five times the rms of the background noise; 2) the drop in antenna temperature between two adjacent bright peaks when moving from one to another is larger than the background noise; and, 3) the size of the condensation is larger than the telescope beam size ($21''$ or 3 pixels). The edge of a clump is taken to be the boundary at which the antenna temperature drops to below half of the highest measured temperature within that clump. An ellipse that best fits to this boundary is considered for clump size and integrated flux measurements. Note that this definition means that clumps can contain several peaks of emission and, in fact, almost half of the detected clumps contain more than one bright peak.

2.4.1 S175A

We find the gas velocity in S175A to range from -48 km s^{-1} to -52 km s^{-1}, which is consistent with previous studies that found V_{LSR}(CO)= -49.6 ± 0.5 km s^{-1} (Blitz et al. 1982) and -50.3 km s^{-1} (Wouterloot & Habing 1985). The ^{12}CO(2-1) map (integrated between -48 km s^{-1} and -52 km s^{-1}) overlaid on the optical image of the H II region is presented in Figure 2.2 and shows that S175A takes the form of a wedge, which lies partially over the H II region, and a filament that leads to the North-West. The brightest ^{12}CO(2-1) emission peak lies at the centre of the region and at a velocity of -49.4 km s^{-1}.

Figure 2.2 also reveals S175A to have a clumpy structure. We used the clump selection method described above to identify thirteen clumps within S175A, which are indicated in Figure 2.3 by ellipses and listed in Table 2.1.

S175A consists of a bright centre containing clumps C5, C6 and C9. Flanking the central area to the East is a ring of clumps, of diameter ≈ 2′, consisting of C1-4 and C7 (Figure 2.3 left panel). We find no evidence for expansion of this ring; all the clumps display narrow single peaks at the same velocity (-49.5 ± 0.5 km s^{-1}) . A chain of clumps consisting of C10-13 lies to the West of the centre (Figure 2.3 right panel). The C8 clump, south of the ring, is the only clump in the same line of sight of the H II region. We are unable to determine whether C8 lies in front of or behind the H II region.

^{12}CO(2-1) is optically thick and can not be used to detect the dense gas

within the clumps. Therefore, we observed the brightest peak within each clump using single point observations of ^{13}CO(2-1) and CS(5-4), in order to further probe the properties of the clumps in S175A. The observed antenna temperatures, T_a^*, at these points are listed in Table 2.1, and range from 9.6-29.1 K for ^{12}CO(2-1) and 2.26-17.34 K for ^{13}CO(2-1). We failed to detect any CS(5-4) emission within this cloud, indicating that the densities of the dense centres are less than $\approx 10^6$ cm^{-3}.

As noted above, S175A is situated very close to the H II region and it could be expected to exhibit signs of turbulence, which could manifest as a large velocity dispersion between the clumps and/or as asymmetric line profiles broadened significantly beyond the thermal line width. However, we find the spread in velocity of the brightest peaks to be small: -49.0 to -50.8 km s^{-1} for ^{12}CO(2-1) and -49.0 to -50.9 km s^{-1} for ^{13}CO(2-1). Furthermore, both ^{12}CO and ^{13}CO velocity profiles of the peaks are very narrow ($0.78 < \Delta V < 1.61$ km s^{-1} for ^{12}CO and $0.47 < \Delta V < 1.08$ km s^{-1} for ^{13}CO - see Table 2.3) and symmetric. Comparing these line widths with calculated thermal line widths calculated from T_{ex} found in §2.5.1 ($0.51 < \Delta V < 0.82$ km s^{-1}), and assuming $T_{kin} = T_{ex}$, we may conclude that S175A is a quiescent region and not dynamically active.

2.4.2 S175B

The S175B ^{12}CO(2-1) map, which is integrated between -47 km s^{-1} and -53 km s^{-1}, is shown in Figure 2.4. In comparison with S175A, S175B is more uniform with an extended CO emission averaging $\sim$ 5-7 K covering more than 80 % of the observed region (Figure 2.4, left panel). Furthermore, a consistent background noise of $\sim$ 2 K exists through the mapped region.

Clump identification was therefore more difficult in S175B and was restricted to a region at the north-west that showed a greater degree of dynamical activity than in the rest of the region. A particularly dynamically active area is highlighted in the right panel (enlarged square) of Fig. 2.4. Twelve distinct clumps have been resolved within S175B (Figure 2.5) and are indicated by ellipses, with corresponding positions listed in Table 2.2. Most of the clumps are located in the northern part of the cloud and only three clumps (C4, C5 and C12) have been identified in the southern half. We are unable to resolve these three clumps any further because the southern half of the cloud is especially uniform and the clumps have irregular shapes with edges that are hard to distinguish from the extended 5-7 K CO emission.

As for S175A, single point observations in ^{13}CO(2-1) were made at the peaks within the clumps (C12 is yet to be observed in ^{13}CO). The observed physical parameters of each of these positions are listed in Table 2.2. We note here that the observed T_a^* are generally lower in S175B than S175A ($^{12}T_a^*$=9.3-16.8 K

and $^{13}T_a^*$=2.7 K to 6.3 K), while S175B shows a slightly wider velocity range at the peaks, with -47.8 km s^{-1} < V(^{12}CO) < -52.2 km s^{-1} and -47.7 km s^{-1} <V(^{13}CO) < -52.0 km s^{-1}.

In contrast to the narrow and uniform ^{12}CO(2-1) line profiles ($\Delta V \sim 1$ km s^{-1}) of the extended gas, the peaks within each clump have wide line profiles ($1.04 < \Delta V < 8.68$ km s^{-1} for ^{12}CO and $0.59 < \Delta V < 2.11$ km s^{-1} for ^{13}CO - see Table 2.4). With the exception of C5, which lies in a somewhat isolated position at the centre in the southern half of the region, the peak position ^{12}CO line profiles are asymmetric. S175B is clearly more dynamically active than S175A. Comparing the emission line widths with thermal line widths, ($0.51 < \Delta V < 0.65$ km s^{-1}) confirms that the observed line widths are significantly larger than the thermal velocity dispersion.

Furthermore, we see multiply-peaked profiles in ^{12}CO(2-1), which are identified by letters in Table 2.4, in C1-C3, C7 and C9 (compare the line widths and profile shapes in Figure 2.6). The multiple peak structure could be a result of self-absorption or multiple cores at different velocities along the line of sight. In ^{13}CO(2-1), we find that C1-3 and C7-11 appear to be either saturated or self-absorbed. Signatures of self absorption and saturation in ^{13}CO can be an indication of warm gas inside the cores. Alternatively, multiple peaks in ^{13}CO could support the possibility of multiple cores. Our recent observations in ^{13}CO(3-2) (Azimlu, M^{c}Coey & Fich, in prep.) at C1-C3 shows strong signature of an outflow located at C1, which could explain multiple peaked profiles

for these peaks.

2.5 Physical Parameters Derived from CO Observation

^{12}CO(2-1) maps have been used to study the morphology of the cloud, and to identify the position of clumps and their size. These observations also are used to determine the brightest peaks within each clump and measure the physical parameters of each peak, such as antenna temperature, line width and velocity profiles. Using these parameters we can calculate the mass of the clumps assuming Virial equilibrium conditions or calculate the velocity integrated (or "X-factor") mass, using a known "X-factor" (an empirical ratio of H_2 column density to the velocity integrated ^{12}CO(1-0) emission) to calculate the H_2 column density.

^{12}CO is optically thick and not suitable to measure the properties of the densest gas; therefore, we also calculated mass using observations of the brightest peak within each clump in ^{13}CO(2-1). We measure the ^{13}CO(2-1) antenna temperature and line width directly from the observed spectrum. Then, assuming Local Thermodynamic Equilibrium (LTE), we determine the excitation temperature, opacity and gas column density for the observed points. Assuming that clumps are uniformly spherical, we calculate the average volume density, LTE mass, and the Jeans Mass for each clump.

2.5.1 Temperature and Opacity

The corrected antenna temperature, T_a^*, and line widths for both ^{12}CO(2-1) and ^{13}CO(2-1) emission lines were directly measured from spectra, after baseline subtraction. For multiply peaked profiles, we determine a separate line width for each peak only if the separation is greater than 1 km s^{-1} (five times of the channel resolution of 0.2 km s^{-1}). The brightest ^{12}CO peak within a multiply peaked spectrum is used in calculation.

T_b, the received brightness temperature, is related to the directly observed antenna temperature through the beam efficiency and beam filling factor; $T_a^* = T_b \eta_{mb} f_{BEAM}$. The beam efficiency, η_{mb}, is 0.69 at the JCMT for the observed frequencies, and f_{BEAM} is the fraction of the telescope beam filled by the source emission. Although our sources are larger than the beam size, we expect that there will be sub-structure due to the hierarchical nature of the ISM. However, we have no means to measure this and we take $f_{BEAM} = 1$ in order to calculate T_b. Strictly speaking, therefore we find a lower limit to T_b.

The opacity, τ, and excitation temperature, T_{ex}, can be derived by comparing the ^{12}CO(2-1) and ^{13}CO(2-1) brightness temperatures:

$$T_b = T_0 \left[f(T_{ex}) - f(T_{bg}) \right] \times \left[1 - exp(-\tau) \right] \tag{2.1}$$

$$\text{and} \quad f(T) = \frac{1}{exp(T_0/T) - 1}, \tag{2.2}$$

where T_{bg} is the microwave background temperature (2.73 K) and $T_0 = h\nu/k$, with ν_{12} = 230.538 GHz for ^{12}CO(2-1) and ν_{13} = 220.399 GHz for ^{13}CO(2-1). We consider a Local Thermodynamic Equilibrium (LTE) model in which ^{12}CO(2-1) and ^{13}CO(2-1) have the same T_{ex} and $\tau_{13} \ll \tau_{12}$. The abundance ratio of two isotopic species is also required in order to derive T_{ex} and τ from expression 2.1. This ratio varies from 24 at the centre of the Galaxy to a terrestrial value of 89. We adopt the commonly used average value of 62±4 derived by Langer & Penzias (1993) for molecular clouds in the solar neighbourhood.

T_{ex} can be calculated from the optically thick ^{12}CO line (e.g. Pineda et al. 2008). We can then solve equation 2.3 to obtain T_{ex},

$$T_{ex}(^{12}CO) = \frac{T_0^{12}}{\ln\left[1 + \frac{T_0^{12}}{T_b(^{12}CO)+T_0^{12}f(T_{bg})}\right]}\ , \tag{2.3}$$

and then the opacity, using ^{13}CO:

$$\tau_{13} = -\ln\left[1 - \frac{T_b(^{13}CO)}{T_0^{13}}\left\{\left[exp(\frac{T_0^{13}}{T_{ex}}) - 1\right]^{-1} - f(T_{bg})\right\}^{-1}\right]. \tag{2.4}$$

To derive these equations it has been assumed that $\tau_{12} \gg 1$. The calculated T_{ex} varies from 15.9 K to 34.5 K for S175A and from 14.2 K to 22.1 K for S175B. Observed and calculated parameters, such as T_a^*, T_{ex}, ΔV_{12} and ΔV_{13}, τ_{13} and $\tau_{12} = 62 \times \tau_{13}$, and the corresponding hydrogen column density are listed in Tables 2.3 and 2.4 for S175A and S175B.

2.5.2 Mass Estimation

In this Section, we describe how individual emission lines of ^{12}CO and ^{13}CO are used to estimate the mass of individual clumps in S175A and S175B by several means. We use line widths of ^{12}CO and ^{13}CO in order to calculate the Virial mass, we have also calculated the ^{12}CO velocity integrated mass (or "X-factor" mass), and used an LTE model to determine the ^{13}CO column density. We also calculate the Jeans Mass for each clump. In the following we describe each method individually and give the range of masses found for S175A and S175B. The masses determined by each method for each clump can be found in Tables 2.5 and 2.6.

Virial Mass

According to the Virial theorem for a stable, self-gravitating, spherical distribution of mass (excluding other agents such as external pressure and magnetic fields), the kinetic energy must equal the half of the potential energy. Assuming that our clumps are in Virial equilibrium, the Virial mass is calculated from

$$M_{vir}(M_{\odot}) = 126 \times R_e(pc)(\Delta V)^2(kms^{-1}), \tag{2.5}$$

which assumes a spherical distribution with density proportional to r^{-2} (McLaren et al 1988). If the calculated Virial mass is larger than the mass measured by

other techniques then the object has too much kinetic energy and is not stable. Most of the clumps have an irregular shape and an appropriate value for the radius can not be taken from the ^{12}CO maps. Instead, we calculate the area of a clump from the ^{12}CO maps and assumed the effective radius of $R_e = \sqrt{Area/\pi}$. We do not have any measurements of the clump size from the ^{13}CO(2-1) pointed observations; therefore, we use the same measured radius from ^{12}CO maps for both lines.

There are uncertainties in measurement of the parameters in this equation which carry through to the mass estimation. For example, our size estimation relies on distance measurement that has an estimated uncertainty of $\sim 20\%$. In addition, each CO isotopomer presents different line widths; ΔV_{12} is observed to be on average larger than ΔV_{13} by a factor of 1.7. ^{12}CO(2-1) is optically thick and most of the observed lines are saturated and may show self-absorption; hence, we cannot measure the correct ΔV.

In some cases the difference is much larger due to the presence of multiple peaks, which are not resolvable in ^{12}CO. For example S175B-C1 presents a broadened spectrum in ^{12}CO with ΔV_{12}=8.68 km s^{-1}. This spectrum is divided into three peaks in ^{13}CO with the main peak ΔV_{13}=1.44 km s^{-1} which is six times smaller than ΔV_{12}. As a result, the calculated Virial mass using ^{12}CO(2-1) line width, $M_{vir}(^{12}\mathrm{CO})$, is overestimated by a factor of ~ 36. $M_{vir}(^{13}\mathrm{CO})$, which is calculated using ΔV_{13}, then is the best estimation if the cloud is in Virial equilibrium. However, we note that self-absorption can be seen in a few

cases for the optically thinner line of ^{13}CO. $M_{vir}(^{13}\mathrm{CO})$ ranges between 3.5-24.9 $M_{\odot}$ for S175A, and between 17-62 $M_{\odot}$ for S175B. In the case of self-absorbed or multiply peaked lines, we are measuring too large a line width and consequently overestimating the Virial masses.

Velocity Integrated Mass

In the case of the optically thick ^{12}CO emission we can calculate the column density from the empirical relation $N(H_2) = X \times \int T_{mb}(^{12}CO)dv$, with $T_b = T_a^*/\eta_b$. For the JCMT, $\eta_{mb} = 0.69$ is the beam efficiency at the observed frequency range. X is an empirical factor which gives the ratio of the H_2 column density to the integrated intensity of ^{12}CO(1-0). Both theory (Bell et al. 1996) and observation (Pineda et al. 2008) indicate that the "X-factor" is sensitive to variations in physical parameters, such as density, cosmic ionization rate, cloud age, metallicity and turbulence. The "X-factor" also depends on the cloud structure and varies from region to region. Studies (e.g. Pineda 2008, and references therein) have shown that the X value is roughly constant for the observed Galactic molecular clouds, and is currently estimated at $X \simeq 1.9 \pm 0.2 \times 10^{20}$ cm^{-2}(K km s^{-1})$^{-1}$ for ^{12}CO(1-0) (Strong & Mattox 1996). We use ^{12}CO(2-1) and so need to correct this factor. Using a ^{12}CO(1-0) point observation (Blitz et al. 1982) and the ^{12}CO(2-1) smoothed to the ^{12}CO(1-0) beam size (2.3′), we calculated a ratio of ^{12}CO(2-1)/^{12}CO(1-0) = 0.8, which is identical to the value found by Brand & Wouterloot (1998) in a larger sample.

$\int T_{mb}(^{12}CO)dv$ is derived by integrating over all pixels within an ellipse best-fitted to the half highest peak contour (Figures 2.3 and 2.5). About 90% of the integrated flux lies within this ellipse for most of the individual distinct clumps. Adjacent or combined clumps (C5, C6 and C9 within S175A and C10-C11 within S175B) have overlaps and the common area between two fitted ellipses has been integrated for both. For a few extended bright clumps (C5, C6, C8 and C9 in S175A and C5 and C10 in S175B) we have considered the ellipse fitted to the 3σ ($\sim$5 K) contour to define the edges of the clump which contains the $\sim$90% of the integrated flux.

The integrated mass is determined by:

$$M_{int}^{12} = D^2 m_H \mu \times X \int T_{mb}(^{12}CO)dvdA\,, \tag{2.6}$$

where D is the distance, m_H is the mass of a hydrogen atom, and μ= 2.33 is the mean molecular weight for H_2 with a 25% mass fraction of Helium. The calculated M_{int} ranges from 4.1 to 19.4 $M_\odot$ for clumps in S175A, and from 8.9 to 31.4 $M_\odot$ for clumps in S175B.

LTE Mass

The column density can also be calculated from the optically thin ^{13}CO(2-1) line under the assumption of LTE (Rohlf & Wilson 2004):

$$N(^{13}CO) = 1.5 \times 10^{14} \frac{T_{ex} exp(T_{0(\nu_{10})}/T_{ex}) \int \tau^{13}(v) dv}{1 - exp(-T_{0(\nu_{21})}/T_{ex})}. \quad (2.7)$$

where $T_{0(\nu_{10})} = h\nu/k$ with $\nu_{10} = 110.201$ GHz for ^{13}CO(1-0) and $\nu_{21} = 220.399$ GHz for ^{13}CO(2-1). When using the LTE model, we assume that T_{ex}^{12}=T_{ex}^{13} and that the excitation temperature is the same over the entire cloud. For optically thin lines, integrals involving $\tau(v)$ can be approximated by integrated line intensity

$$T_{ex} \int \tau(v) dv \simeq \frac{\tau}{1 - exp(-\tau)} \int T_{mb}(v) dv. \quad (2.8)$$

Assuming $N(H) \simeq 10^6 \times N(^{13}CO)$ (Pineda et. al. 2008), the clump mass using the ^{13}CO column density is then calculated as:

$$M_{LTE} = \frac{\pi}{3} R_e^2 m_H \mu N(H). \quad (2.9)$$

M_{LTE} ranges from 0.6 to 14.8 $M_\odot$ for S175A clumps and from 1.9 to 13.1 $M_\odot$ for S175B clumps.

Jeans mass

Assuming that the kinetic temperature, T_K, of the gas is equal to T_{ex}, the Jeans mass is given by

$$M_J = 1.0 M_\odot \left(\frac{T_K}{10K}\right)^{3/2} \left(\frac{n_{H_2}}{10^4 cm^{-3}}\right)^{-1/2}. \quad (2.10)$$

Only the thermal pressure is considered in the calculation of the Jeans mass, while some agent, such as turbulence and/or internal dynamics, and magnetic fields may act to support the clump against gravitational collapse. If that is the case, then M_{Vir} and M_{int} will be larger than M_{Jeans}. The clumps in S175A have a slightly larger M_{Jeans} than those in S175B (4.3-12.7 $M_\odot$ versus 2.8-10.2 $M_\odot$). The Jeans masses for each region have been listed in Tables 2.5 and 2.6.

2.6 Discussion

The primary goal of this study is to investigate how the physical properties of this molecular cloud have been affected by the S175 H II region. We have selected two different areas: S175A, adjacent to the H II region, and S175B, which is distant enough that it is unlikely to be affected by the ionized gas around the exciting star. We have measured and calculated different physical parameters for two regions and will compare them in this section and discuss how they may have been affected by external sources of turbulence such as the S175 H II region.

2.6.1 Comparison of the Properties of S175A and S175B

Structure: The observed regions show significantly different structures. S175A, which appears to be affected by ionized gas, has an elongated structure and is fragmented into clearly identified distinct clumps, while S175B is very uniform and the clumps within it are less easily identified due to an underlying extended ^{12}CO emission. The extended gas in S175B displays uniformly narrow lines ($\Delta V \sim 1$ km s^{-1}) of $^{12}T_a^* \sim 5 - 7$ K.

Temperature: S175A contains clumps with higher gas temperatures: $^{12}T_a^*$ and $^{13}T_a^*$ range between 9.6-29.1 K and 1.86-17.34 K, respectively, for clumps within S175A, versus 9.2-16.8 K and 2.65-6.42 K for clumps within S175B. Calculated excitation temperature is larger for both regions; T_{ex} varies between 19.1-47.7 K for clumps within S175A and 18.5-29.8 K for S175B. This temperature range is higher than what we expected for S175B as this region is too distant to be warmed up by the H II region. The hottest clumps within S175A (C5, C6, C8 and C9) lie at the edge of the H II region and appear to have been warmed by the star exciting the H II region. These clumps also have higher column densities (105.9-290.4 $\times 10^{20}$ cm^{-2}) than the rest of the S175A region (13.28-82.4 $\times 10^{20}$ cm^{-2}), and these densities are also larger than the column densities of the clumps within S175B (33.83-100.9 $\times 10^{20}$ cm^{-2}).

Size and Mass: The clumps identified within S175B have larger sizes (0.14-0.34 pc) than the S175A clumps (0.12-0.22 pc). It was more difficult to identify the boundary of the clumps within S175B, especially for the colder ones (C3, C4, C7, C8 and C11), because of the extended gas emission with the temperature of the clumps' defined edge temperature ($\sim$ 5 K). Any inaccuracy in boundary selection, which highly affects the estimated size of the clump, can produce significant uncertainty in the mass estimation. It is common in molecular clouds studies to define the edge of the clumps based on a detection level above the background (see §2.6.3). We were unable to use this boundary selection because of the extended ^{12}CO(2-1) emissions in S175B, which cover $\sim$ 80% of the mapped region. Therefore we determine clump boundaries based on the half of the peak temperature. This boundary selection accounts for up to 90% of the total flux (where the boundary is selected to be the background) of the clearly identified clumps within S175A.

We note that some of the clump masses might be overestimated for the smallest clumps in our sample as the lower limit to our clump size is given by our beam size (0.11 pc at 1.09 kpc) and therefore the masses found for these clumps are upper limits. We note that less than one third of our clumps are affected by this issue.

In addition, saturation and self-absorption, especially in ^{12}CO(2-1) emission lines which results in measuring larger line widths, are other sources of inaccuracy in the mass calculation. This effect leads to a significant overestimation

of the Virial mass (up to a factor of 60 for M_{Vir}^{12} compared to M_{Vir}^{13}) and M_{Vir}^{12} is found to be much larger (up to a factor of 600) compared to the calculated M_{LTE}. The M_{Vir}^{12} masses are therefore neglected in the rest of this study.

^{13}CO(2-1) is an optically thinner line and consequently less saturated or absorbed. However, it is also dependent on the $(\Delta V)^2$ and thus is highly dependent on internal dynamics. M_{Vir}^{13} is consistent with M_{int} for S175A, indicating that most of these clumps are close to Virial equilibrium, but it is noticeably larger than M_{int} for S175B clumps. M_{LTE}, which is independent of the cloud dynamics and directly measures the column density, is the smallest calculated mass. In following section we compare these masses to examine the effect of the gas internal dynamics on mass estimation.

Reviewing the above, we can see that the properties of the clumps in the molecular cloud, associated with S175 H II region, are different from what were expected. We expected more turbulence and internal motion within S175A due to the proximity of the H II region. Indeed, we find that S175A contains the clumps with the highest temperature and the largest column densities (C5 and C6); these clumps lie at the edges of the H II region and are likely to be material that has been swept up by the expansion of the ionization front and has then condensed. However, S175B displays the wider line profiles and appears more likely to be subject to turbulent motion. Our recent studies of S175B-C1 in ^{12}CO(3-2) (Azimlu, M^{c}Coey & Fich, in prep.) presents strong evidence of an outflow within this clump. We discuss further outflow-driven turbulence and its

observable affects in §2.6.3. Broadening this study to include the third region at the northern part of the cloud, S175C, would give us insight on the impact of the H II region on the molecular cloud associated with it.

2.6.2 Mass Distribution in the S175 Molecular Cloud

An FCRAO CO(1-0) Survey of the Outer Galaxy (Heyer et al. 1998) provides us with a further opportunity to investigate the large scale structure and mass within the region. This data covers an area much larger than the molecular cloud associated with the S175 H II region which guarantees that we have not missed edges of the cloud, but it has lower spatial ($50''$) and frequency ($\sim$1 km s^{-1}) resolution.

From the data of Heyer et. al. (1998) we find that the molecular material associated with the H II region is reasonably compact and, with a velocity range of -40 km s^{-1} to -60 km s^{-1}, is distinct from the background emission, which has a V_{LSR} of $\sim 0-20$ km s^{-1}. Figure 2.10 shows a map of the molecular cloud, integrated from the FCRAO data between -40 km s^{-1} to -60 km s^{-1} and we calculate the integrated mass in this molecular cloud to be $\sim$ 550 M$_{\odot}$. The integrated mass condensed in clumps from JCMT observations within S175A and S175B totals 355 M$_{\odot}$, so 65% of mass in the cloud is in dense clump form. This is higher than the typical star formation efficiency ($\sim$ 30%, Alves et al. 2007) and is likely a consequence partly of the overestimation of the size of some clumps but also of the overestimation of M_{int}^{12} due to broadened line profiles.

On the other hand only a fraction of the clump mass may end up in a proto-star but we can not resolve stellar-mass cores within our data . Indeed, the total M_{LTE} for the region is 88 $M_{\odot}$, which is 16% of the mass in the molecular cloud and closer to the typical value.

It is possible that we have not accounted for all the material in the region, or maybe part of the initial mass is missed. Fich & Rodulph (in prep.) calculated a total mass of 0.4 $M_{\odot}$ for the ionized gas which accounts only for a very small fraction of the total mass. We do not have any direct estimation of the atomic hydrogen mass but the atomic hydrogen, which lies in a thin layer around the ionized front, cannot contribute significantly (less than 1%) to the mass of the cloud (Krco et al. 2008).

The velocity range within the S175 cloud is found to be -47 to -53 km s^{-1}. In comparison, Fich et al. (1990) measured the ionized gas toward the S175 H II region to be at -55 km s^{-1}, indicating that the ionized gas is expanding toward us with a velocity of $\sim$5 km s^{-1}. Assuming that the ionized gas has been expanding with the same velocity to its present size (0.63 pc in diameter) it is $\sim 6 \times 10^4$ years old. Since the expansion velocity decreases with time, this age is an upper limit and swept up material cannot have been ejected from the cloud within this short time scale. We conclude that the material around the S175 H II region contains more massive clumps than is typical but cannot, with this data, explain why.

As an aside, it is interesting to note that, contrary to the general belief that

massive stars form within Giant Molecular Clouds (GMCs) with typical mass of $10^4 - 10^5 M_\odot$, here we find a ≈ 10 $M_\odot$ B1.5V star has been formed within a relatively small cloud with total mass of only 550 $M_\odot$.

2.6.3 The Effect of Line Width

Line width and mass estimates

Some mass estimation methods such as the Virial and ^{12}CO velocity-integrated masses depend on line profile and width, which are highly sensitive to cloud kinematics. The LTE analysis directly measures column density and is independent of line profile, and therefore of turbulence and internal dynamics. As a result, comparing masses estimated by these different methods enables an evaluation of turbulence and kinematics of the clumps.

In Figure 2.7 we compare M_{int}^{12} and M_{Vir}^{13}. The solid line is the linear least-squares fit and the line of equality is marked by long dashes. In S175A M_{int}^{12} and M_{Vir}^{13} are almost equal (left panel), indicating that clumps within S175A are close to Virial equilibrium.

The clumps in S175B display larger line widths than those in S175A and have larger velocity-integrated and Virial masses as a result. The right panel in Figure 2.7 shows that there is a weak relation between Virial and velocity-integrated mass in S175B.

An important point to note from this figure is that S175B is clearly not in Virial equilibrium.

We can investigate further this issue by plotting the LTE masses against M_{Vir}^{13} (Figure 2.8) and against M_{int}^{12} (Figure 2.9). These Figures show that the LTE masses found are slightly smaller than either the Virial or integrated-velocity masses for S175A but noticeably smaller for S175B. In fact, the Virial masses in S175B are up to a factor of 20 larger than M_{LTE}. It is possible that the LTE analysis may underestimate the mass because of self-absorption and saturation of the line profiles, this is especially true in S175B where most of the strongest emission lines are self-absorbed or distorted by internal dynamics, even for ^{13}CO(2-1). However, we note that the ratio of M_{int}^{12} to M_{LTE} for S175B-C1, -C2 and -C3, which show evidence of infall and outflow, is the greatest among all the clumps in the S175 region. We may conclude that M_{int}^{12} is overestimated for all dynamically active clumps.

Line width-clump size relation

Various studies of molecular cloud clump/cores have examined the relation between line width and clump/core size (e.g., Larson 1981, Solomon et al. 1987, Lada et al. 1991, Simon et al., 2001) and a power law, often known as the Larson relation, is reported:

$$\Delta V \propto r^{\alpha}, \qquad 0.15 < \alpha < 0.7. \tag{2.11}$$

This relation has been observed over a large range of clumps/cores, from smaller than 0.1 pc up to larger than 100 pc, which suggests a natural origin. However, the physical process that results in the relation is still undetermined.

In Figure 2.11 we plot the log of ^{12}CO(2-1) and ^{13}CO(2-1) velocity dispersion versus the effective clump radius in order to investigate the Larson relation in S175. A least square analysis shows a weak relation in S175A with $\alpha = 0.9$ for ^{12}CO and $\alpha = 0.7$ for ^{13}CO but no correlation is seen for S175B. This is not unprecedented: Lada et.al. (1991) suggested that the existence of the relation is highly affected by the way clumps are defined and selected. They identified clumps from a survey in the Orion B molecular cloud as having 3σ and 5σ boundary above the noise, and found a weak relation for the 5σ clumps, but no apparent relation for 3σ clumps. More recent studies in the Galactic plane have also indicated a weak or highly scattered relation (Simon et al. 2001). Although we base our boundary selection on the peak temperature within a clump rather than on a level above the background, we see a poor correlation between size and line width for S175A clumps, however, no correlation is found for S175B.

The possible impact of the broadened line profiles in S175B is intriguing. In a study of cloud cores associated with water masers, Plume et al. (1997) noted that the line width-size relation breaks down in massive cores which systematically have higher line widths. Line widths larger than that expected from thermal motions are thought to be due to local turbulence (Zuckerman &

Evans, 1974). Matzner (2007) modelled outflow-driven turbulence from protostars and found that at scales much smaller than the turbulent driving scale the Larson relation is obtained. At larger scales, however, the line width-size relation flattens in a similar way to that seen in the right panel of Figure 2.11. Our recent observations in ^{12}CO(3-2) of S175B-C1, show strong signatures of an outflow in this clump (Azimlu, M^{c}Coey & Fich, in prep.). The feedback from this outflow is a possible source of turbulence in S175B, at least in the North-Western part of the cloud. Presence this outflow indicates that S175B is an active star-forming region and older outflows of recently formed stars could be responsible for the observed structure and kinematics of this cloud.

2.7 Summary and Conclusions

The CO observations presented here show the presence of a small molecular cloud adjacent to the S175 HII region. We mapped two $7' \times 7'$ areas in ^{12}CO(2-1) within the cloud. We selected these two regions, S175A and S175B, to investigate the impact of the H II region on the physical properties of the molecular cloud. Remarkably, these two regions have a very different morphology; S175A is close to the HII region and has a clearly defined, clumpy structure that lies over the HII region at South-East, while the more distant S175B is more uniform but with three clumps that show signatures of outflow. We studied the clumpy structure of the cloud and identified 13 clumps within S175A and 12

within S175B. We then used pointed observations in ^{13}CO(2-1) at the brightest peak of ^{12}CO(2-1) within each clump in combination with the ^{12}CO(2-1) spectrum parameters to measure and calculate the physical parameters of the clouds. Our findings are summarized below:

1. S175A contains warmer clumps than S175B. The most likely explanation for this is that S175A has been heated by the H II region. However S175B is also hotter than might be expected, probably because of the on-going star formation.

2. The line widths are much larger for clumps within S175B than S175A. Comparison of ΔV_{13} with thermal line widths

   shows that S175A has not been much disturbed by the H II region, while S175B clearly displays non-thermal motions that are most likely the result of an outflow. In addition to displaying broad line profiles in ^{12}CO, the ^{13}CO spectra from S175B are split into multiple peaks.

3. Clumps within S175B are generally larger. We suggest that clumps within S175A may be partially a product of the "collect and collapse" effect of ionization fronts from the H II region, while a source of turbulence, possibly the outflow, supports the gas within S175B against fragmentation and gravitational collapse.

4. We determined the Virial, LTE and velocity integrated masses using both ^{12}CO and ^{13}CO lines. M_{Vir}^{12} is over-estimated due to broadened line pro-

files and is not included in our analysis. We find that $M^{13}_{Vir} > M_{int} > M_{LTE}$ in all clumps, which highlights the influence of line width on the mass estimation. A clear relation between M^{13}_{Vir} and M^{12}_{int} in S175A indicates that most of the clumps are in Virial equilibrium within this region. No such relation is found for S175B.

5. We investigated the size-line width relationship for clumps and found a weak relation for clumps within S175A. No relation was found for S175B clumps, which may be a result of a local source of turbulence, due to the outflow, or may be a consequence of the confusion of the clump edges with underly extended gas in S175B.

6. Observations of massive star-forming regions indicate that massive stars originate within Giant Molecular Clouds. However, the molecular cloud associated with the S175 H II region is a small, distinct cloud with total mass of 550 $M_\odot$ and it hosts a $\sim 10M_\odot$ B1.5V star. Upto 65 percent of the cloud mass is located within the condensed clumps.

We compare the structure and gas properties of these two regions to investigate how the molecular gas has been affected by the H II region. S175A has been heated by the H II region and partially compressed by the ionized gas fronts, but contrary to our expectation it is a quiescent region while S175B is very turbulent and dynamically active. Consequently, we have been able to investigate the influence of turbulence on commonly used mass estimates and

line width-size relation. We detected an outflow within S175B which is likely to be the source of turbulence that supports the cloud against gravitational collapse and causes the observed uniform structure within S175B.

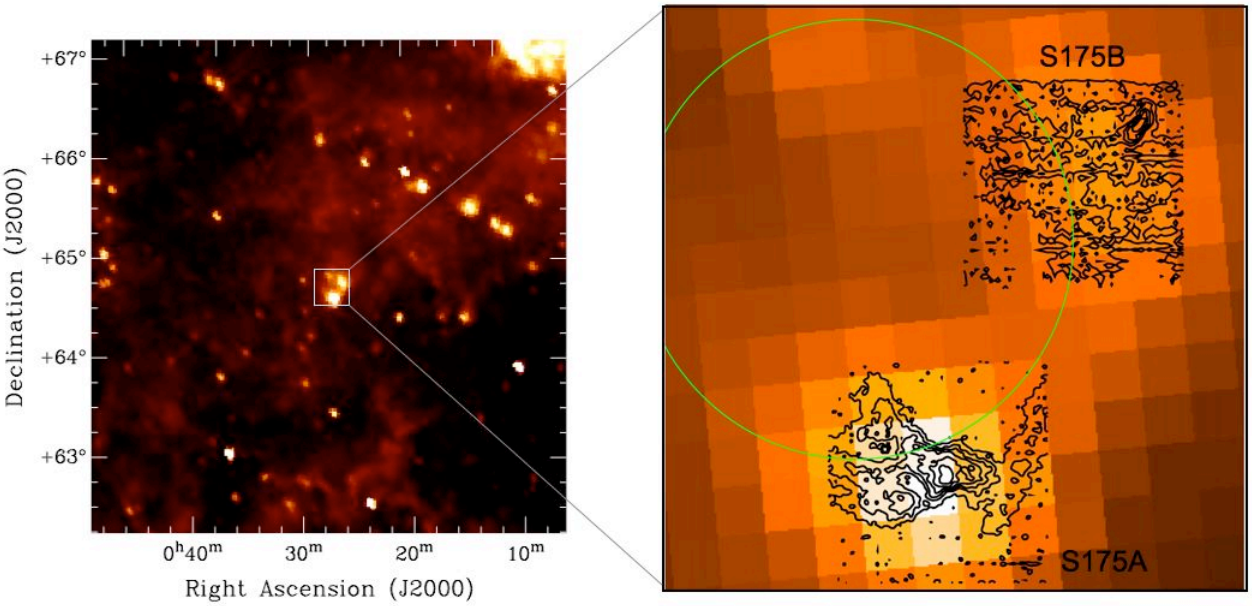

Figure 2.1 Position of the S175 region in IRAS 12 μm map. Three condensations along a ring (shown in green) have been identified. The ring structure has also been observed at AMI 15.8 GHz (Scaife et al. 2008). Overlaid contours of integrated ^{12}CO(2-1), shows the two $7' \times 7'$ observed regions. S175A is adjacent to the H II region while S175B lies at a distance of $\sim 10'$ ($\sim$ 3 pc).

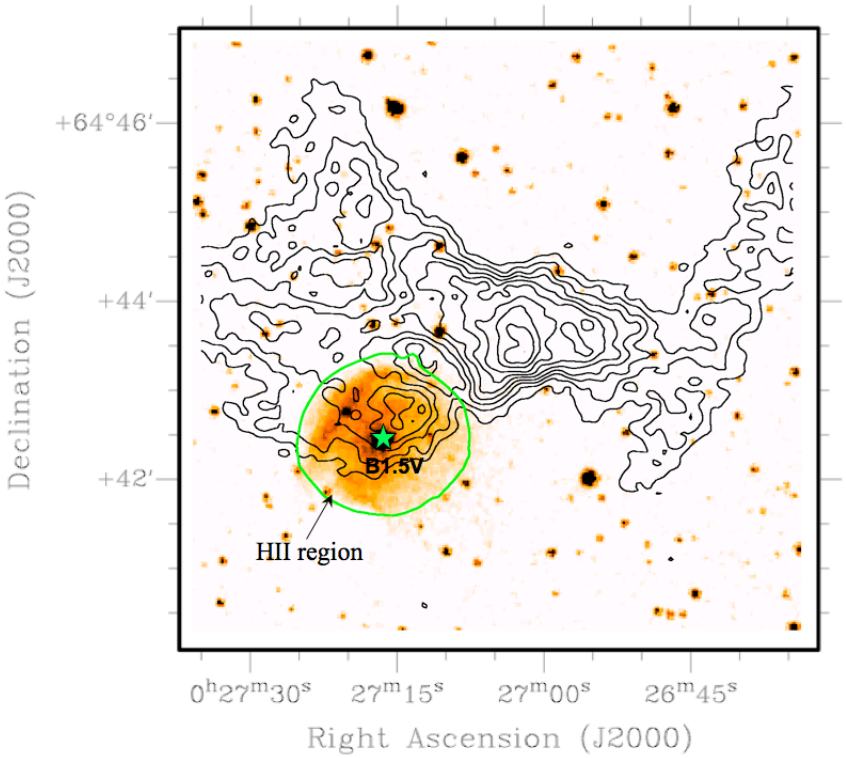

Figure 2.2 : S175A integrated molecular gas contours overlaid on an optical image from the Digital Sky Survey of the H II region S175. The visible borders of the H II region are shown in green and the central bright source is a B1.5V star. The S175A molecular gas forms a wedge-shaped structure that overlays the H II region at the South-East plus a filament that leads to the north-west.

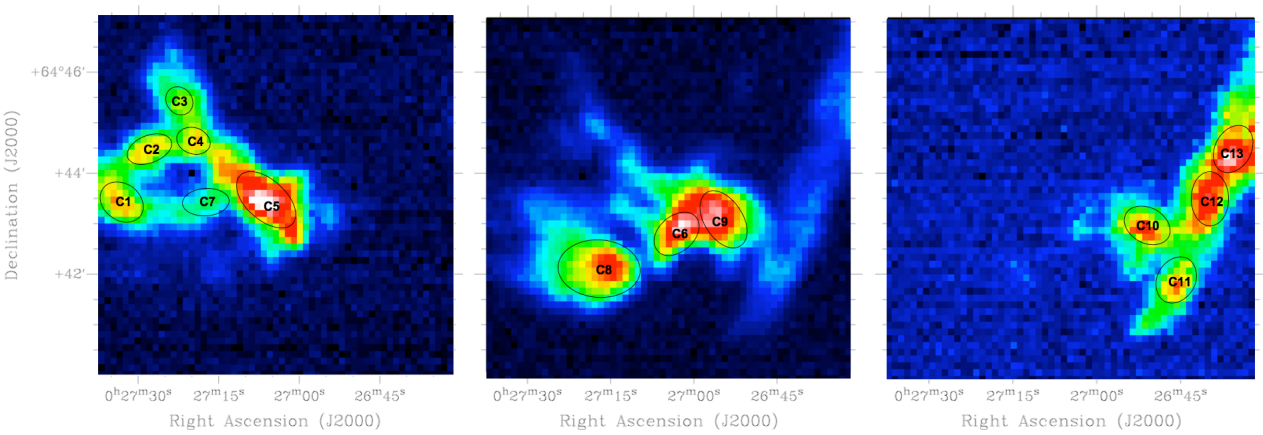

Figure 2.3 : S175A integrated over -48 km s^{-1} to -49.5 km s^{-1} (left), -49.5 km s^{-1} to -50.5 km s^{-1} (middle) and -50.5 km s^{-1} to -52 km s^{-1} (right). We detected 13 distinct clumps within this cloud. The position and other observed physical properties of each clump are listed in Table 2.1.

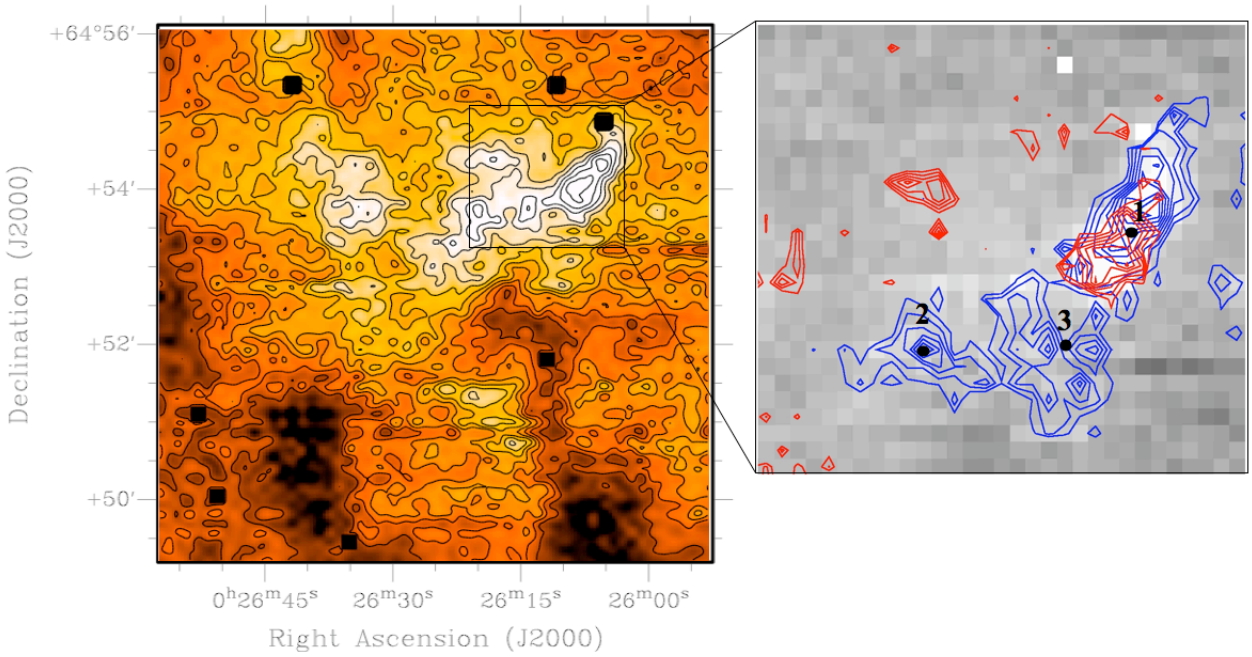

Figure 2.4 : S175B ^{12}CO(2-1) map integrated between -47 km s^{-1} and -53 km s^{-1}. Three dense clumps within the box show evidence of outflow (notice the wide double peaked spectra for these clumps in Figure 2.6). The red contours integrated over -47 to -48 km s^{-1} and blue contours over -53 to -54 km s^{-1}. Our recent observations in ^{12}CO(3-2) (Azimlu, M^{c}Coey & Fich, in prep.) show strong signature of an outflow in C1. The rest of the cloud is uniform and lies on extended diffuse gas with a temperature of $^{12}T_a^* \sim 5 - 7$ K.

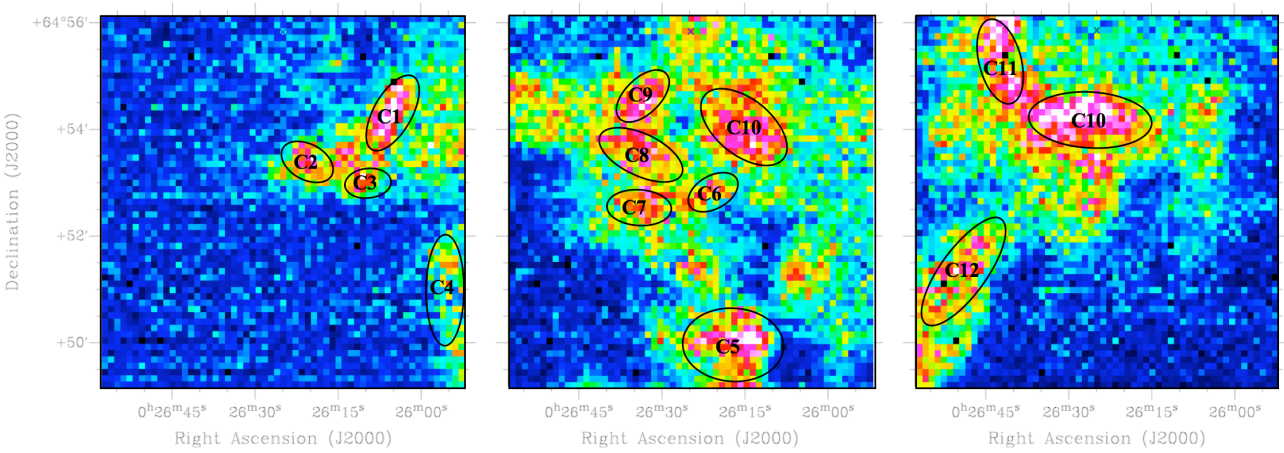

Figure 2.5 S175B ^{12}CO(2-1) map integrated over -47 km s^{-1} to -49 km s^{-1} (left), -49 km s^{-1} to -51 km s^{-1} (middle) and -51 km s^{-1} to -53 km s^{-1} (right). It was more difficult to identify clumps in S175B because of extended gas with $^{12}T_a^* \sim 5-7K$. We detected 12 distinct clumps within this cloud. The position and other observed physical properties of each clump are listed in Table 2.2.

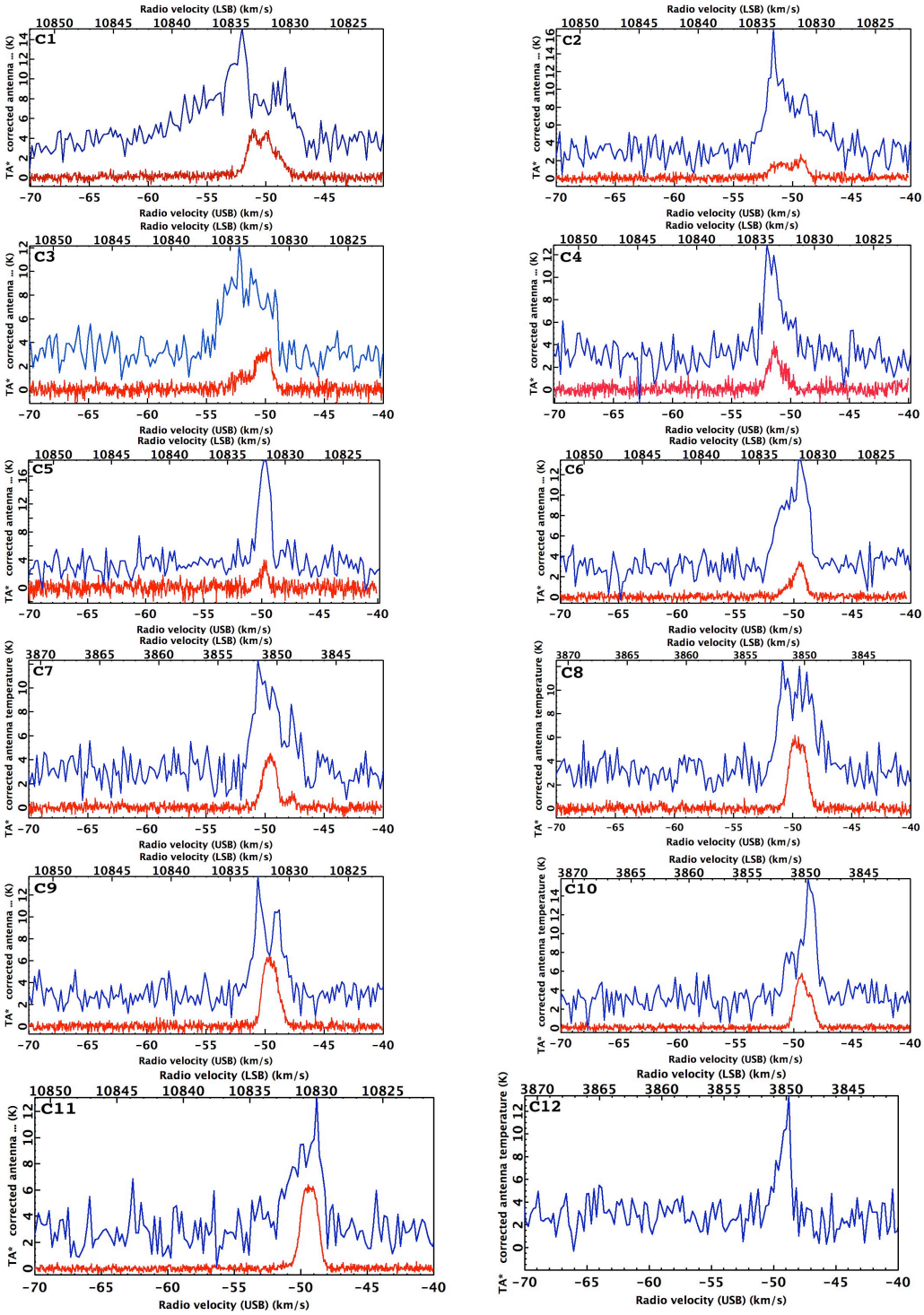

Figure 2.6 ^{12}CO(2-1) (blue spectra) and ^{13}CO(2-1) (red spectra). For clarity, the ^{12}CO(2-1) profile has been shifted upwards by 3 K. Note the broad, distorted lines in C1-C3 which are representative of an outflow. Strong self absorption is seen in C8 and C9. C12 is yet to be observed in ^{13}CO(2-1) (see Figure 7 for C11 and C12).

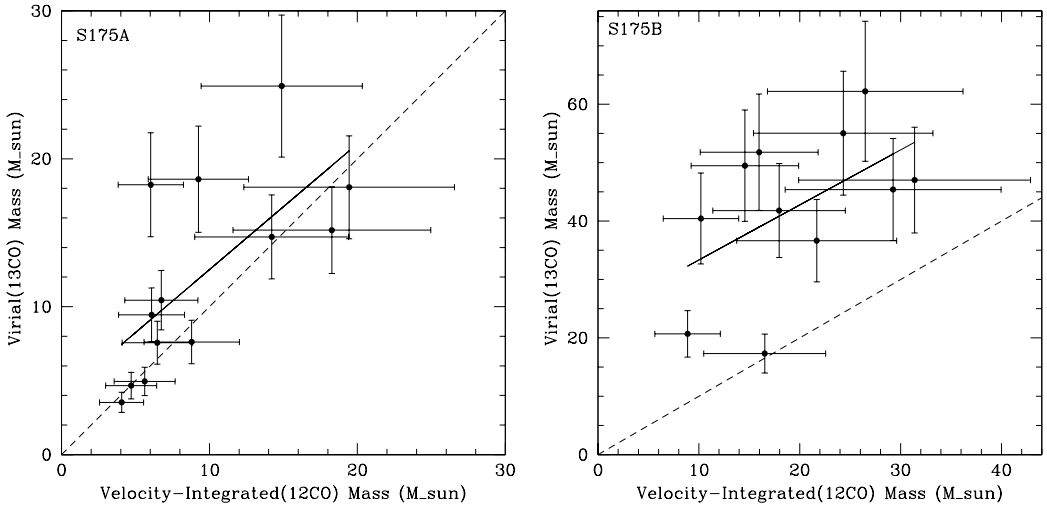

Figure 2.7 ^{13}CO Virial mass versus velocity integrated mass, M_{int}^{12} for S175A (left) and S175B (right). The solid line is the least squares fit and the long-dashed line indicates the line of equality. Most of the clumps within S175A are in Virial equilibrium. Clumps within S175B are dynamically active and not in a Virial equilibrium.

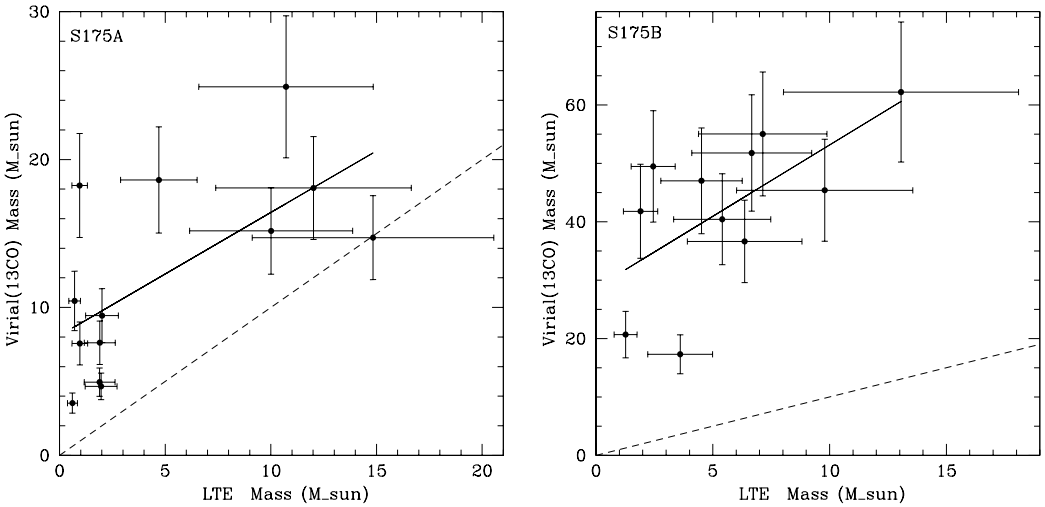

Figure 2.8 ^{13}CO Virial mass versus LTE mass for S175A (left) and S175B (right). The dashed line indicates the line of equality. Most of the clumps are over-Virialized compared to LTE mass for both regions but within S175B M_{Vir}^{13} is noticeably larger than M_{LTE} up to a factor of 20.

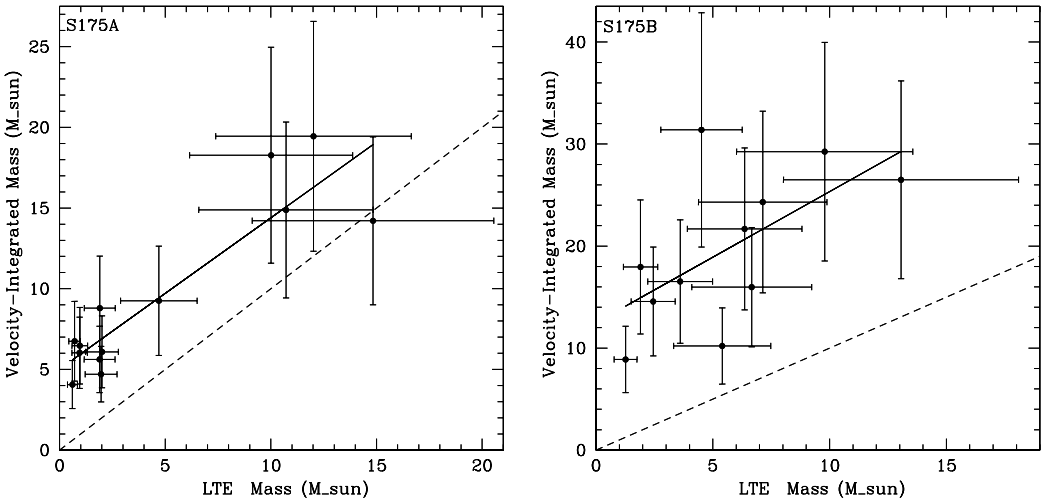

Figure 2.9 Velocity integrated mass versus LTE mass. The dashed line indicates the line of equality. M_{int}^{12} mass is slightly larger than the M_{LTE} for S175A but noticeably larger for S175B.

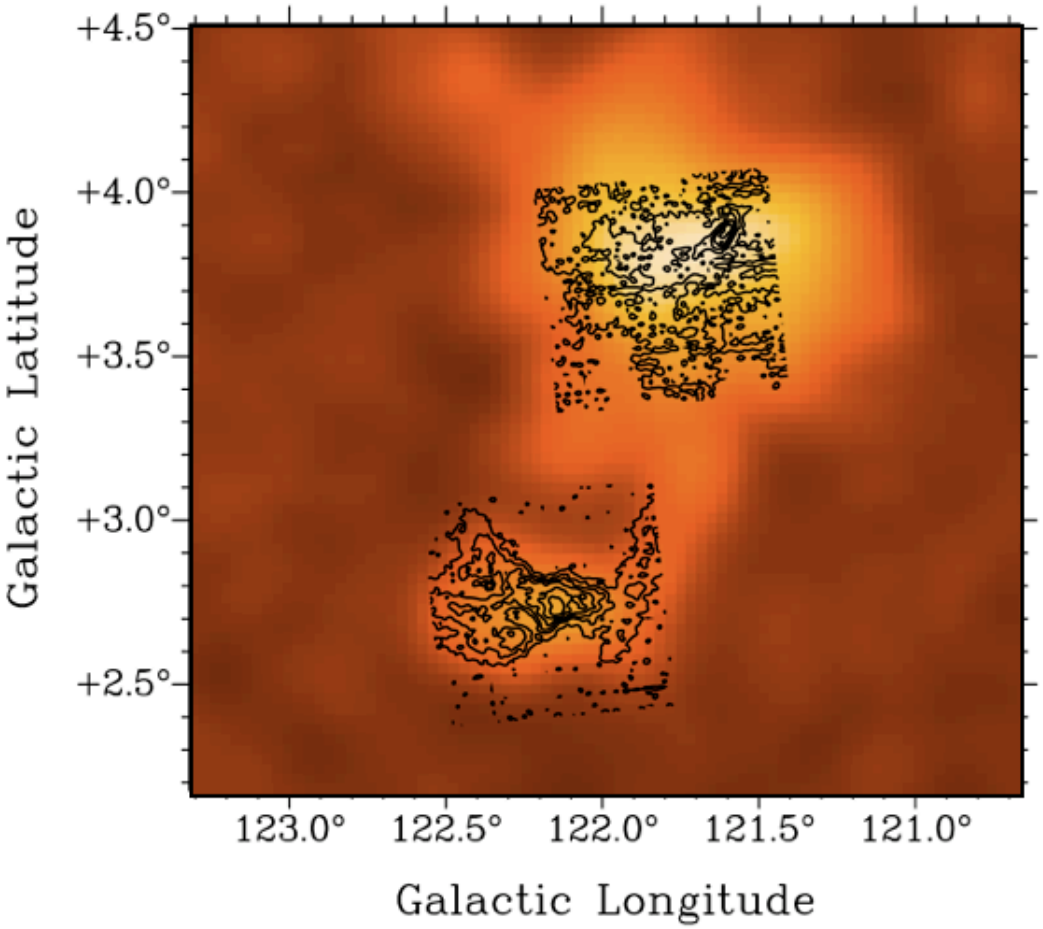

Figure 2.10 FCRAO ^{12}CO(1-0) map integrated between -40 and -60 km s^{-1}. Black contours show the mapped regions in ^{12}CO(2-1) in our study.

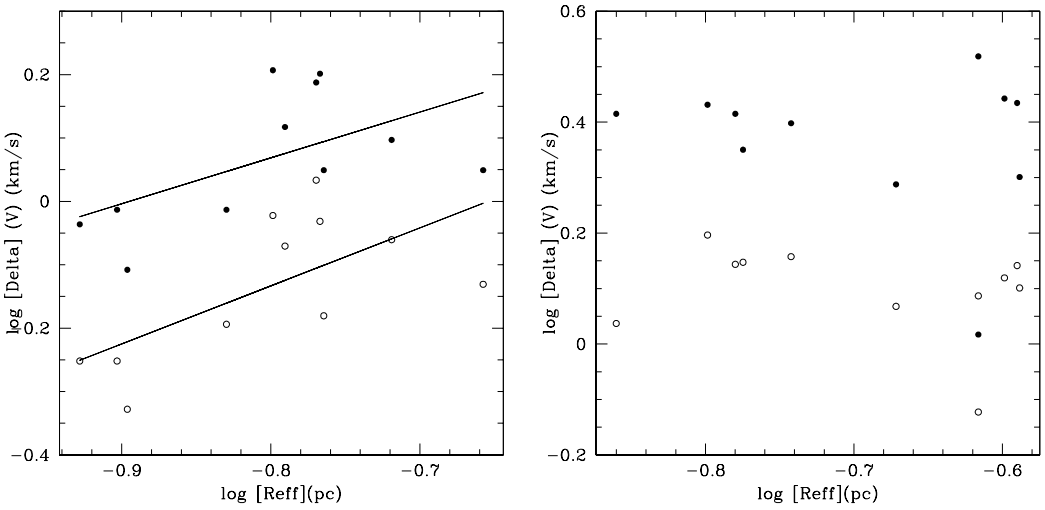

Figure 2.11 Line width is weakly correlated with size for S175A clumps (left panel) but no correlation is seen for S175B clumps (right panel).

Table 2.1. Physical parameters measured for S175A clumps

ID	Position (X,Y)	RA	DEC	R_e (pc)	$^{12}T_a^*$ (K)	$^{13}T_a^*$ (K)
C1	(07,31)	00:27:29.63	+64:43:41.30	0.13±0.024	19.59	8.41
C2	(08,38)	00:27:27.47	+64:44:45.21	0.13±0.024	15.86	4.00
C3	(14,47)	00:27:22.02	+64:45:34.30	0.17±0.033	12.27	5.14
C4	(16,41)	00:27:19.81	+64:44:52.34	0.12±0.023	18.77	9.45
C5	(30,32)	00:27:04.62	+64:43:49.51	0.16±0.031	29.09	17.34
C6	(32,29)	00:27:02.30	+64:43:28.53	0.16±0.031	28.42	14.40
C7	(08,31)	00:27:28.53	+64:43:42.19	0.15±0.028	20.60	5.75
C8	(20,23)	00:27:15.40	+64:42:46.60	0.22±0.042	23.22	9.86
C9	(38,29)	00:26:55.74	+64:43:35.58	0.17±0.033	21.20	11.59
C10	(42,30)	00:26:51.37	+64:43:35.58	0.17±0.033	14.95	7.41
C11	(47,21)	00:26:41.53	+64:42:32.59	0.19±0.037	10.80	1.86
C12	(51,30)	00:26:41.53	+64:43.35.58	0.16±0.032	10.89	2.26
C13	(55,39)	0:26:37.153	+64:44:38.57	0.16±0.030	9.58	3.61

Table 2.2. Physical parameters measured for S175B clumps

ID	Position (X,Y)	RA	DEC	R_e (pc)	$^{12}T_a^*$ (K)	$^{13}T_a^*$ (K)
C1	(48,45)	0:26:05.41	+64:54:20.87	0.18± 0.04	12.10	4.90
C2	(35,38)	0:26:19.70	+64:53:32.71	0.14± 0.03	13.81	2.65
C3	(43,34)	0:26:10.90	+64:53:03.86	0.11± 0.02	9.16	3.54
C4	(57,19)	0:25:55.52	+64:51:18.84	0.26± 0.05	9.87	4.28
C5	(37,19)	0:26:17.49	+64:51:18.84	0.24± 0.05	16.82	3.98
C6	(32,32)	0:26:23.00	+64:52:49.81	0.14± 0.03	10.42	3.46
C7	(22,32)	0:26:33.99	+64:52:49.71	0.25± 0.05	9.33	4.51
C8	(24,37)	0:26:31.80	+6:53:24.73	0.24± 0.05	9.53	6.16
C9	(23,46)	0:26:32.92	+64:54:27.72	0.26± 0.05	10.71	6.42
C10	(27,43)	0:26:28.51	+64:54:06.77	0.21± 0.04	12.87	5.76
C11	(16,50)	0:26:40.63	+64:54:55.63	0.17± 0.03	10.09	6.34
C12	(7,19)	0:26:50.44	+64:51:18.64	0.32± 0.06	10.38	...

Table 2.3. Physical parameters derived for S175A clumps

Clump No.	T_{ex} (K)	V_{12} (kms^{-1})	V_{13} (kms^{-1})	ΔV_{12} (kms^{-1})	ΔV_{13} (kms^{-1})	$N(H)$ ($\times 10^{20} cm^{-2}$)	$n_{int}(H_2)$ ($\times 10^{3} cm^{-3}$)	τ_{12}	τ_{13}
C1	33.83	-49.39	-49.14	0.97	0.56	61.83	6.2	34.44	0.56
C2	28.36	-48.98	-49.03	0.78	0.47	19.38	4.3	17.85	0.29
C3	23.08	-49.39	-49.03	1.12	0.66	34.68	2.6	33.22	0.54
C4	32.63	-49.39	-49.14	0.92	0.56	72.12	6.2	42.99	0.69
C5	47.68	-49.39	-49.35	1.31	0.85	290.4	7.3	55.79	0.90
C6	46.70	-49.79	-49.67	1.61	0.95	243.4	10.5	43.52	0.70
C7	35.31	-49.39	-49.56	0.97	0.64	44.75	6.0	20.13	0.32
C8	39.13	-50.00	-49.99	1.12	0.74	105.9	3.7	33.99	0.55
C9	36.18	-50.20	-49.67	1.54	1.08	190.8	6.6	48.59	0.78
C10	27.03	-50.81	-50.52	1.59	0.93	82.41	4.0	41.94	0.68
C11	20.90	-50.81	-50.62	1.25	0.87	13.28	1.9	11.54	0.19
C12	21.04	-50.01	-50.84	1.15	0.71	13.50	3.3	14.21	0.23
C13	19.08	-50.01	-50.94	1.32	0.62	20.09	3.7	28.87	0.47

Table 2.4. Physical parameters derived for S175B clumps

Clump No.	T_{ex} (K)	V_{12} (kms^{-1})	V_{13} (kms^{-1})	ΔV_{12} (kms^{-1})	ΔV_{13} (kms^{-1})	$N(H)$ ($\times 10^{20} cm^{-2}$)	$n_{int}(H_2)$ ($\times 10^{3} cm^{-3}$)	τ_{12}	τ_{13}
C1-a	22.82	-52.03	-51.12	8.68	1.44	70.71	11.6	31.74	0.51
C1-b	22.82	...	-49.79	8.68	1.44	70.71	11.6	31.74	0.51
C1-c	22.82	-52.03	-48.77	8.68	1.72	70.71	11.6	31.74	0.51
C2-a	25.34	-51.62	-51.12	2.24	2.04	34.42	9.6	13.06	0.21
C2-b	25.34	-48.98	-49.29	2.77	1.40	34.42	9.6	13.06	0.21
C3-a	18.47	-52.23	-51.99	2..70	2.11	49.57	9.3	29.81	0.48
C3-b	18.47	-51.22	-50.05	3.11	1.57	49.57	9.3	29.81	0.48
C4	19.52	-52.03	-51.22	2.00	1.26	51.17	2.0	34.70	0.56
C5	29.77	-49.80	-49.75	1.04	0.75	31.58	2.5	16.57	0.27
C6	20.34	-49.39	-49.56	2.60	1.35	33.83	7.3	24.68	0.40
C7-a	18.71	-50.61	-49.57	2.77	1.32	57.44	3.3	40.29	0.65
C7-b	18.71	-47.76	-47.73	2.77	1.95	57.44	3.3	40.29	0.65
C8	19.02	-50.81	-49.49	3.30	1.22	85.83	4.5	63.01	1.02
C9	20.77	-50.61	-49.49	2.72	1.39	100.9	3.4	55.71	0.90
C10	23.95	-48.78	-49.22	1.94	1.51	71.87	4.9	36.30	0.59
C11	19.84	-48.78	-49.30	2.60	0.59	100.7	4.9	60.15	0.97
C12	20.27	-48.78	...	1.13	...	...	0.09	...	...

Table 2.5. Masses calculated for S175A clumps (all in $M_{\odot}$)

Clump	M_{vir}^{13}	M_{int}^{12}	M_{LTE}^{13}	M_{Jeans}
C1	4.9±1	5.6±2.1	1.9±0.7	7.9
C2	3.5± 0.7	4.1±1.5	0.6±0.2	7.3
C3	9.4±1.8	6.1±2.2	2±0.8	6.9
C4	4.7±0.9	4.7±1.7	2±0.8	7.5
C5	14.7±2.8	14.2±5.2	14.8±5.7	12.2
C6	18.1±3.5	19.4±7.1	12±4.6	9.8
C7	7.6±1.5	8.8±3.2	1.9±0.7	8.6
C8	15.2±2.9	18.3±6.7	10±3.9	12.7
C9	24.9±4.8	14.9±5.4	10.7±4.1	8.4
C10	18.6±3.6	9.3±3.4	4.7±1.8	7.0
C11	18.2±3.5	6.0±2.2	0.9±0.4	7.0
C12	10.4±2.0	6.7±2.5	0.7±0.3	5.3
C13	7.6±1.5	6.5±2.4	1±0.4	4.3

Table 2.6. Masses calculated for S175B clumps (all in $M_\odot$)

Clump	M_{vir}^{13}	M_{int}^{12}	M_{LTE}^{13}	M_{Jeans}
C1	47±9.1	31±11.5	4.5±1.7	3.2
C2	42±8.1	18±6.6	1.9±0.7	4.5
C3	50±9.5	15±5.3	2.4±0.9	2.8
C4	52±10	16±5.8	6.7±2.6	6.1
C5	17±3.3	17±6.0	3.6±1.4	10.2
C6	21±4.0	9±3.3	1.3±0.5	3.4
C7	55±10.6	24±8.9	7.1±2.8	4.5
C8	45±8.7	29±10.7	9.8±3.8	3.9
C9	62±12	27±9.7	13.1±5.0	5.1
C10	37±7.1	22±7.9	6.4±2.5	5.3
C11	40±7.8	10±3.7	5.4±2.1	4
C12	...	12±4.5	...	9.8

Chapter 3

Molecular Clouds Associated with H II Regions

3.1 Overview

The properties of molecular clouds associated with 10 H II regions were studied using CO observations. We identified 142 dense clumps within our sample and measured and calculated physical properties of the clumps such as size, excitation temperature, line widths, density and mass. We found that our sources are divided into two categories: those that show a size-line width relation ("type I") and those which do not show any relation ("type II"). Type II sources have larger line widths in general. Investigating the relation between the line width and other parameters shows that while the M_{LTE} increases with ΔV for both ^{12}CO and ^{13}CO lines in type I sources, no relation was found for type II sources.

No relation between column density and line width was found for either category. We also investigated how the characteristics of the clumps vary with distance from the H II region. We found no relation between mass distribution of the clumps and distance from the ionization front, but a weak decrease of the excitation temperature with increasing distance from the ionized gas. No relation was found between line width and distance from the H II region which probably indicates that the internal dynamics of the clumps is not affected by the ionized gas. Internal sources of turbulence, such as outflows and stellar winds from young proto-stars may have a more important role.

3.2 Introduction

Massive stars are believed to form in giant molecular clouds in clusters which themselves formed in dense, massive, turbulent clumps. Clustered star formation is more complicated compared to isolated star formation from individual collapsing cores, and therefore less well understood theoretically. Massive star-forming regions are not as common as low mass star-forming regions and consequently, less populous in nearby clouds. Therefore, high mass star formation has been far less studied in details compared to low mass stars. In regions of high mass star formation it is not only the physical conditions of the molecular clouds that govern the star formation. Newborn stars in these regions also affect their original environment through various feedback mechanisms. Low

mass stars form gently in more quiescent regions and do not significantly affect their environment during their slow formation and evolution process. Contrarily, high mass stars form in turbulent dense cores and evolve very quickly. They influence the environment by strong winds, jets and outflows which change the physical conditions such as temperature and density of the cloud. They also ionize the gas (known as H II regions) that expands into the surrounding cloud. All of these energetic processes near the young massive star affect further star formation.

We are making a detailed examination of the dense gas properties in star-forming regions associated with massive stars in order to investigate how the physical parameters and consequently, star formation have been affected in these environments. Our sample consists of 10 H II regions selected from the Sharpless catalog of H II regions (Sharpless 1959). We have selected objects in the outer Galaxy, primarily along the Perseus arm to minimize the confusion with background sources and to have the best estimate of the kinematic distance for those like S196 which we do not have a direct distance determination by spectrometric study of the exciting star. S104 is the only source with almost the same Galactic orbit as the Sun, but we have direct distance measurement for this object and it satisfies other requirements. All distances are collected from literature and listed by references in Table 3.1.

Some of these regions have been investigated in previous studies and it has been observed that they have complex spatial and kinematic structures

(Hunter et al. 1990). Triggered star formation also has been observed at the peripheries of two sources within our sample (S104 and S212; Deharveng et al. 2003 , 2008). Here we study the properties of the molecular gas in higher resolution and investigate how physical parameters varies due to the influence of the H II region and the exciting star.

For each source we used the James Clerk Maxwell telescope (JCMT) to make $7' \times 7'$ ^{12}CO(2-1) maps around the H II regions to study the clumpy structure of the gas in the associated molecular clouds and to locate the dense cores within the cloud. These maps can be made in poor weather conditions at the JCMT as the emission is very strong. ^{12}CO(2-1) is optically thick and cannot trace the dense gas at the centre of the cores where the star formation actually takes place. Therefore, we need to use pointed observations of an optically thinner emission line such as ^{13}CO(2-1) in the cores to measure physical properties of the dense gas, such as density, temperature, clump masses and velocity structure that affect the star formation process. In particular, the velocity structure and line widths will provide information on the dynamic forcing by the H II region and on the clumps' support mechanisms. We can also get a picture of internal dynamics inside the molecular cloud. Hot clumps that show evidence of outflows can also be found and identified as candidates for proto-stars.

We introduce the sample and present the observational details in §3.3. In §3.4 the observational results and calculated parameters are presented. We

discuss about the relationships between derived physical characteristics in §3.5 and conclusions are summarized in §3.6.

3.3 Sample Selection and Observation

3.3.1 Sample

Observed sources are listed in column one of Table 3.1. Columns two and three present the approximate coordinates of the centre of the mapped region in ^{12}CO(2-1). Column four shows the distance of the source based on the identified exciting star; for S196 no exciting star has been detected and therefore we use its s kinematic distance for this source. In column five we list the radial velocity of each source from the catalog of CO radial velocities toward Galactic H II regions by Blitz, Fich and Stark, (1982). We have selected H II regions with small angular size to be able to map the molecular gas at the edges of the region. Column six presents the angular diameter of optically visible ionized gas. The angular diameter varies between one and seven arc-minutes. Our sources lie at distances between $\approx$ 1 kpc (S175) and $\approx$ 7 kpc (S212). The calculated diameters of the H II regions in our sample vary from smaller than 1 pc for S175 and S192 to 9 pc for S104. The calculated diameters are listed in column seven. In column eight we list the identified exciting stars from the literature.

To investigate the effects of the massive exciting star and the H II region on its environs we compare the molecular gas near the H II region with the gas from parts of the cloud which are distant enough that they are unlikely to be affected. We observed an excellent example of a second distinct and distant component in the molecular cloud associated with S175 (Azimlu et al. 2009, hereafter Paper I). Two components, S175A and S175B, in the molecular cloud have previously been identified in an IRAS survey of H II regions by Chan & Fich (1995). Both regions have the same $V_{LSR} \approx -50$ km s^{-1} and are connected by a recently observed filament of molecular gas with the same velocity. Therefore it is reasonable to assume that S175A and S175B lie at the same distance. We use the results from Paper I as a template to study the properties of the presented clouds in this paper.

3.3.2 Observations with the 15 m JCMT Sub-millimeter Telescope

The observations were carried out in different stages. In this first stage from August to November 1998 we made $7' \times 7'$ ^{12}CO(2-1) maps of S175A, S175B, S192/S193, S196, S212 and S305. The details of these observations have been described in Paper I. Pointed observations in ^{13}CO(2-1) on peaks of identified dense clumps within each region were made from August 2005 to February 2006. In this period we also made a $7' \times 7'$ ^{12}CO(2-1) map of S104 with the same observational settings as in 1998, but due to the large angular size of

this H II region we missed most of the associated molecular gas in our map. Therefore, we decided to extend the S104 map to a larger area.

Further observations were made with the new ACSIS system at the JCMT between October 2006 and January 2009. We extended the S104 map to a $9' \times 9'$ map and made four more $7' \times 7'$ ^{12}CO(2-1) maps: around S148/S149, S152, S288 and S307. Most of the peaks identified in clumps within all sources in our sample were also observed in ^{13}CO(2-1) during four observation missions in this period. In this new configuration with ACSIS, we used a bandwidth of 250 MHz with 8190 frequency channels, corresponding a velocity range of about 325 km s^{-1} for ^{12}CO(2-1) and 340 km s^{-1} for ^{13}CO(2-1) with a resolution of $\sim$0.04 km s^{-1}. We used the Starlink SPLAT and GAIA packages to reduce the data, make mosaics, remove baselines and fit Gaussian functions to determine ΔV, the FWHM of the observed line profiles.

3.4 Results

The physical properties of the clumps are derived from the ^{12}CO(2-1) maps and ^{13}CO(2-1) pointed observations at peaks. We used the ^{12}CO(2-1) maps to study the structure and morphology of the molecular clouds and to identify clumps within them. The cloud associated with each H II region consists of various clumps of gas that display one or more peaks of emission (typically towards the centre of the clump). We define any separated condensation as

a distinct clump, if: 1) the brightest peak within the region has an antenna temperature larger than five times the rms of the background noise; 2) the drop in antenna temperature between two adjacent bright peaks on a straight line in between, is larger than the background noise; and, 3) the size of the condensation is larger than the telescope beam size (21″ or 3 pixels). The edge of a clump is taken to be the boundary at which the integrated intensity over the line drops to below half of the highest measured integrated intensity within that clump. An ellipse that best fits to this boundary is considered to calculate the clump size and total integrated flux measurements.

The positions of the ^{12}CO(2-1) peak of identified clumps in each region and other observed parameters for each clump are listed in Table 3.6. Most of the clumps do not have a circular shape, therefore an equivalent value for the radius is calculated from the area covered by the clump in ^{12}CO maps. We define the effective radius for each clump based on the area of the clump as $R_e = \sqrt{Area/\pi}$. The corrected antenna temperatures for ^{12}CO(2-1) and ^{13}CO(2-1) , $^{12}T_a^*$ and $^{13}T_a^*$ and the peak velocities for each emission line, V_{12} and V_{13}, are directly measured from spectra after baseline subtraction, and are listed in Table 3.6.

We calculate the ^{13}CO(2-1) optical depth and hydrogen column density assuming local thermodynamic equilibrium (LTE) conditions. We use the ^{12}CO(2-1) peak antenna temperature to calculate the brightness temperature and estimate the excitation temperature, T_{ex}, for each clump. The optical

depth, τ, and ^{13}CO column density can be derived by comparing the ^{12}CO(2-1) and ^{13}CO(2-1) brightness temperatures. We convert the ^{13}CO column density to hydrogen column density, $N(H)$, assuming an abundance factor of $\simeq 10^6$ (Pineda et al. 2008). Derived parameters are listed in Table 3.3. Column two shows the excitation temperature. In columns three and four we present the FWHM of the best Gaussian fitted to the ^{12}CO and ^{13}CO spectra. Column five presents the hydrogen column density calculated from LTE assumption. Calculated optical depth for ^{12}CO and ^{13}CO are listed in columns eight and nine. Detailed discussion of the methods and the equations are given in Paper I.

We used three different methods to estimate the clump masses. The Virial mass was calculated by assuming that our clumps are in Virial equilibrium. We used the ^{13}CO line widths and assumed a spherical distribution with density proportional to r^{-2} (McLaren 1988). In Paper I, we discussed the uncertainties of this mass estimation method. For example, the line profiles are broadened in many cases (for example strongly in S152 and S175B) due to internal dynamics and probably turbulence. As a result, the Virial equilibrium assumption overestimates the mass of the clumps and especially is not an appropriate mass estimation method for dynamically active regions.

We also calculated ^{13}CO column density under the LTE assumption and converted it to hydrogen column density in order to determine clump masses. There are some uncertainties in the mass estimated this way from several fac-

tors due to non-LTE effects. For example, in the LTE assumption the CO column density directly varies with T_{ex}. However the ^{12}CO emission might be thermalized even at small densities, while the less abundant isotopes may be sub-thermally excited (Rohlf & Wilson 2004). LTE calculations assume that the excitation temperature is constant throughout the cloud. T_{ex} is calculated from the observed ^{12}CO line which is optically thick and only traces the envelope around the dense cores; however, inside the envelope, the core might be hotter or cooler. If the core is hotter than the envelope, the emission line might be self absorbed and the measured antenna temperature will give too small a T_{ex} for most of the clumps. The M_{LTE} is the smallest calculated mass for most of the clumps in our sample.

In the case of the optically thick ^{12}CO emission we can calculate the column density from the empirical relation $N(H_2) = X \times \int T_{mb}(^{12}CO)dv$, with the brightness temperature, $T_{mb} = T_a^*/\eta_{mb}$. For the JCMT, $\eta_{mb} = 0.69$ is the beam efficiency at the observed frequency range. However the "X-factor" is sensitive to variations in physical parameters, such as density, cosmic ionization rate, cloud age, metallicity and turbulence. The "X-factor" also depends on the cloud structure and varies from region to region. Studies (e.g. Pineda 2008, and references therein) have shown that the X value is roughly constant for the observed Galactic molecular clouds, and is currently estimated at $X \simeq 1.9 \pm 0.2 \times 10^{20}$ cm^{-2}(K km s^{-1})$^{-1}$ (Strong & Mattox 1996). Detailed calculations on columnd density and mass can be found in Paper I. The velocity integrated

mass M_{int} calculated for all the identified clumps and relevant volume density are listed in columns six and seven of Table 3.3. In general M_{int} is intermediate between M_{vir} which often overestimates the mass determinations and M_{LTE} which may underestimates the mass. Accordingly, we use M_{int} as the best mass estimation for our clumps in the rest of this paper and discuss the estimated masses relations further in §3.5.4.

3.5 Discussion

In this section we discuss the physical conditions of 142 clumps identified within clouds associated with ten H II regions. We investigate the relationships between different measured and calculated parameters such as size, line widths, density and mass in order to understand how they have been affected in different regions. We also explore how these physical properties vary with distance from the ionized fronts of the H II region. Since derived physical parameters vary over a large range, we made logarithmic plots to examine the large dynamical range of variations.

3.5.1 Size-Line Width (Larson) Relationship

Studies of the molecular emission profile and line width provides us with information of the internal dynamics and turbulence of the clumps and cores.

Various studies of molecular cloud clump/cores have examined the relation between line width and clump/core size (e.g., Larson 1981, Solomon et al. 1987, Lada et al. 1991 , Caselli & Myers 1995, Simon et al. 2001) and a power law, often known as the Larson relation, has been proposed to describe this relationship:

$$\Delta V \propto r^{\alpha}, \qquad 0.15 < \alpha < 0.7. \tag{3.1}$$

This relation has been observed over a large range of clumps/cores, from smaller than 0.1 pc up to larger than 100 pc. Different power law indices have been observed within different samples. The observed relationship is presumingly affected by the cloud physical conditions, clump definition, and dynamical interaction with associated sources such as H II regions, newborn stars or proto-stars. In their survey for dense cores in L1630 Lada et al. (1991) noticed that the existence of the Larson relation is highly dependent on clump definition. They found a weak correlation for clumps selected by 5σ detection above the background but no correlation for clumps selected at 3σ. Kim & Koo (2003) found a good correlation between size and line width for both ^{13}CO and CS observations with $\alpha = 0.35$. However, some other studies show more scattered plots (e.g. Yamamoto et al. 2006, Simon et al. 2001) or no relation at all (e.g Azimlu et al. 2009, Plume at al. 1997). In a study of three categories of clumps containing massive stars, containing stellar or proto-stellar identified sources, and no identified source, a weak relation was found (Saito at al. 2008). In this

study the clumps that contain massive stars had larger ΔVs.

In a study of cloud cores associated with water masers, Plume et al. (1997) noted that the size-line width relation breaks down in their massive high density cores which systematically have higher line widths. Line widths larger than those expected from thermal motions are thought to be due to local turbulence (Zuckerman & Evans, 1974). Larson (1981) noted that regions of massive star formation such as Orion seem to have larger ΔV and probably show no correlation with size. Plume et. al. (1997) concluded that a lack of the Larson relation in their data indicates that physical conditions in very dense cores with massive star formation are very different from local regions of less massive star formation (the line widths may have been affected by star formation process). They suggested that these conditions (denser and more turbulent than usually assumed) may need to be considered in studying the massive portion of the Initial Mass Function. This argument agrees with the conclusions of Saito et al. (2007). In their study (Saito et al. 2007), note that most of the clumps without massive stars, the cluster forming clumps classified by a previous study (Tachihara et al. 2002) and the massive clumps observed by Casseli & Myers (1995) al have a similar line width. These regions have in common that they are all forming intermediate mass stars, suggesting that there is a close relation between the characteristics of the formed stars and the line width. They also mention that, although the line width might be influenced by feedback of young stars, an extended line emission could be a part of the initial conditions of the

cloud.

The index α seems to depend on the physical conditions of the cloud and especially varies in turbulent regions (e.g Caselli & Myers 1995; Saito et al. 2006). Star forming regions are turbulent environments and the star formation process is believed to be governed by supersonic turbulence (e.g. Padoan & Nordlund 1999) driven on large scales. A turbulent cascade then transfers the energy to smaller scales and forms a hierarchical clumpy structure (Larson 1981). Numeric analysis of decaying turbulence in an environment with a small Mach number (the speed of moving object in a fluid divided by the speed of sound) is consistent with the Kolmogorov law, but a supersonic magneto hydrodynamic turbulence results in a steeper velocity spectrum (Boldyrev 2002 and references there in).

We investigated the Larson relation in our sample for both ^{12}CO(2-1) and ^{13}CO(2-1) lines. Size and line width are two parameters which are directly measured from the observations. First we studied ΔV_{12} versus R_e for the clumps in each region individually. Because there are uncertainties in both ΔV and R_e, we calculated the slope of the fitted line with five different fitting methods using the *slope* code by Isobe et al. (1990). We are looking for a possible relation between two parameters and so we accepted the bisector least-squares fit as the best fitting method in our study for all parameters as recommended by the authors.

Different values were found for α varying between -1.6$\pm$0.4 and 3.0$\pm$0.5.

We found four objects with $\alpha \leq 0.06$ with poor correlation coefficients (-0.36 - 0.002) and 6 objects with $\alpha \geq 1.3$ with higher correlation coefficients (0.45 for S307 to 0.8 for S305). The slopes and uncertainties for both ΔV_{12} and ΔV_{13} are listed in Table 3.4.

There is a noticeable gap between these two α ranges and we therefore divided our sources into two categories: the "type I" sources that show a size-line width relation and "type II" sources with poor correlation, small values for α and therefore weak or no Larson relation. The clumps within type II sources have broader lines in general and have a scattered size-line width plot. Figure 3.2 shows ΔV plotted versus R_e for these sources. No size-line width relation is found. Figure 3.1 shows the plots of ΔV_{12} and ΔV_{13} vs R_e and the derived αs for both ^{12}CO(2-1) (black dots) and ^{13}CO(2-1) (red dots) lines. S288 has only 4 identified clumps and therefore and we therefore excluded this region. ^{13}CO has smaller line widths compared to ^{12}CO but very similar relations for both type I and type II sources.

The slopes we have calculated for type I regions are larger than the reported values. The calculated values are partially dependent on the fitting method which must be considered to compare different surveys. For example some of fitting commands in plotting packages such as Super Mongo only calculate ordinary least square based on "X" which is always smaller than the bisector line fit. Our "X" least square slopes for type I sources vary between 2.1 and 0.7 for ^{12}CO and 1.4 and 0.7 for ^{12}CO line widths. On the other hand larger line

widths and larger slopes might be a result of the gas properties in massive star forming regions. Most of the previous works study the size-line width relation in low mass and intermediate star forming regions. Larger line widths and consequently larger power indices might be a cause by the massive star and the H II region or the initial conditions of the molecular clouds that produce massive stars. We discuss that issue n more details in section 3.5.6.

Considering all six type I sources together, we derived $\alpha = 0.76 \pm 0.05$ for ΔV_{12} vs. R_e and $\alpha = 0.71 \pm 0.05$ for ΔV_{13} vs R_e with correlation coefficients of 0.7 and 0.62 respectively. These results are in agreement with the largest reported slopes.

The type II sources have larger line widths in ^{13}CO as well (Figure 3.2). Such large line widths may originate from the initial conditions of the clump or maybe caused by energy inputs such as proto-stellar outflows, radiation pressure from massive stars, strong stellar winds, internal rotation and infall to proto-stars within the clumps.

We have detected strong signatures of an outflow within S175B (Azimlu, et al., in preparation) which has the largest line widths in our sample. S152 is the other source in our sample with large line widths. This region has very active star formation and contains a dense stellar cluster (detected in 2MASS data). To provide enough gravitational energy to bind the clumps with larger internal velocity dispersion, much higher densities are required than for the clumps with smaller line widths (Saito et al., 2006). High gas density ($n > 10^5$ cm^{-3})

is an essential factor in the formation of rich embedded clusters such as the one detected in S152 (Lada et al. 1997). In addition, these clumps must be gravitationally bound in order to survive longer than the star formation time scale of $\sim 10^6$ yr. In a massive star-forming model, McKee & Tan (2003) suggest that the mass accretion rate in a core embedded in a dense clump depends on the turbulent motion of the core and the surface density of the clump. Therefore, to form a dense core that can produce a massive star, the clump requires both a high gas density and large internal motion while it is also gravitationally bound. External pressure may have an important role on providing additional force to keep the clump stable during the star formation process (Bonnor-Ebert model; Bonner 1956, Ebert 1955).

3.5.2 Size-Density Relation

We investigated the relation between column density and size for type I and type II sources. In Figure 3.3 we plot N(H) versus clump effective radius for both type I (top panel) and type II (bottom panel) sources. We found no relation between the column density and size for our sources. We also investigated the relation between velocity integrated volume density and size. Results are presented in Figures 3.4 and 3.5. There is a weak relation for some individual sources such as S175A and S175B but, in total, the density decreases as size increases. The dashed line with a slope of -2.5 shows the limit below which we have not found any clump. Simon et al. (2001) found different power

law indices for their sample of four molecular cloud complexes varying between -0.73 and -0.88, slightly smaller than the power law factor of -1.24 found by Kim & Koo for molecular clouds associated with ultra compact H II regions. These results may be due to the fact that the smaller clumps are probably more evolved. The gas is more collapsed to the centre and therefore these clumps have smaller size with larger volume densities. This also explains the lack of a relation between size and column density. The smaller clumps have higher volume density and integrating density through the clump centre may result in a small or large column density dependent on the initial conditions and the nature of the clumps. Sources within our sample are located at different distances. We have detected the smallest clumps in S175A which is the closest source to us at a distance of ≈ 1 kpc. If this source was at a five times larger distance (approximately the distance of S305), clumps C1-C4 and C11-C13 could not be resolved and we measured smaller average volume density for these groups of clumps as individual objects. Thus, our plot is likely to be affected by the spatial resolution effect.

Saito et al. (2006) suggest that the mass and density must be larger for turbulent clumps (they define a core turbulent if $\Delta V > 1.2\,\mathrm{km\,s^{-1}}$) compared to non-turbulent ones for a given size to bind the turbulent clumps gravitationally. For a similar density distribution, they found that turbulent clumps (those with larger line widths) have densities twice the non-turbulent ones. We do not see an excess for mass or column density in our type II sources. For a detailed

discussion on different masses and equilibrium conditions of the clumps see §3.5.4.

3.5.3 LTE Mass and Column Density-Line Width Relation

We find a weak relation between N(H) and ΔVs (Figure 3.6 and 3.7). The column density increases with ΔV for both ^{12}CO and ^{13}CO lines. The dashed lines present the bisector least-squares fits with slopes of 2.3±0.25 and 2.1±0.35 for ^{12}CO lines in type I and type II sources respectively but the correlation coefficient is poor (0.53 and 0.42 respectively). The slopes are similar (2.3±0.23 and 2.4±0.38) for ΔV_{13} for both type I and type II sources with similar correlations (0.51 and 0.47 respectively).

M_{vir} and M_{int} both depend on the emission line profile and are expected to increase for type II regions with larger line widths. The LTE mass is calculated independent of the cloud dynamics and the emission line profiles. In Figures 3.8 and 3.9 we show how M_{LTE} varies with ΔV for both ^{12}CO and ^{13}CO emission lines. For type I sources M_{LTE} increases with ΔV for both ^{12}CO and ^{13}CO with least-square fit slopes of 4.2 ± 0.28 and 4.2 ± 0.24, but no relation is found for type II sources. The mass range is not very different for type I and type II clumps (1.1 - 350 vs 0.5 - 500 $M_\odot$). The LTE mass is calculated by integrating the LTE column density over the area of each clump assuming that it is a

sphere with radius of R_e. M_{LTE} is proportional to R_e^2; therefore, the fact that the mass calculation depends on size might be the cause of the relation between M_{LTE} and ΔV in type I sources where the size-line width relation was found.

3.5.4 Equilibrium State of the Clumps

Virial mass is calculated as $M_{vir}(M_\odot) = 126 \times R_e(\mathrm{pc})\ (\Delta V)^2(\mathrm{km\ s^{-1}})$ assuming that the gravitational potential energy is in balance with internal kinetic energy. M_{vir} increases with $(\Delta V)^2$; integrated mass, M_{int} is also line-profile dependent and varies linearly with ΔV, while M_{LTE} is independent of line width and of the internal dynamics of the cloud. We plot M_{vir}/M_{LTE} versus M_{LTE} in Figure 3.10 to investigate the virial equilibrium. Resolving the clumps within clouds is highly dependent on the distance to the cloud. To decrease the effect of resolution we have selected only objects at distances between 3 and 7 kpc. Closer sources are presented by crosses in the plot . Most of our clumps have larger Virial masses and are far above the $M_{vir} = M_{LTE}$ line, indicating that most of our clumps are probably not gravitationally stable. An external pressure is required to keep the clumps with $M_{vir} > M_{LTE}$ bound.

It has been suggested that to bind the turbulent clumps they must have larger masses and for similar size, the turbulent sources have possibly larger densities (Saito et al. 2007). In our sample both type I and type II sources have similar clump masses and we do not see an excess for either type, but we do see the effect of mass. In Figure 3.10 more massive clumps tend to be closer

to Virial equilibrium. The same pattern has been observed by Yamamoto et al. (2003, 2006) for clumps within two different regions where only larger clumps have Virial masses similar to the LTE mass.

Figure 3.11 shows the plot of velocity integrated mass, M_{int}, versus M_{LTE}. For most of the clumps, M_{int} is higher than the M_{LTE} but mostly below the line of the $M_{int} = 10M_{LTE}$. M_{int}/M_{vir} is much larger for low mass clumps and like M_{vir}, M_{int} tends to be equal to M_{LTE} for higher masses; however, the difference is smaller compared to M_{vir}, versus M_{LTE}. The solid line shows the best least-squares fit with a slope of 0.81.

In Figure 3.12 we compare M_{vir} versus M_{int}. Similar to M_{LTE}, clumps have larger M_{vir} for low mass clumps. At approximately M= 100 $M_{\odot}$, $M_{vir} \simeq M_{int}$, while for clumps larger than 100 $M_{\odot}$ $M_{vir} < M_{int}$. The solid line shows the least-squares fit with a slope of 0.59. The higher mass clumps in our plot lie within more distant sources where we cannot resolve smaller structures within them. It suggests that probably the average density and temperature of larger clumps results in a larger Jeans length while smaller dense structures resolved as clumps have locally higher density and therefore smaller Jeans length. Analysis of cloud and clump equilibria in a study of four molecular clouds at different distances shows that, while the whole cloud is gravitationally bound, the majority of the clumps within them are not (Simon et al 2001). We found that the equilibrium appears for clumps larger than $\sim 100M_{\odot}$.

3.5.5 Temperature-Line Width Relation

In Figures 3.13 and 3.14 we investigate the relation between the excitation temperature and line widths. Part of profile line broadening is due to the thermal velocity dispersion of the molecules and the thermal line width increases with temperature. The observed ΔVs are more broadened due to internal dynamics and turbulence within the clouds. We found no relation between T_{ex} and ΔV for both ^{12}CO and ^{13}CO emission lines which indicates that the emission line profile is dominated by the internal dynamics of the clumps.

3.5.6 Effects of Distance from H II Region on Physical Parameters

We are studying how H II regions and their exciting stars affect the physical conditions of their associated clouds. One might expect more influence on clumps that are closer to the H II region. To investigate these effects, we examine how the environmental parameters vary with distance from the edges of the ionized gas. Most of the H II regions in our sample are not perfect spheres but we try to fit the best circle on visible edges of the ionized gas. To determine the borders of the ionized gas we use Digital Sky Survey images in the red filter in which the hydrogen ionized gas is bright with sharp edges. Our sources have different angular sizes, different physical sizes and lie at different distances from the Earth. They might also be at different evolutionary stages,

with a mixture of ages. We need to re-scale the distances to a common distance to be able to compare them. A normalized distance for each clump is defined as the distance of the clump from the edge of H II region divided by the H II region radius.

Temperature-Distance relation

In Figure 3.15 we investigate the variation of excitation temperature, T_{ex} with distance from the H II region. We expect clumps to be warmed up by the radiation from the exciting star and to show a trend of decreasing temperature with distance from the H II region. We can see that the clump temperature decreases by distance from the ionized gas around some sources such as S175A and S152. We observe a scattered relation for S305 and a weak relation (for clumps at distances larger than 0.1R) for S104. The fact that we cannot see the same relation for other sources might be due to internal heating sources within the clumps such as proto-stars. C4 and C8 in S307 (noted in Figure 3.15, top panel) are good examples of such compact clumps with high density and temperature. On the other hand, we are measuring the projected distance of the clumps which in general will be smaller than the true value. We check the effect of distance projection by simulating numerically randomly distributed clumps with heating from an external source. The luminosity of the heating source, the power-law index of decrease in central heating with distance, and the heating of the clump from the diffuse background are the input parameters of

the simulation. We also set the number of clumps and the radial distribution of the clumps' positions. The output is temperature versus the projected distance from the heating source.

Figure 3.16 shows plots of some selected simulations. Assuming the input values are similar to observed parameters of our sample and assuming a $R^{-\alpha}$ decreasing power law for luminosity, (Figure 3.16) we see some scattering on the plot for small distances, but a decrease in temperature as distance from the heating source increases. We cannot have any distant hot clump that is warmed by the heating source. Such distant but hot clumps like S307-C3 and S307-C4 noted in Figure 3.15 are probably being warmed by an internal source such as a proto-star. We see more scatter in the simulated plots for smaller projected distances. Most of our mapped regions $7' \times 7'$ are small compared to the size of the H II region; consequently we did not map the molecular gas at large distance from the edges of H II regions with larger angular size (e.g. S104, S212 and S148/S149). The scattering of T_{ex} versus normalized distance for the clumps within these sources matches with the objects at the smaller distances of the simulated plots. S175B is the only source in which all of the clumps are too distant for it to have been influenced by the H II region.

Line Width-Distance Relation

We study the effect of the expanding ionized gas on the internal dynamics of the molecular gas by investigating the variation of line widths with distance

from the H II region. In Figure 3.17 we plot ΔV versus normalized distance for ^{12}CO (top panel) and ^{13}CO (bottom panel). We cannot find a relation for ΔV_{12} or ΔV_{13} versus distance for any of type I or type II sources. The line-width is very scattered at different distances even for S175A and S152 which show a decrease of T_{ex} with distance from the ionized gas. The expansion of the ionized gas may cause the molecular gas in shells around the H II region slightly larger line widths but we do not see a significant distance effect on the internal motions of the clumps mostly beyond the collected shells. Physical conditions of individual clumps and other internal sources of turbulence or dynamics such as proto-stellar outflows, infall and rotation may have a more important role on line profiles.

The noticeable point is that as we discussed in section 3.5.1, we have seen larger line widths and larger Larson power law indices in our sample for type I sources. But If the line profiles are not much affected by the H II region and the exciting star, then the observed large line widths are more probable to be a part of the initial characteristics of the cloud which already have formed at least one massive star.

3.5.7 Mass Distribution

The number of clumps identified within each mapped region varies between 4 and 35 with an average of about 12 clumps per region. because this number was not large enough to make an appropriate statistical study on mass distribution

for each mapped region, we investigated the characteristics of the largest clump, the second largest clump and the third largest clump in each mapped region. We expected to find the largest clumps within the collected shells of mass at the peripheries of the ionized gas. This was the case for some sources such as S192 and S175A, but not common for other objects. We did not find any relation between the largest clump mass and its normalized distance from the H II region.

We repeated the same procedure for the second and third largest clump within each region. We saw no relation for the second largest mass as well, but it was noticeable that the third largest clump has about 10% of the total mass of the cloud in most of our sources. Only S104 did not follow this rule. S104 has the largest angular size in our sample and we mapped only a small fraction of the molecular gas associated with this H II region. We extended the map from $7' \times 7'$ to $9' \times 9'$ to cover the edges of the ionized gas but may have still a significant amount of the emission from the more distant parts of the cloud. We only observed the fragmented clumps collected in layers around H II region. The number of clumps in this mapped region was twice that of the other sources and may explain why third largest clump in this region contains only 5% of the total mass of the observed part of the cloud.

3.6 Summary and Conclusions

We have studied the physical properties of molecular clouds associated with a sample of ten H II regions. We mapped eleven $7' \times 7'$ areas in ^{12}CO(2-1) at the peripheries of the ionized gas and extended one of these maps (around S104 H II region, the largest of our H II regions) to $9' \times 9'$ in order to understand the molecular gas well beyond the edges of the H II region. We studied the clumpy structure of the clouds and identified 142 distinct clumps within eleven mapped regions. We also made pointed observations in ^{13}CO(2-1) at the position of the brightest ^{12}CO peak within each clump for 117 clumps. We used these observations to measure and calculate the physical characteristics of the clouds. We summarize our findings below:

We investigated size-line width relation for our sources using both ^{12}CO and ^{13}CO emission lines and calculated effective radius. Our sources are divided into two categories: those which do not show any size-line width relation and those which show a power law relation. We labeled these group of sources as type I and the other four sources with no relation as type II. Type II sources have larger line widths in general.

The power law indices derived for size-line width relation in type I sources are relatively larger than the previous studies, but they are not affected by the exciting star or the ionized gas. We may conclude that larger line widths and consequently larger indices are possibly the initial conditions of the massive

star forming molecular clouds.

No relation was found between column density and size of the clump but, for both type I and type II sources, the volume density decreases with size; the larger clumps have smaller densities. The smaller clumps might be more evolved, contracting to smaller size and higher densities.

We investigated the relationship between LTE column density and line width. We found that the column density increases with both ΔV_{12} and ΔV_{13} for both type I and type II regions but the relation is very scattered and difficult to fit a line.

We estimated the mass of each clump in three different ways: the Virial mass using ΔV_{13} determined from optically thinner ^{13}CO lines ($M_{vir} \propto (\Delta V_{13})^2$), ^{12}CO velocity integrated mass or X factor mass ($M_{int} \propto \Delta V_{12}$), and LTE mass (mass estimate independent of line width) using both ^{12}CO and ^{13}CO lines. M_{vir} is larger than the M_{LTE} for small clumps but tends to equal values for large masses. Low mass clumps also have larger M_{vir} than M_{int} but M_{vir} become approximately equal to M_{int} at M=100 $M_\odot$ and is smaller than M_{int} for larger masses. We may conclude that the larger clouds are gravitationally bound but the fragmented smaller clumps within them are not.

We investigated how M_{LTE} varies with ΔV for both type II and type I sources. While we see that M_{LTE} increases with both ΔV_{12} and ΔV_{13} for type I sources, no relation was found for type II regions.

No relation was found between the excitation temperature and the line widths. This suggests that the line widths for both ^{12}CO and ^{13}CO are determined by the internal dynamics of the clump rather than the thermal velocity dispersion of the molecules.

Excitation temperature decreases with distance from the edges of the ionized gas for some clouds. However, the measured decrease is not significant because of the projected distance effect especially for smaller distances.

The effect of the H II regions on the internal dynamics of the clumps was investigated. The line widths for the clumps within collected shells around H II regions are slightly larger, but no relation was found between ΔV_{12} and ΔV_{13} and normalized distance from the H II region. The expansion of the ionized gas affects the internal dynamics of the collected mass but these effects do not go beyond the shells. The plots of ΔV versus normalized distance are very scattered for both type I and type II regions, even for those sources in which temperature decreases by distance.

The third most massive clump in each region contains 10% of the total mass of the observed part of the cloud in our sample. The only exception, S104, is the largest H II region in our sample and due to its large size we have mapped only a small fraction of its associated molecular cloud.

We have measured and calculated physical characteristics of molecular clouds associated with H II regions. High density turbulent clumps are good candidates for massive star formation. We have detected such clumps within type II

sources in our sample. Our sources lie at large distances and we cannot resolve individual embedded proto-stars within them, but we have detected signatures of star formation such as proto-stellar outflows within our sample.

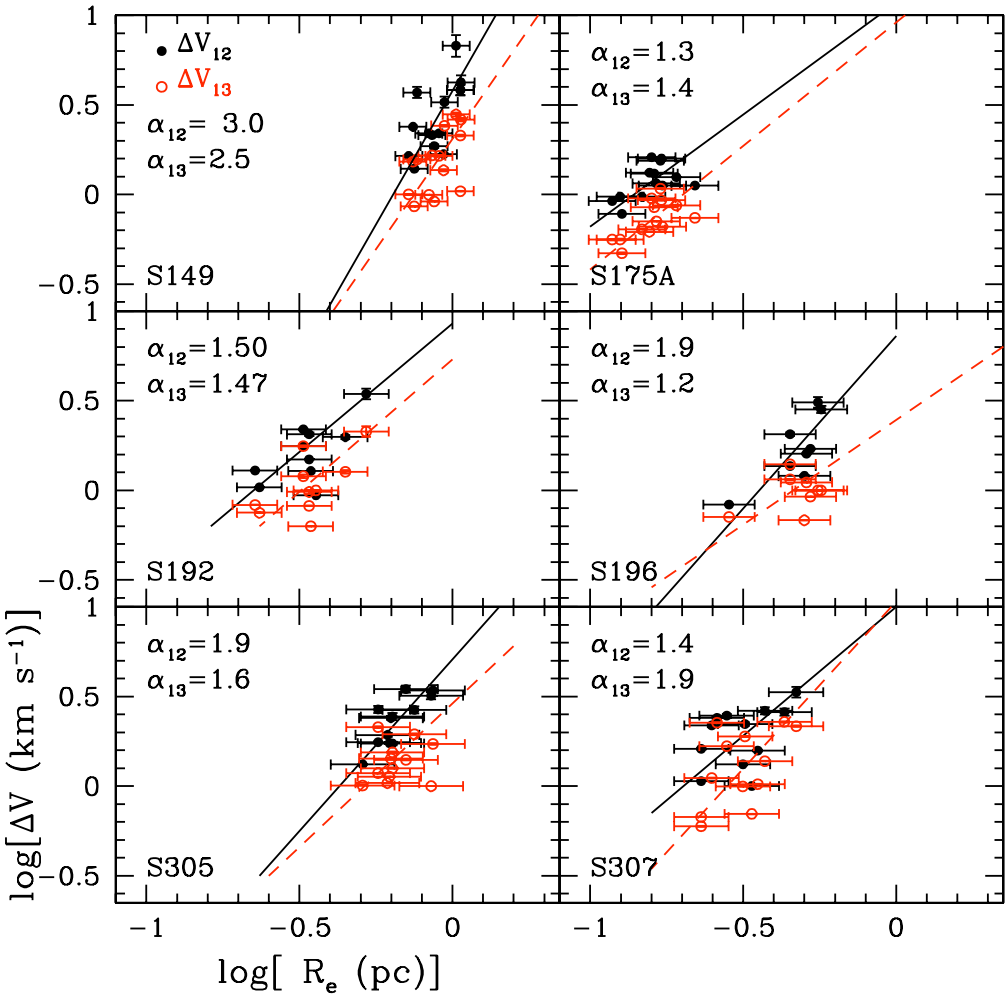

Figure 3.1 Correlation between the ^{12}CO(2-1) (black) and ^{13}CO(2-1) (red) line widths and the effective radius of the clumps for type I sources. The solid line is the bisector least-square fit for ^{12}CO(2-1) and dashed line shows the least-squares fit for ^{13}CO(2-1) lines. The slope derived for each line is shown in top left corner of each panel.

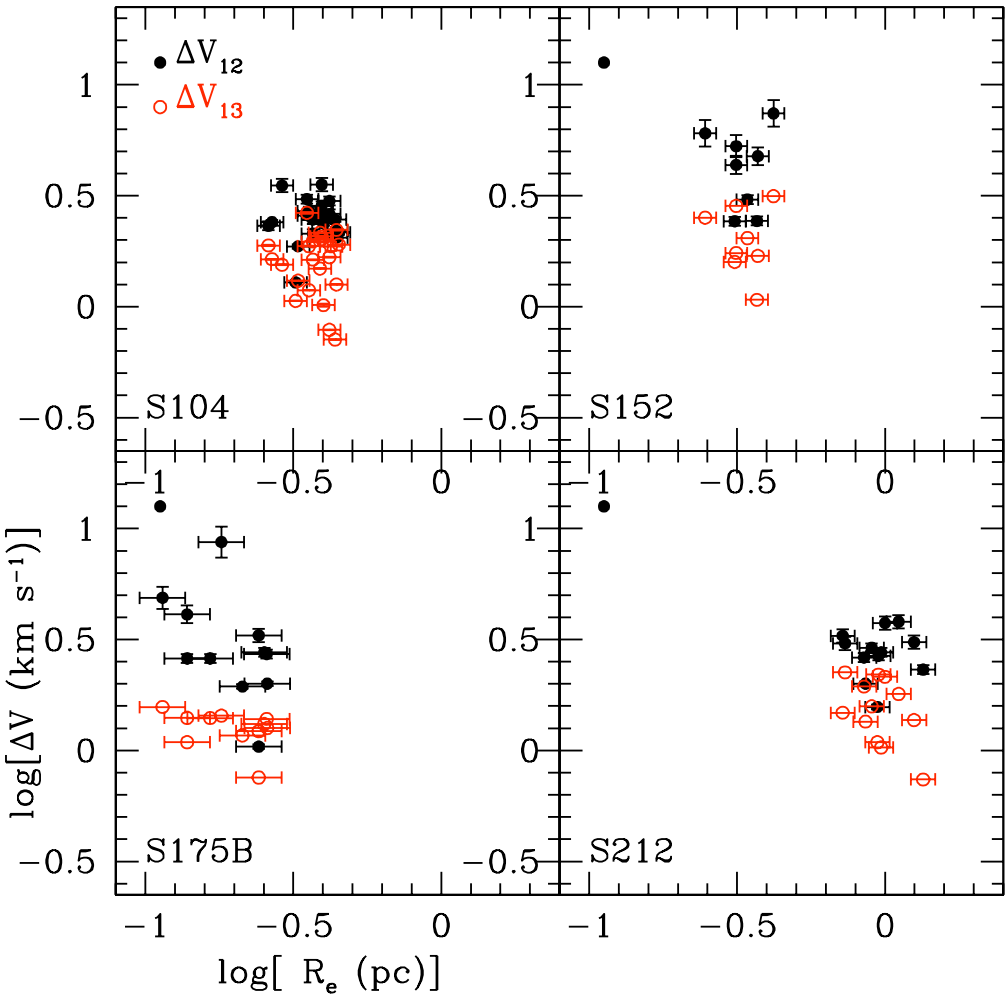

Figure 3.2 Same plot as Figure 3.1 for type II sources.

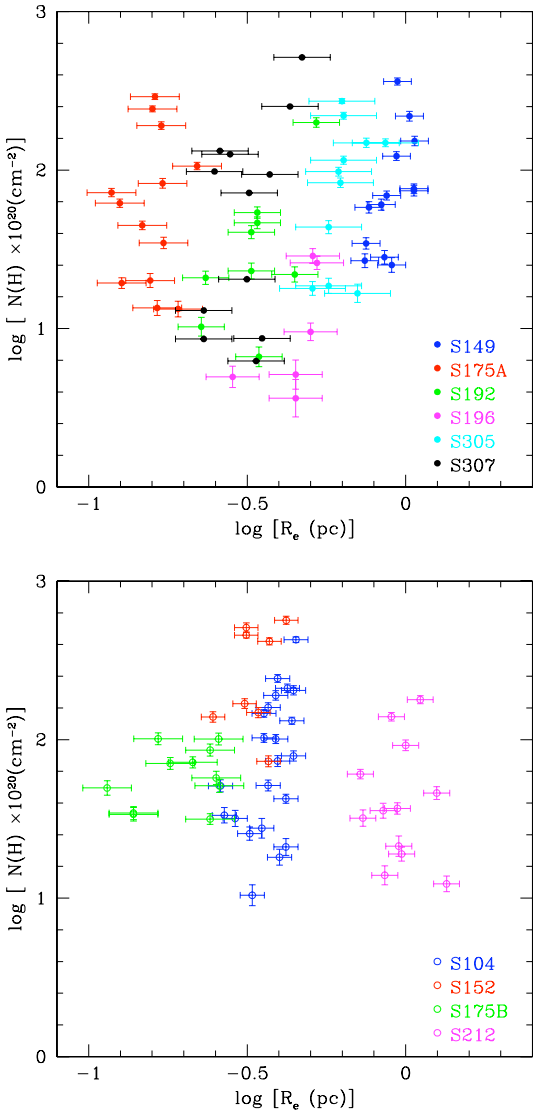

Figure 3.3 LTE column density vs. effective radius for type I (top) and type II (bottom) sources.

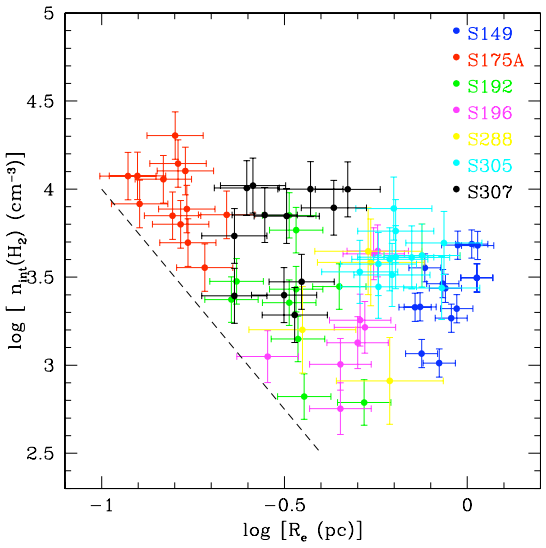

Figure 3.4 Velocity integrated volume density vs. effective radius for type I sources. The dashed line shows an approximate limit below which no clump has been found in our rdata ($n_{int} = -2.5R_e + 1.5$). No strong correlation is found between n_{int} and R_e but overall the volume density is smaller for larger clumps.

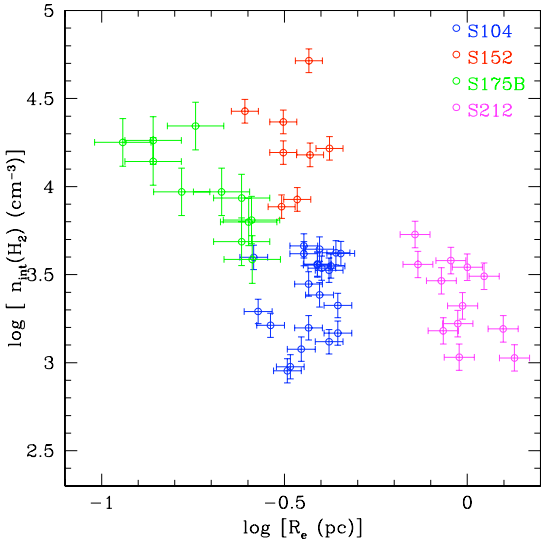

Figure 3.5 Same as Figure 3.4 for type II sources. Similar to type I sources, no strong correlation is found between n_{int} and R_e but overall the volume density tends to smaller values for larger clumps.

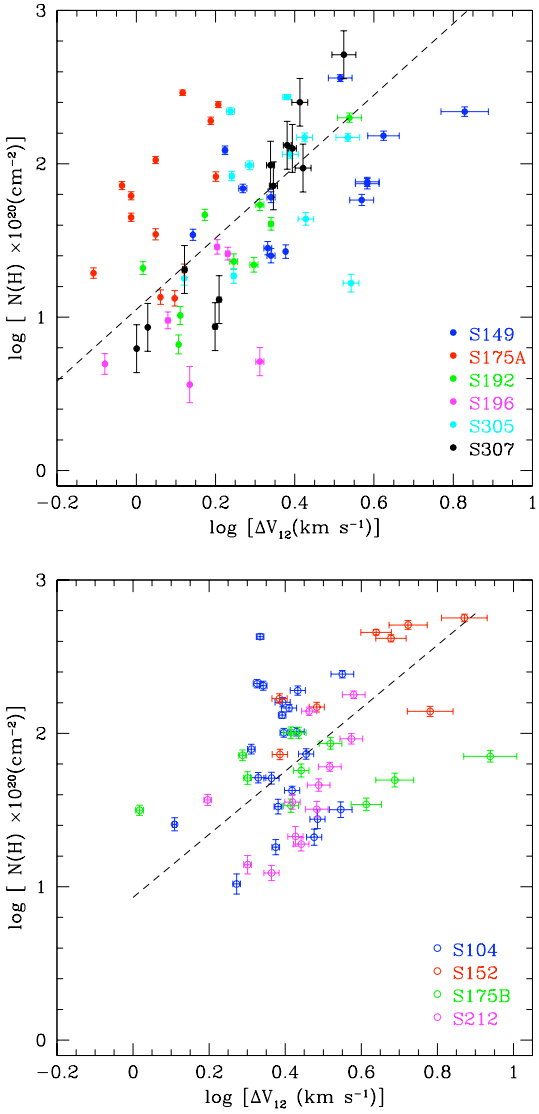

Figure 3.6 LTE column density vs. ΔV_{12} for type I (top) and type II (bottom) sources. The dashed line shows the bisector least-squares fits. The relation for type I sources has a slope of 2.3; the relation for type II sources is slightly weaker (correlation coefficient of 0.42 compared to 0.53 for type I sources) with a slope of 2.06.

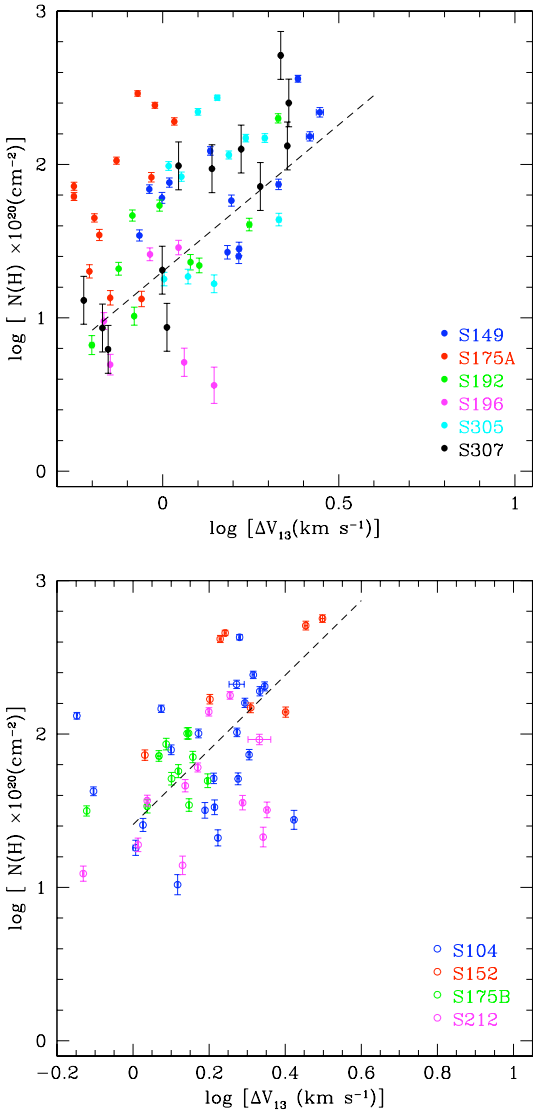

Figure 3.7 Same plot as Figure 3.6 for ^{13}CO(2-1) line widths. The relation for type I sources has the same slope of ^{12}CO(2-1) , 2.3; the relation for type II sources is slightly weaker (correlation coefficient of 0.43 compared to 0.53 for type I sources) with a slope of 2.43.

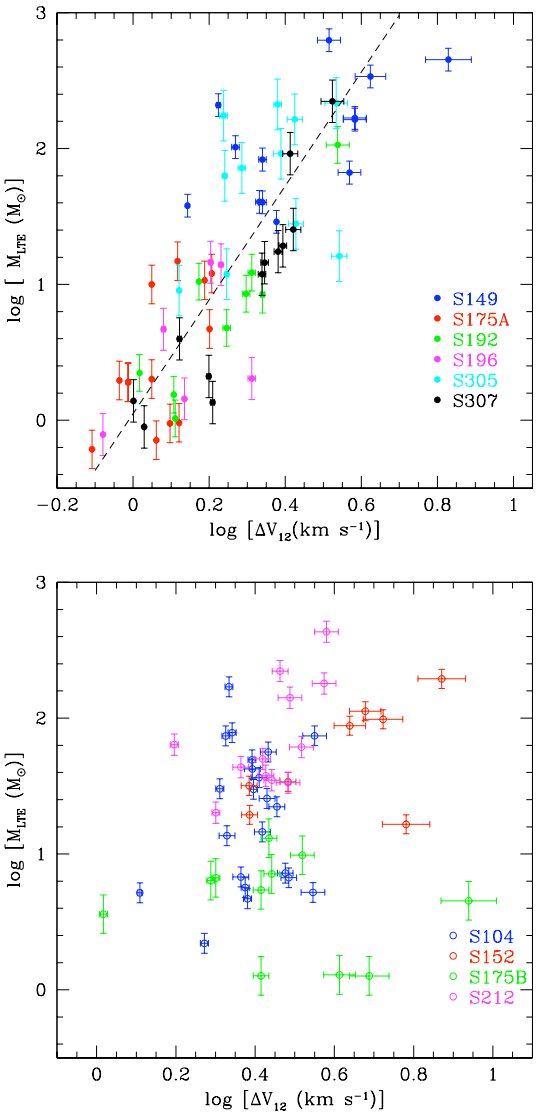

Figure 3.8 M_{LTE} vs. ΔV_{12} for type I (top) and type II (bottom) sources. The dashed line shows the bisector least-squares fit to type I clumps with a slope of 4.2. No relation is found for type II sources.

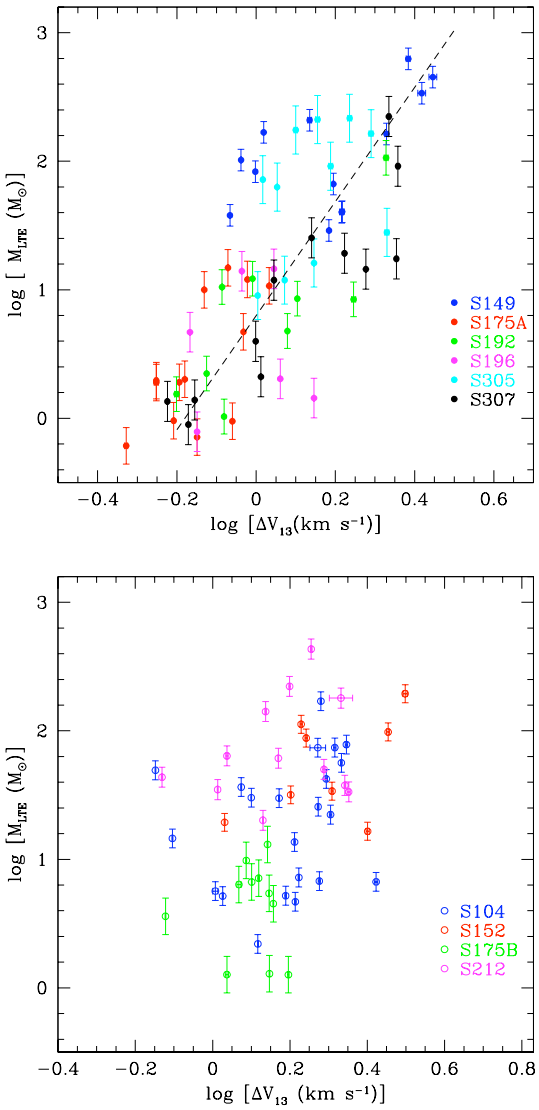

Figure 3.9 Similar to Figure 3.8 for ^{13}CO(2-1) line width. The dashed line is the least-squares fits with the slope of 4.2, the same as the previous plot. Similar to ^{12}CO(2-1) , no relation is found between M_{LTE} and ΔV_{13} for type II sources.

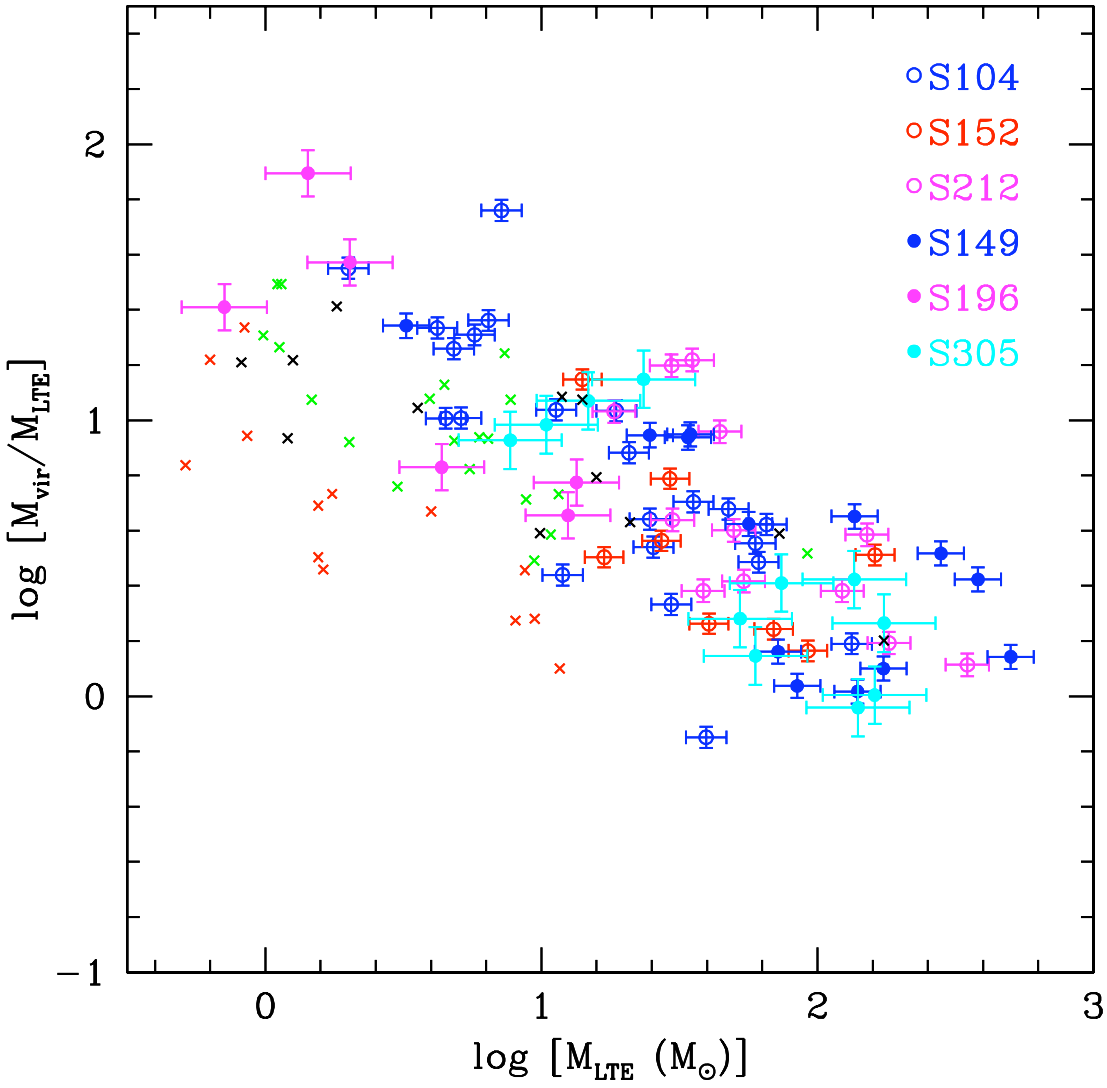

Figure 3.10 M_{vir}/M_{LTE} vs. M_{LTE}. Filled circles present type I sources and open circles present type II sources. To decrease the effect of varying distances and consequently the resolution effect we have considered only sources at nearer distances between 3.3 and 7.1 k pc. Other sources are shown by crosses.

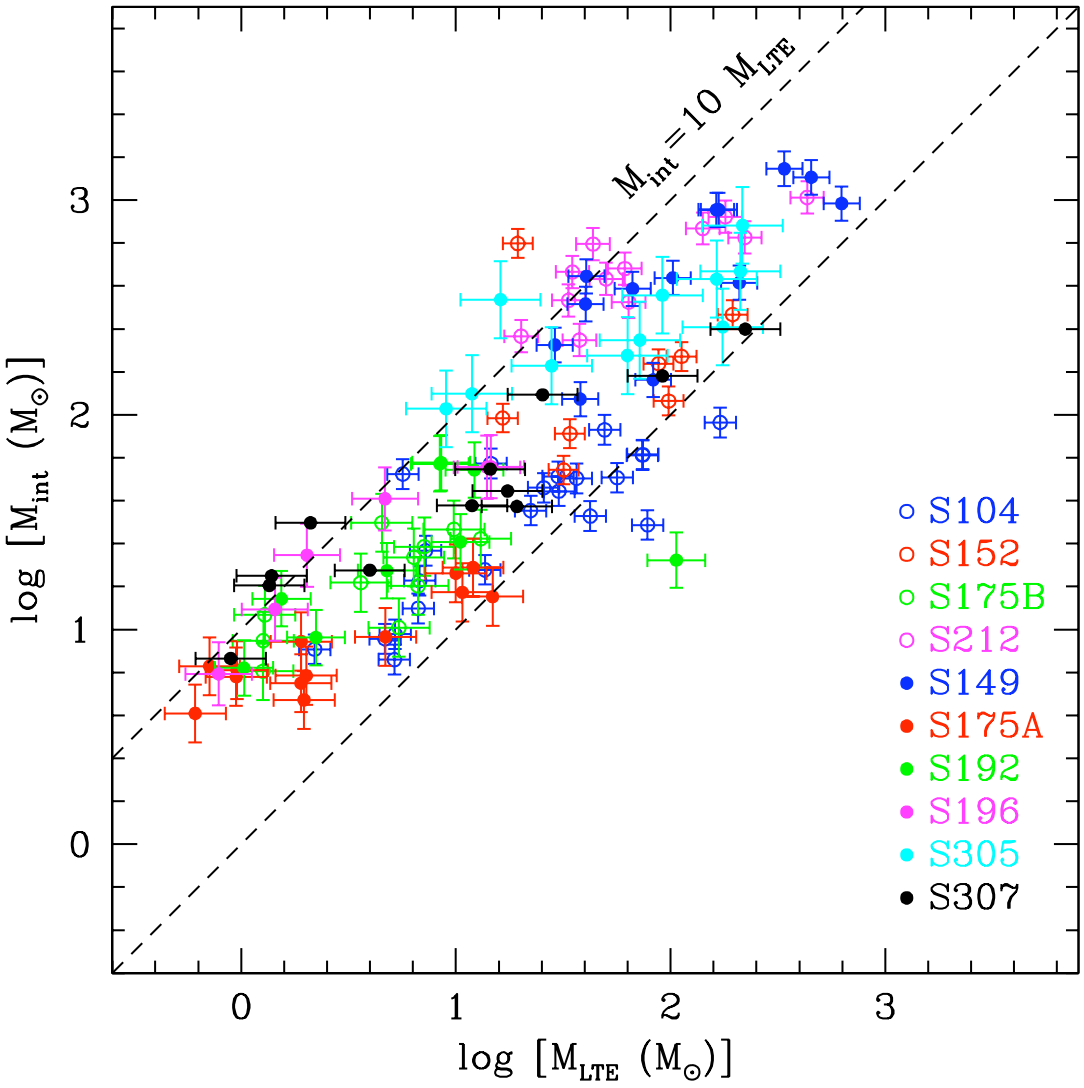

Figure 3.11 Velocity integrated mass plotted vs. LTE mass. Filled circles represent type I sources and open circles represent type II sources. The solid line is the least-squares fit to all clumps together. The dashed lines are $M_{int} = M_{LTE}$ and $M_{int} = 10 M_{LTE}$.

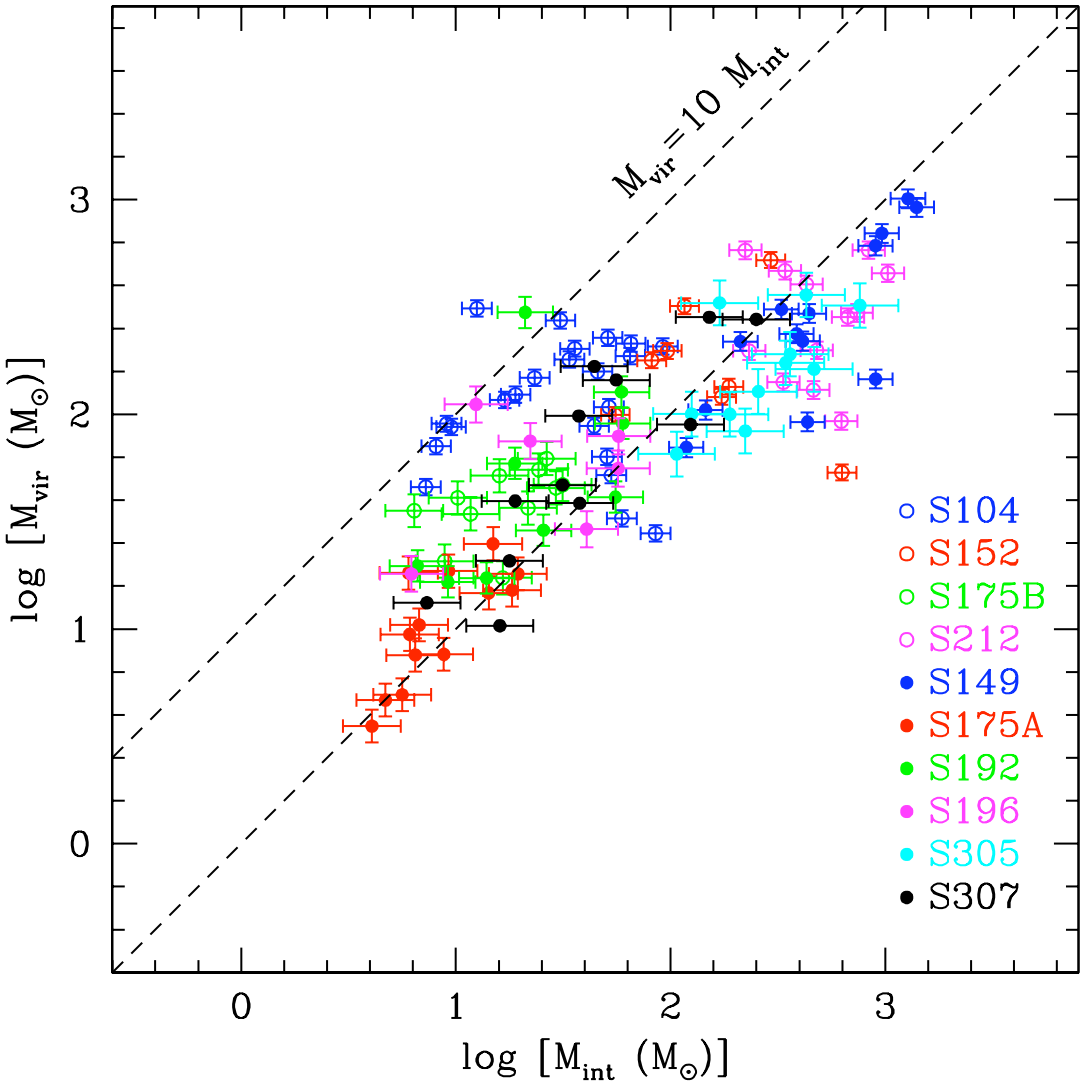

Figure 3.12 Virial mass plotted vs. velocity integrated mass. Filled circles represent type I sources and open circles represent type II sources. The solid line is the least-squares fit to all clumps together. The dashed lines are $M_{vir} = M_{int}$ and $M_{vir} = 10M_{int}$. Virial mass tends to equal to M_{int} for massive clumps and they are equal at M $\sim 100M_{\odot}$.

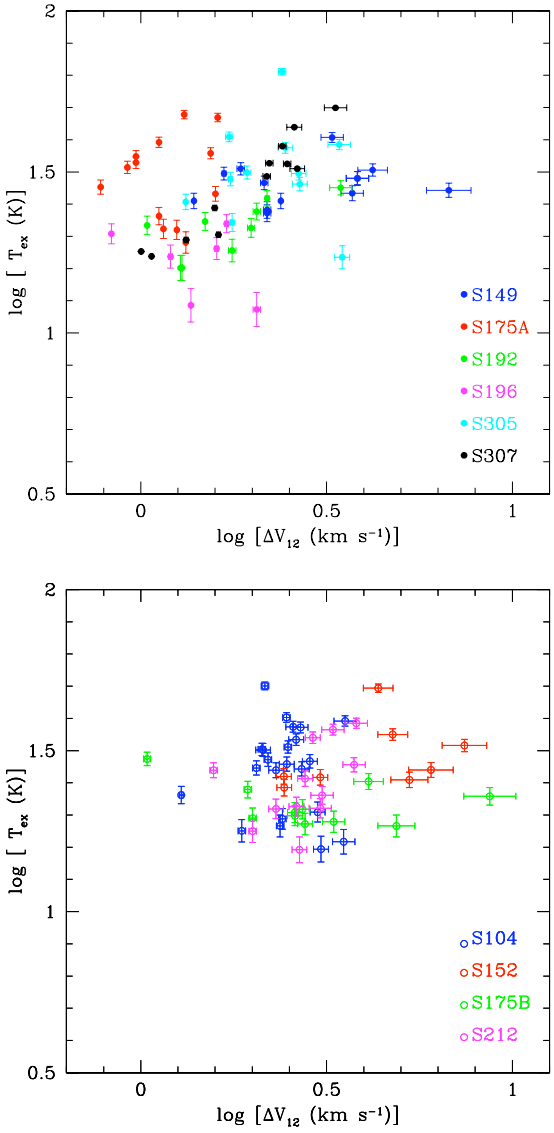

Figure 3.13 Excitation temperature vs. ΔV_{12} for type I (left panel) and type II (right panel) sources. No relation is found for type I or type II sources. Lack of relation may indicate that the line widths (which are generally much larger than the calculated thermal line widths) are dominated by the internal dynamics of the clump.

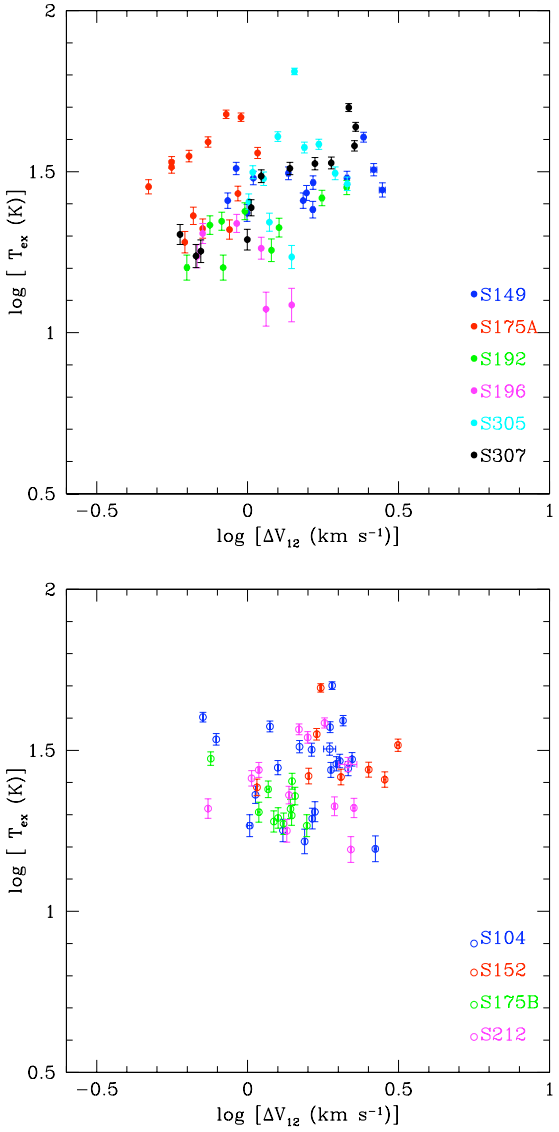

Figure 3.14 Same as Figure 3.13 for ΔV_{13}. Similarly no relation is found.

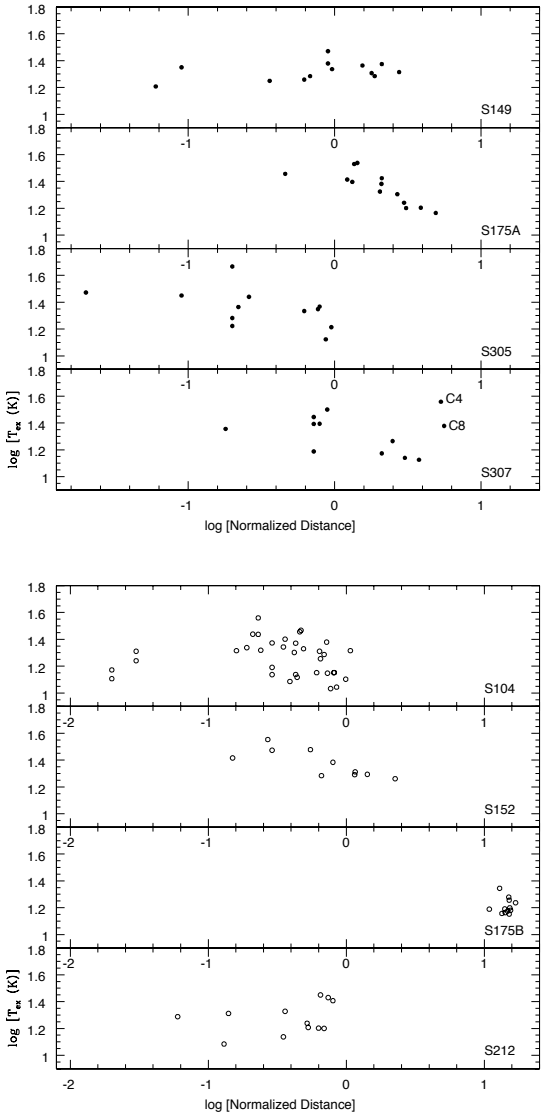

Figure 3.15 Excitation temperature vs. normalized distance from H II region for type I (left panel) and ^{13}CO(right panel) sources.

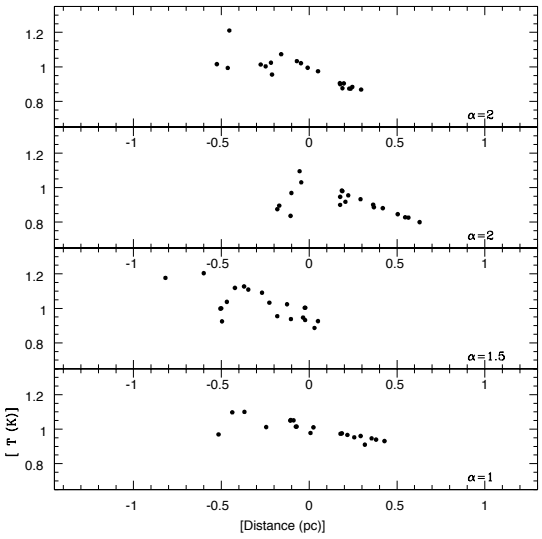

Figure 3.16 Simulated temperature variation from a heating source with similar physical conditions as our cloud samples with different luminosity decrease power law index, α.

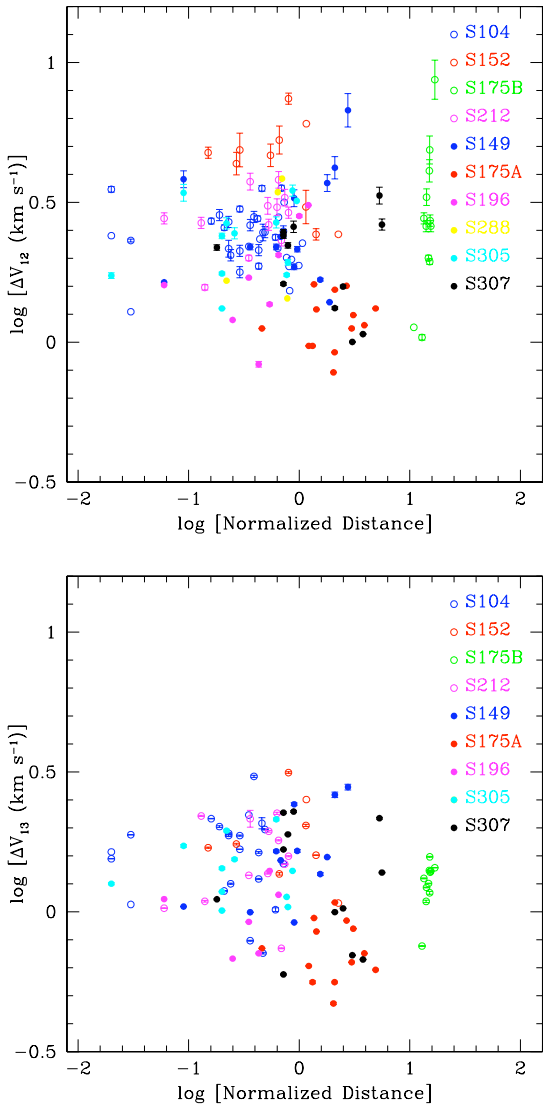

Figure 3.17 Line width vs. normalized distance from H II region for ΔV_{12} (top) and ΔV_{13} (bottom).

Table 3.1. Properties of selected regions

Source	RA J(2000)	Dec J(2000)	Distance (kpc)	V_{LSR} (kms^{-1})	Diameter (arcmin)	Diameter (pc)	Exciting Star
S104	20:17:42	36:45:30	3.3±0.3	0.0	7	6.7	O6V [a]
S148/S149	22:56:22	58:31:29	5.6±0.6	-53.1	1	1.6	B0V [a]
S152	22:58:41	58:47:06	2.39±0.21	-50.4	2	1.4	O9V [b]
S175A	0:27:04	64:43:35	1.09±0.21	-49.6	2	0.63	B1.5V [b]
S175B	0:26:25	64:52:36	1.09±0.21	-49.6	2	0.63	B1.5V [b]
S192/193	2:47:30	61:56:33	2.96±0.54	-46.3	1	0.86	B2.5V [b]
S196	2:51:41	62:12:19	4.7±1.0	-45.1	4	5.4	... [d]
S212	4:40:56	50:27:47	7.1±0.7	-35.3	5	10.3	O6 [a]
S288	7:8:39	-4:18:41	3.0±1.2	56.7	1	0.87	B1 [c]
S305	7:30:13	-18:31:50	5.2±1.4	44.1	4	6.1	O9.5 [c]
S307	7:35:33	-18:45:55	2.2±0.5	46.3	6	3.8	O9 [c]

[a]Data about exciting star and distance from Caplan et al. 2000

[b]Data about exciting star and distance from Russeil et al. 2007

[c]Data about exciting star and distance from Moffat et al. 1997

[d]No exciting star identified for this H II region. The kinematic distance is reported here. Note that S196 is close to S192/S193 in position and velocity and is likely to be at the same distance.

Table 3.2. Physical parameters measured for the entire sample

ID	RA	DEC	R_e (pc)	$^{12}T_b$ (K)	$^{13}T_b$ (K)	V_{12} (km s^{-1})	V_{13} (km s^{-1})
S104							
... C1	20:17:26.0	+36:42:34.0	0.40±0.04	13.3	3.2	0.81	0.58
... C2	20:17:34.4	+36:46:39.5	0.35±0.03	10.5	2.1	-2.85	-2.32
... C3	20:18:01.8	+36:45:10.1	0.38±0.03	20.5	···	-0.1	···
... C4	20:17:56.6	+36:45:23.8	0.45±0.04	44.7	18.6	0.61	-0.42
... C5	20:17:23.9	+36:45:56.8	0.28±0.03	12.6	···	1.83	···
... C6	20:17:50.7	+36:46:54.5	0.29±0.03	11.4	3.7	-1.42	-1.33
... C7	20:17:53.6	+36:48:18.7	0.42±0.04	28.8	6.7	1.42	-0.66
... C8	20:17:57.8	+36:44:34.9	0.44±0.04	34.7	17.1	0	0.66
... C9	20:17:30.3	+36:47:49.3	0.39±0.04	22.3	10.7	0.91	0.66
... C10	20:17:57.2	+36:43:52.8	0.40±0.04	33.6	12.3	0.81	0.87
... C11	20:17:57.7	+36:48:11.9	0.40±0.04	27.0	8.4	0.4	0.54
... C12	20:17:29.9	+36:42:55.2	0.42±0.04	26.5	12.5	1.62	1.25
... C13	20:17:35.1	+36:42:34.6	0.36±0.03	32.0	12.9	1.22	1.37
... C14	20:17:40.9	+36:42:20.9	0.36±0.03	31.9	6.6	2.23	1.53
... C15	20:17:27.4	+36:47:21.1	0.44±0.04	22.6	8.2	1.62	1.7
... C16	20:17:30.3	+36:48:45.3	0.37±0.03	23.3	10.0	1.01	1.16
... C17	20:17:54.9	+36:43:17.7	0.37±0.03	26.4	4.3	1.32	1.45
... C18	20:17:36.1	+36:47:07.6	0.42±0.04	15.1	2.3	3.66	3.49
... C19	20:17:45.0	+36:42:35.2	0.4±0.04	23.9	5.1	4.98	4.9
... C20	20:17:46.7	+36:44:48.3	0.33±0.3	12.7	1.6	5.48	5.27
... C21	20:17:42.6	+36:42:56.0	0.26±0.02	22.1	4.1	5.99	6.52
... C22	20:17:42.1	+36:41:53.0	0.31±0.03	21.5	···	2.13	···
... C23	20:17:51.3	+36:44:13.5	0.27±0.02	14.2	3.6	6.09	5.85
... C24	20:17:52.4	+36:45:02.6	0.32±0.03	17.7	3.9	5.89	6.02
... C25	20:17:50.1	+36:48:32.5	0.44±0.04	24.3	10.9	6.4	0.87

Table 3.2—Continued

ID	RA	DEC	R_e (pc)	$^{12}T_b$ (K)	$^{13}T_b$ (K)	V_{12} (km s^{-1})	V_{13} (km s^{-1})
... C26	20:15:48.8	+36:31:52.9	0.35±0.03	22.1	···	2.34	···
... C27	20:15:29.9	+36:35:31.2	0.32±0.03	11.8	···	2.34	···
... C28	20:15:52.8	+36:40:26.0	0.55±0.05	13.1	···	0.2	···
... C29	20:15:42.4	+36:41:00.1	0.32±0.03	13.3	···	0.92	···
... C30	20:15:38.9	+36:40:24.2	0.6±0.05	13.2	···	0.61	···
... C31	20:15:48.1	+36:40:40.7	0.52±0.05	8.7	···	2.54	···
... C32	20:16:09.7	+36:39:02.6	0.39±0.04	22.4	···	0.51	···
... C33	20:17:54.3	+36:41:40.4	0.38±0.03	9.0	···	0.61	···
... C34	20:17:58.2	+36:41:54.7	0.60±0.06	11.2	···	0.71	···
... C35	20:17:59.9	+36:47:02.7	0.46±0.04	18.6	···	0.71	···
S148/S149							
... C1	22:56:44.9	+58:30:06.24	$1.07±0.11$	26.7	7.4	-55.05	-55.67
... C2	22:56:43.9	+58:28:14.88	1.03±0.11	22.3	9.8	-54.97	-54.26
... C3	22:56:18.8	+58:33:14.99	0.87±0.09	27.0	9.2	-55.08	-55.09
... C4	22:56:02.3	+58:33:13.90	0.94±0.1	25.8	10.6	-55	-55.46
... C5	22:56:17.2	+58:31:02.99	0.94±0.1	35.0	14.6	-52.58	-52.14
... C6	22:56:26.1	+58:30:55.00	1.06±0.11	24.8	9.1	-54.21	-54.05
... C7	22:56:19.1	+58:29:48.99	0.77±0.07	21.8	5.4	-51.67	-51.48
... C8	22:56:42.3	+58:31:51.89	0.90±0.1	18.8	2.5	-54.17	-54.33
... C9	22:56:21.6	+58:32:32.49	0.84±0.09	18.2	8.3	-53.94	-51.46
... C10	22:56:13.7	+58:33:15.98	0.86±0.09	23.8	2.6	-54.53	-54.66
... C11	22:56:03.9	+58:31:34.90	0.74±0.08	20.4	2.8	-53.7	-53.35
... C12	22:55:56.8	+58:29:11.84	0.75±0.08	20.4	5.8	-54.81	-54.8
... C13	22:56:13.5	+58:30:05.48	0.55±0.06	16.0	···	-53.1	···
S152							
... C1	22:58:56.1	+58:46:29.27	$0.32±0.03$	20.3	15.9	-50.68	-50.87

Table 3.2—Continued

ID	RA	DEC	R_e (pc)	$^{12}T_b$ (K)	$^{13}T_b$ (K)	V_{12} (km s^{-1})	V_{13} (km s^{-1})
... C2-a	22:58:44.3	+58:46:51.50	0.33±0.03	35.7	···	-50.72	···
... C2-b	22:58:40.6	+58:46:31.67	0.32±0.03	43.9	20.9	-49.85	-49.84
... C2-c	22:58:38.1	+58:46:44.50	0.33±0.03	35.3	···	-49.77	···
... C3	22:58:39.7	+58:48:15.50	0.37±0.03	30.0	20.5	-49.25	-49.79
... C4	22:58:47.7	+58:45:19.32	0.42±0.04	27.4	17.0	-50.84	-50.74
... C5	22:58:59.5	+58:45:32.08	0.31±0.03	21.0	12.1	-50.68	-50.71
... C6	22:58:59.7	+58:48:29.41	0.34±0.03	20.8	9.4	-50.92	-50.95
... C7	22:59:04.0	+58:49:54.53	0.37±0.03	18.9	9.0	-50.84	-50.58
... C8	22:58:31.8	+58:45:12.32	0.25±0.02	22.2	7.5	-51.79	-49.86
S175A							
... C1	0:27:29.6	+64:43:41.30	0.13±0.024	28.4	12.2	-49.39	-49.14
... C2	0:27:27.5	+64:44:45.21	0.13±0.024	23.0	5.8	-48.98	-49.03
... C3	0:27:22.0	+64:45:34.30	0.17±0.033	17.8	7.4	-49.39	-49.03
... C4	0:27:19.8	+64:44:52.34	0.12±0.023	27.2	13.7	-49.39	-49.14
... C5	0:27:04.6	+64:43:49.51	0.16±0.031	42.2	25.1	-49.39	-49.35
... C6	0:27:02.3	+64:43:28.53	0.16±0.031	41.2	20.9	-49.79	-49.67
... C7	0:27:28.5	+64:43:42.19	0.15±0.028	29.9	8.3	-49.39	-49.56
... C8	0:27:15.4	+64:42:46.60	0.22±0.042	33.7	14.3	50	-49.99
... C9	0:26:55.7	+64:43:35.58	0.17±0.033	30.7	16.8	-50.2	-49.67
... C10	0:26:51.4	+64:43:35.58	0.17±0.033	21.7	10.7	-50.81	-50.52
... C11	0:26:41.5	+64:42:32.59	0.19±0.037	15.7	2.7	-50.81	-50.62
... C12	0:26:41.5	+64:43.35.58	0.16±0.032	15.8	3.3	-50.01	-50.84
... C13	0:26:37.2	+64:44:38.57	0.16±0.030	13.9	5.2	-50.01	-50.94
S175B							
... C1	0:26:05.4	+64:54:20.87	0.18±0.04	17.5	7.1	-52.03	-51.12
... C2	0:26:19.7	+64:53:32.71	0.14±0.03	20.0	3.8	-51.62	-51.12

Table 3.2—Continued

ID	RA	DEC	R_e (pc)	$^{12}T_b$ (K)	$^{13}T_b$ (K)	V_{12} (km s^{-1})	V_{13} (km s^{-1})
... C3	0:26:10.9	+64:53:03.86	0.11±0.02	13.3	5.1	-52.23	-51.99
... C4	0:25:55.5	+64:51:18.84	0.26±0.05	14.3	6.2	-52.03	-51.22
... C5	0:26:17.5	+64:51:18.84	0.24±0.05	24.4	5.8	-49.8	-49.75
... C6	0:26:23.0	+64:52:49.81	0.14±0.03	15.1	5.0	-49.39	-49.56
... C7	0:26:34.0	+64:52:49.71	0.25±0.05	13.5	6.5	-50.61	-49.57
... C8	0:26:31.8	+64:53:24.73	0.24±0.05	13.8	8.9	-50.81	-49.49
... C9	0:26:32.9	+64:54:27.72	0.26±0.05	15.5	9.3	-50.61	-49.49
... C10	0:26:28.5	+64:54:06.77	0.21±0.04	18.6	8.3	-48.78	-49.22
... C11	0:26:40.6	+64:54:55.63	0.17±0.03	14.6	9.2	-48.78	-49.3
... C12	0:26:50.4	+64:51:18.64	0.32±0.06	15.0	···	-48.78	···
S192							
... C1	2:47:48.1	+61:55:41.67	0.35±0.06	16.9	7.9	-44.59	-44.67
... C2	2:47:48.0	+61:54:45.68	0.23±0.04	10.8	2.4	-45.4	-45.52
... C3	2:47:35.2	+61:56:59.35	0.33±0.06	20.8	3.6	-46.01	-46.05
... C4	2:47:35.3	+61:57:55.35	0.24±0.04	16.3	4.5	-46.01	-46.16
... C5	2:47:27.3	+61:57:27.73	0.35±0.06	18.5	7.7	-47.03	-47.54
... C6	2:47:26.3	+61:56:38.78	0.53±0.09	22.9	11.1	-46.83	-46.8
... C7	2:47:25.4	+61:59:05.82	0.33±0.06	12.9	3.4	-46.62	-46.8
... C8	2:47:12.4	+61:56:25.37	0.45±0.08	15.9	3.0	-47.44	-47.97
... C9	2:47:31.1	+61:54:46.55	0.35±0.06	10.8	2.1	-45.4	-48.71
... C10	2:47:15.5	+61:59:27.25	0.36±0.06	8.1	···	-49.47	···
S196							
... C1	2:52:06.7	+62:09:58.04	0.56±0.12	15.1	···	-42.56	···
... C2	2:51:59.7	+62:09:30.46	57±0.12	16.5	···	-43.98	···
... C3	2:51:38.7	+62:09:31.56	29±0.06	15.1	1.3	-43.78	-43.72
... C4	2:51:14.8	+62:11:45.58	0.53±0.11	16.5	4.6	-44.59	-44.57

Table 3.2—Continued

ID	RA	DEC	R_e (pc)	$^{12}T_b$ (K)	$^{13}T_b$ (K)	V_{12} (km s^{-1})	V_{13} (km s^{-1})
... C5	2:51:22.9	+62:13:44.27	0.45±0.1	7.0	1.0	-45	-44.67
... C6	2:51:28.0	+62:13:14.05	0.45±0.10	7.3	0.6	-45.41	-45.31
... C7	2:51:36.8	+62:10:27.70	0.51±0.10	13.1	4.4	-47.23	-47.54
... C8	2:51:44.8	+62:10:34.27	0.51±0.11	12.1	2.6	-46.62	-46.59
S212							
... C1	4:40:34.2	+50:27:05.98	0.72±0.07	31.3	5.1	-33.05	-35.11
... C2	4:40:38.7	+50:27:05.73	0.9±0.09	29.3	10.2	-33.46	-33.51
... C3	4:40:42.4	+50:27:54.51	1.11±0.11	33.0	10.8	-32.85	-33.09
... C4	4:40:47.5	+50:27:40.21	1.0±0.1	23.2	6.0	-35.08	-35.42
... C5	4:40:50.4	+50:27:40.02	0.94±0.09	22.1	4.9	-35.29	-35.21
... C6	4:40:54.0	+50:27:04.75	0.97±0.1	20.6	2.9	-35.69	-35.74
... C7	4:41:01.4	+50:28:14.24	1.25±0.12	17.7	5.2	-35.49	-36.49
... C8	4:41:04.3	+50:27:04.03	1.35±0.13	15.6	2.9	-35.69	-36.49
... C9	4:40:48.3	+50:28:59.76	0.95±0.09	10.5	1.9	-39.15	-38.82
... C10	4:40:45.2	+50:26:30.33	0.86±0.09	12.6	2.0	-34.07	-34.26
... C11	4:40:43.1	+50:27:26.46	0.85±0.08	16.0	3.2	-34.68	-35
... C12	4:40:39.4	+50:26:23.69	0.73±0.07	15.7	2.5	-33.05	-35
S288							
... C1	7:08:39.2	-04:19:21.80	0.55±0.22	24.9	···	58.38	···
... C2	7:08:37.4	-04:18:53.80	0.54±0.21	28.0	···	56.16	···
... C3	7:08:34.6	-04:17:15.80	0.61±0.25	9.9	···	56.56	···
... C4	7:08:42.5	-4:18:46.80	0.35±0.14	11.3	···	56.95	···
S305							
... C1	7:30:04.7	-18:30:25.27	0.75±0.20	25.8	9.3	42.64	43.29
... C2	7:30:12.6	-18:32:03.82	0.86±0.23	33.0	9.6	43.66	42.87
... C3	7:29:59.3	-18:30:52.89	0.64±0.17	32.1	8.6	43.86	43.93

Table 3.2—Continued

ID	RA	DEC	R_e (pc)	$^{12}T_b$ (K)	$^{13}T_b$ (K)	V_{12} (km s^{-1})	V_{13} (km s^{-1})
... C4	7:30:16.6	-18:31:15.08	0.61±0.17	26.1	11.0	44.88	44.14
... C5	7:29:59.8	-18:32:37.92	0.51±0.14	24.7	9.2	44.06	42.77
... C6	7:29:59.8	-18:32:37.92	0.63±0.17	20.2	2.8	44.67	44.46
... C7	7:30:00.3	-18:31:48.96	0.62±0.17	59.2	14.5	46.91	46.69
... C8	7:30:06.2	-18:32:59.38	0.57±0.15	23.6	3.0	46.3	46.69
... C9	7:30:00.3	-18:33:33.96	0.64±0.17	35.1	16.4	47.11	46.8
... C10	7:30:02.7	-18:33:34.13	0.57±0.15	16.8	2.7	47.72	48.39
... C11	7:30:14.0	-18:34:37.91	0.70±0.19	12.0	2.3	47.32	44.67
... C12	7:30:17.0	-18:33:56.11	0.85±0.23	16.3	···	44.07	···
S307							
... C1	7:35:33.3	-18:44:59.00	0.25±0.06	25.2	10.5	44.53	44.35
... C2-a	7:35:33.3	-18:45:20.50	0.28±0.06	28.1	9.1	45.26	44.68
... C2-b	7:35:33.2	-18:45:34.50	0.26±0.06	32.5	6.9	45.842	46.42
... C3	7:35:36.3	-18:46:25.83	0.43±0.1	38.0	11.2	46.6	46.55
... C4	7:35:38.7	-18:48:57.50	0.47±0.12	44.5	19.5	47.04	46.72
... C5	7:35:31.8	-18:46:23.50	0.32±0.07	28.2	5.0	46.78	46.88
... C6-a	7:35:41.7	-18:46:16.49	0.35±0.08	19.1	1.4	46.01	46.18
... C6-b	7:35:42.5	-18:46:30.49	0.34±0.08	12.7	1.7	48.22	48.25
... C7	7:35:37.4	-18:44:54.83	0.23±0.05	15.0	3.7	45.8	47.79
... C8	7:35:43.1	-18:48:35.32	0.37±0.09	26.9	8.4	47.11	47.21
... C9	7:35:43.7	-18:43:55.32	0.23±0.05	12.1	2.4	47.06	47.13
... C10	7:35:41.0	-18:44:59.49	0.32±0.07	14.3	3.6	47.29	47.34

Table 3.3. Physical parameters calculated for all clumps

Clump No.	T_{ex} (K)	ΔV_{12} (km s^{-1})	ΔV_{13} (km s^{-1})	$N(H)$ ($\times 10^{20}$cm^{-2})	$n_{int}(H_2)$ (cm^{-3})	M$_{int}$ (M$_\odot$)	τ_{12}	τ_{13}
S104								
...C1	18.46	2.37	1.02	18.13	34.5	53±9	17	0.27
...C2	15.631	2.81	3.05	31.77	11.9	13±2	13	0.21
...C3	25.844	3.56	···	···	34.3	45±8	···	···
...C4	50.193	2.16	1.91	427.26	41.7	92±15.9	33	0.54
...C5	17.77	1.78	···	···	14.4	8±1.3	···	···
...C6	16.483	3.52	1.55	31.81	16.3	10±1.6	24	0.38
...C7	34.219	2.62	0.79	42.39	33.5	59±10	16	0.27
...C8	40.132	2.47	0.71	131.53	42.1	85±15	42	0.68
...C9	27.714	2.71	2.15	190.27	35.9	51±9	40	0.64
...C10	39.111	3.55	2.07	243.36	44.2	65±11	28	0.45
...C11	32.405	2.49	1.48	100.94	36.3	52±9	23	0.37
...C12	31.932	2.12	1.87	210.72	35.4	65±11	39	0.63
...C13	37.462	2.57	1.19	146.19	46.1	51±9	32	0.51
...C14	37.352	2.69	1.87	102.59	41.6	46±8	14	0.23
...C15	27.957	2.05	1.26	78.92	21.2	44±8	28	0.45
...C16	28.711	2.47	1.97	159.49	28.0	34±6	34	0.55
...C17	31.784	2.13	1.63	51.45	15.8	19±3	11	0.18
...C18	20.363	2.99	1.67	21.06	13.1	23±4	10	0.16
...C19	29.326	2.85	2.02	73.27	24.2	36±6	15	0.24
...C20	17.82	1.87	1.31	10.42	9.5	8±1.4	8	0.13
...C21	27.45	2.31	1.89	51.04	39.6	17±2.9	12	0.20
...C22	26.855	2.77	···	···	26.2	19±3	···	···
...C23	19.414	2.4	1.64	33.31	19.6	9±1.6	18	0.28
...C24	23.031	1.29	1.06	25.51	9.0	7±1.3	15	0.25
...C25	29.66	2.2	2.22	204.5	14.7	31±5	37	0.59

Table 3.3—Continued

Clump No.	T_{ex} (K)	ΔV_{12} (km s^{-1})	ΔV_{13} (km s^{-1})	$N(H)$ ($\times 10^{20}$cm^{-2})	$n_{int}(H_2)$ (cm^{-3})	M$_{int}$ (M$_\odot$)	τ_{12}	τ_{13}
...C26	27.419	2.17	···	···	32.3	32±6	···	···
...C27	16.936	2.34	···	···	18.9	15±2.6	···	···
...C28	18.289	3.16	···	···	15.0	59±10	···	···
...C29	18.468	1.53	···	···	14.3	11±2	···	···
...C30	18.421	1.87	···	···	9.9	51±9	···	···
...C31	13.665	2.01	···	···	14.2	48±8	···	···
...C32	27.729	2.26	···	···	28.1	40±7	···	···
...C33	14.057	1.98	···	···	9.7	13±2.2	···	···
...C34	16.305	1.88	···	···	6.7	35±6	···	···
...C35	23.883	2.8	···	···	22.0	51±9	···	···
S149								
...C1	32.079	4.21	2.62	152.34	47.9	1400±290	20	0.32
...C2	27.708	6.75	2.79	218.55	48.8	1280±260	35	0.57
...C3	32.395	1.86	0.92	69.01	27.3	435±89	25	0.41
...C4	31.238	1.67	1.36	122.4	20.9	412±84	32	0.52
...C5	40.48	3.27	2.42	361.84	48.1	960±196	33	0.54
...C6	30.229	3.83	1.04	76.15	31.3	900±184	28	0.45
...C7	27.16	3.71	1.57	58.08	35.7	900±77	17	0.28
...C8	24.099	2.19	1.65	25.16	18.5	386±67	9	0.14
...C9	23.551	2.19	1	60.59	10.3	328±30	37	0.60
...C10	29.216	2.15	1.65	28.16	29.0	440±90	7	0.11
...C11	25.703	2.38	1.53	26.79	21.4	211±43	9	0.15
...C12	25.727	1.39	0.9	34.43	11.6	118±24	21	0.34
...C13	21.24	2.27	···	···	21.3	191±53	···	···
S152								
...C1	25.647	5.28	1.37	508.99	156.0	117±18	93	1.51

Table 3.3—Continued

Clump No.	T_{ex} (K)	ΔV_{12} (km s^{-1})	ΔV_{13} (km s^{-1})	$N(H)$ ($\times 10^{20}$cm^{-2})	$n_{int}(H_2)$ (cm^{-3})	M$_{int}$ (M$_\odot$)	τ_{12}	τ_{13}
...C2-a	41.211	4.66	···	···	207.0	176±28	···	···
...C2-b	49.415	4.35	1.75	456.5	233.0	175±28	40	0.64
...C2-c	40.782	4.87	···	···	213.0	181±29	···	···
...C3	35.468	4.76	1.69	416.42	151.0	189±30	70	1.13
...C4	32.78	7.42	3.15	566.29	165.0	295±47	60	0.96
...C5	26.311	2.43	1.59	168.75	77.0	56±9	53	0.85
...C6	26.121	3.04	2.04	148.31	84.0	82±13	37	0.59
...C7	24.242	2.43	1.07	73.02	519.0	633±100	39	0.63
...C8	27.516	6.04	2.52	139.02	268.0	97±15	25	0.41
S175A								
...C1	33.828	0.97	0.56	61.83	118.9	6±2.0	34	0.56
...C2	28.362	0.78	0.47	19.38	82.4	4±1.4	18	0.29
...C3	23.076	1.12	0.66	34.68	49.6	6±2.1	33	0.54
...C4	32.626	0.92	0.56	72.12	118.7	5±1.6	43	0.69
...C5	47.676	1.31	0.85	290.4	139.7	14±5	56	0.90
...C6	46.698	1.61	0.95	243.38	201.2	19±7	44	0.70
...C7	35.307	0.97	0.64	44.75	113.7	9±3.1	20	0.33
...C8	39.128	1.12	0.74	105.94	71.4	18±6.4	34	0.55
...C9	36.178	1.54	1.08	190.75	126.8	15±5.2	49	0.78
...C10	27.025	1.59	0.93	82.41	77.1	9±3.2	42	0.68
...C11	20.901	1.25	0.87	13.28	35.8	6±2.1	12	0.19
...C12	21.039	1.15	0.71	13.5	63.2	7±2.4	14	0.23
...C13	19.084	1.32	0.62	20.09	70.6	6±2.3	29	0.47
S175B								
...C1	22.819	8.68	1.44	70.78	220.9	31±11	32	0.51
...C2	25.341	4.1	1.4	34.42	183.0	12±4.1	13	0.21

Table 3.3—Continued

Clump No.	T_{ex} (K)	ΔV_{12} (km s^{-1})	ΔV_{13} (km s^{-1})	$N(H)$ ($\times 10^{20}$cm^{-2})	$n_{int}(H_2)$ (cm^{-3})	M$_{int}$ (M$_\odot$)	τ_{12}	τ_{13}
...C3	18.466	4.87	1.57	49.57	178.1	6±2.2	30	0.48
...C4	19.52	2	1.26	51.17	38.6	16±5.6	35	0.56
...C5	29.769	1.04	0.75	31.58	48.7	17±5.8	17	0.27
...C6	20.339	2.6	1.09	33.82	139.0	9±3.1	25	0.40
...C7	18.71	2.77	1.32	57.33	63.0	24±9	40	0.65
...C8	19.019	3.3	1.22	85.83	86.2	29±10	63	1.02
...C9	20.774	2.72	1.39	100.91	64.6	26±9	56	0.90
...C10	23.955	1.94	1.17	71.86	93.4	22±8	36	0.59
...C11	19.838	2.6	1.4	101.21	93.3	10±3.6	60	0.97
...C12	20.274	1.13	···	···	16.4	12±4.3	···	···
S192								
...C1	22.204	1.49	0.82	46.41	27.0	26±8	38	0.62
...C2	15.906	1.29	0.83	10.26	23.6	7±2	15	0.25
...C3	26.156	2.19	1.76	40.57	71.0	61±19	12	0.19
...C4	21.597	1.04	0.75	20.89	29.9	9±3.0	20	0.32
...C5	23.829	2.05	0.98	53.91	58.5	57±18	33	0.53
...C6	28.272	3.45	2.13	199.34	6.1	22±7	41	0.66
...C7	18.041	1.76	1.2	23.06	22.6	19±6	19	0.31
...C8	21.167	1.98	1.27	21.93	28.0	61±20	13	0.21
...C9	15.906	1.28	0.63	6.64	14.1	14±4.5	13	0.21
...C10	13.057	0.94	···	···	6.6	8±2.4	···	···
S196								
...C1	20.336	3.09	···	···	42.9	179±73	···	···
...C2	21.804	2.83	···	···	44.6	201±82	···	···
...C3	20.336	0.83	0.71	4.96	11.2	6±2.6	6	0.09
...C4	21.804	1.7	0.92	25.97	16.4	58±24	20	0.32

Table 3.3—Continued

Clump No.	T_{ex} (K)	ΔV_{12} (km s^{-1})	ΔV_{13} (km s^{-1})	$N(H)$ ($\times 10^{20}$cm^{-2})	$n_{int}(H_2)$ (cm^{-3})	M$_{int}$ (M$_\odot$)	τ_{12}	τ_{13}
...C5	11.839	2.05	1.15	5.12	10.1	23±9	9	0.15
...C6	12.203	1.37	1.4	3.63	5.7	13±5.2	5	0.08
...C7	18.271	1.6	1.11	28.71	18.0	58±24	25	0.40
...C8	17.275	1.2	0.68	9.53	13.4	41±17	15	0.24
S212								
...C1	36.717	3.29	1.48	60.59	53.5	479±90	11	0.18
...C2	34.708	2.91	1.58	139.7	38.0	671±125	26	0.42
...C3	38.483	3.81	1.8	178.81	31.0	1028±193	24	0.39
...C4	28.605	3.75	2.15	92.13	34.8	836±157	18	0.30
...C5	27.506	1.57	1.09	36.84	16.7	335±63	15	0.25
...C6	25.897	2.77	1.03	18.97	21.0	463±87	9	0.15
...C7	22.956	3.08	1.37	46	15.6	738±138	21	0.35
...C8	20.845	2.31	0.74	12.3	10.6	624±117	13	0.20
...C9	15.565	2.67	2.2	21.3	10.7	223±42	12	0.20
...C10	17.794	2	1.35	13.94	15.2	232±44	10	0.17
...C11	21.207	2.63	1.94	35.61	29.2	430±81	14	0.22
...C12	20.965	3.04	2.25	31.97	36.1	341±64	11	0.17
S288								
...C1	30.282	3.84	···	···	38.4	150±114	···	···
...C2	33.4	3.44	···	···	44.4	164±125	···	···
...C3	14.967	1.43	···	···	8.1	45±34	···	···
...C4	16.42	1.66	···	···	15.9	17±13	···	···
S305								
...C1	31.248	2.66	1.95	148.43	42.0	430±220	28	0.44
...C2	38.498	3.42	1.72	148.74	49.4	760±390	21	0.34
...C3	37.608	2.45	1.54	115.31	57.9	361±185	19	0.31

Table 3.3—Continued

Clump No.	T_{ex} (K)	ΔV_{12} (km s^{-1})	ΔV_{13} (km s^{-1})	$N(H)$ ($\times 10^{20}$cm^{-2})	$n_{int}(H_2)$ (cm^{-3})	M$_{int}$ (M$_\odot$)	τ_{12}	τ_{13}
...C4	31.497	1.93	1.04	97.79	40.0	223±114	34	0.54
...C5	30.091	1.74	1.13	83.23	32.6	189±97	29	0.46
...C6	25.524	1.32	1.01	17.89	33.9	107±55	9	0.15
...C7	64.765	2.4	1.43	272.49	77.5	466±239	17	0.28
...C8	29.006	2.68	2.14	43.7	37.6	169±87	8	0.14
...C9	40.628	1.73	1.26	220.45	41.1	256±131	39	0.62
...C10	22.026	1.76	1.18	18.58	27.8	125±64	11	0.18
...C11	17.174	3.49	1.4	16.67	40.9	344±176	13	0.21
...C12	21.552	3.2	...	...	27.5	407±208	...	...
S307								
...C1	30.617	2.18	1.11	97.93	101.3	38±16	33	0.54
...C2-a	33.508	2.48	1.11	126.02	71.3	37±16	24	0.39
...C2-b	38.003	2.41	2.26	132.25	104.8	44±19	15	0.24
...C3	43.504	2.59	2.28	251.74	78.4	152±66	21	0.35
...C4	50.001	3.35	2.16	513.66	99.7	251±108	35	0.57
...C5	33.622	2.22	1.89	71.85	70.3	56±24	12	0.19
...C6-a	24.456	1.58	1.03	8.67	29.8	31±14	5	0.08
...C6-b	17.912	1	0.7	6.24	19.3	18±8	9	0.14
...C7	20.192	1.62	0.6	12.99	54.2	16±7	18	0.28
...C8	32.338	2.63	1.38	93.76	100.0	124±54	23	0.37
...C9	17.279	1.07	0.68	8.59	24.8	7±3.2	14	0.22
...C10	19.474	1.32	1	20.46	25.0	19±8	18	0.29

Table 3.4. The Larson power law index for each region

Source	$\alpha[\Delta V_{12}]$	$\alpha[\Delta V_{13}]$	^{12}CO Correlation Coefficient	^{13}CO Correlation Coefficient	Source type
S104	1.0 ± 0.04	-1.2 ± 0.4	0.007	-0.1	II
S148/S149	3.0 ± 0.5	2.5 ± 0.7	0.66	0.49	I
S152	-1± 0.9	-1.2± 0.8	0.019	-0.1	II
S175A	1.3 ± 0.3	1.4 ± 0.3	0.55	0.64	I
S175B	-1.7 ± 0.4	-0.75 ± 0.2	-0.59	-0.38	II
S192/193	1.5 ± 0.2	1.5 ± 0.2	0.67	0.62	I
S196	1.9 ± 0.4	1.2 ±0.2	0.78	0.34	I
S212	-1.0± 0.1	-1.6 ± 0.4	-0.022	-0.48	II
S305	1.9 ± 0.2	1.6 ± 0.2	0.79	0.51	I
S307	1.4 ± 0.2	1.9 ± 0.2	0.44	0.53	I

Chapter 4

Star Formation at the Borders of H II Regions

Expansion of H II regions within molecular clouds forms dense envelopes around the ionized gas fronts. The collected shells may not be gravitationally stable and may collapse and initiate star formation. The "collect and collapse" model of triggered star formation is now well developed theoretically (Elmegreen & Lada 1977) and is confirmed observationally (e.g Deharveng et al. 2005). Many observational studies have confirmed triggered star formation at the borders of expanding H II regions. For example in an observational investigation of collect and collapse candidates in a sample of 20 H II regions (Deharveng et al. 2005, 2006, 2008, 2009, Zavagno et al. 2006, Pomares 2009) young stellar clusters embedded within dense molecular gas at peripheries of H II regions have been

found. Dense clumps formed within the collected gas also may host massive cores which produce the next generation of massive stars. Regions forming rich embedded clusters require high densities ($n > 10^5$ cm^{-3}) and they are more fragmented. A lower density with less fragmentation may produce a smaller number of stars (Lada et al. 1997).

Molecular gas emissions were used to study the structure and fragmentation of the gas while the near infrared imaging provides the information of the stellar components within the area and probably the sources embedded within the gas. Luminous red point sources could be candidates for young massive proto-stars or stellar groups.

In this chapter we investigate the stellar population within the areas we have mapped around H II regions using near-IR data. We look at the spatial distribution of stars and how that distribution relates to the cloud structure and also look for candidates of Young Stellar Objects (YSOs). Two types of clusters were identified in this study: young clusters embedded within dense clumps at the peripheries of H II regions which probably have been triggered by the expansion of the ionized gas, and open clusters with more main sequence stars that contain the exciting star and overlap with the H II region.

4.1 The Two Micron All Sky Survey (2MASS) Data

The Two Micron All Sky Survey (2MASS) is the deepest uniform scan of the entire sky in three near-IR J (1.25 μm), H(1.65 μm) and K_s (2.17 μm) bands to a 3σ detecting threshold of 17.1, 16.4 and 15.3 mag for each band, respectively. All point sources brighter than 1 mJy in each band with signal to noise ratio (S/N) larger than 10, with a pixel size of 2.0″ is detected and characterized.

We selected 2MASS point sources within our 11 mapped regions in ^{12}CO(2-1). Only sources with photometric quality of Qflg = AAA were selected. This quality flag means a S/N greater than 10 and corrected photometric uncertainty (cmsig)$<$ 0.10857. This criterion reduces the confusion with background and field stars with spectral types later than F0 while selecting the range for young stellar candidates of high and intermediate mass stars.

Colour-colour and colour-magnitude diagrams help to identify the nature of the sources in each sample. For example, point sources with red excess in a (J-H) - (H-K_s) colour-colour diagrams could be candidates YSOs. We plot (J-H) versus (H-K_s) diagrams for 2MASS sources detected within our mapped regions. We study the stellar population in each region and discuss how it might have been affected by the physical conditions of the cloud.

4.1.1 Methods

We plot the $(J-H)$ vs. $(H-K)$ colour-colour diagrams to understand the nature of the detected sources in 2MASS images. Stars in different evolutionary stages stand at different portions of the diagram. We accept the reddening-free quantity q, defined by Romero and Cappa (2009) following the previous works (Comeron & Pasquali, 2005), to separate early type stars from background red giants:

$$q = (J-H) - 1.8 \times (H-K). \tag{4.1}$$

Main sequence stars have q values between -0.15 and 0.10. Object with red excess have smaller qs ($q < -0.15$) and giant stars have q larger than 0.2. In the case of S104 and S307 there is contamination between giants and the main sequence stars on the colour-colour diagram. To keep the safe side, we accept the sources with $q > 0.25$ as giants for S307 and $q > 0.4$ for S104.

We estimated the star formation efficiency (SFE) by counting the detected sources in K band within the selected clumps. The clump edge was taken as defined for clump mass estimation in Chapter 2. The total stellar mass is estimated assuming an average of 1 $M_{\odot}$ for detected point sources within each clump. The 2MASS data is not deep enough and it does not identify the embedded faint sources, therefore the number of detected sources especially for lower mass stars might be under-estimated. The total stellar mass is then estimated just based on massive luminous stars. Deep NIR observations are needed for more accurate SFE estimation.

4.2 S104

Figure 4.1 shows ^{12}CO(2-1) contours super-imposed on a 2MASS K_s band image. The thick white curve presents the visible boundaries of the H II region from Digital Sky survey red images. The molecular gas has been swept by the expansion of the ionized gas and fragmented into dense clumps in shells around the H II region. Such conditions favour triggered star formation.

A compact stellar cluster is detected in 2MASS data associated with the hot dense clump C4, at the left side of the image. C4 has a high T_{ex} of 36 K and N(H)=334×10^{20} cm^{-2}. The clump is gravitationally unstable in this condition and will likely fragment to several smaller cores. This cluster is probably a second generation of stars formed through the "collect and collapse" model. The star formation efficiency (the fraction of total mass in stars to total mass in gas plus total mass in stars) is about 35% which is higher than general star formation efficiency in molecular clouds (less than 10% up to 20%, Jorgenssen et al., 2008) Deharveng et al. (2003) introduced S104 as a prototype of massive star formation triggered by the expansion of H II region. They have studied the embedded cluster with deep CFHT infrared imaging. Figure 4.2 shows the embedded cluster super-imposed on an integrated C^{18}O(2-1) map from the IRAM 30m telescope. The data reduction and results of these observations are yet to be published.

In the right hand panel of Figure 4.1 we present the colour-colour diagram of the stars within our ^{12}CO(2-1) map using 2MASS data. The solid thick

line shows the main sequence and the giant branch (Koornneef 1983). The dashed lines show the reddening lines for B1V and late type M0V stars using standard extinction curves (Stahler & Palla 2004) and show a reddening of $A_V = 15$ mag (dust changes the colours that we observe and the reddening line shows the effect of this reddening on different colours). In total 687 sources were detected within the $12' \times 12'$ mapped area. The main sequence stars are shown in dots and the giants with open squares. 44 of the detected sources, shown as red open triangles, have an infrared excess and lie below the reddening line. Uncertainty in magnitude determination may cause a shift for the sources that lie close to the reddening line in colour-colour diagram but it is not very large (the 2MASS photometry uncertainties is smaller than 0.1 mag). These reddened objects could be candidates YSOs.

Figure 4.3 shows the K versus $(J - K)$ colour-magnitude diagram for the same sources. Black dots show the main sequence stars, blue squares show the giants and the red triangles show the sources with red excess. The reddening lines are drawn for an O9 and a B5 star. The solid curve marks the main sequence at the same distance of the exciting star of S104 with no extinction and the long-dashed curve shows the main sequence with a visual extinction of 3 mag. A second population of highly extincted stars ($A_V > 20$ mag) which are mostly giants (O and B stars) and sources with extra reddening is noticeable in the diagram with $(J-K) > 1.8$ (sources at right side of the vertical dotted line). Most of these sources are toward C4, the hot, dense clump at the borders of

the H II region which contains a young cluster. These all suggest that massive star formation is currently taking place in this region.

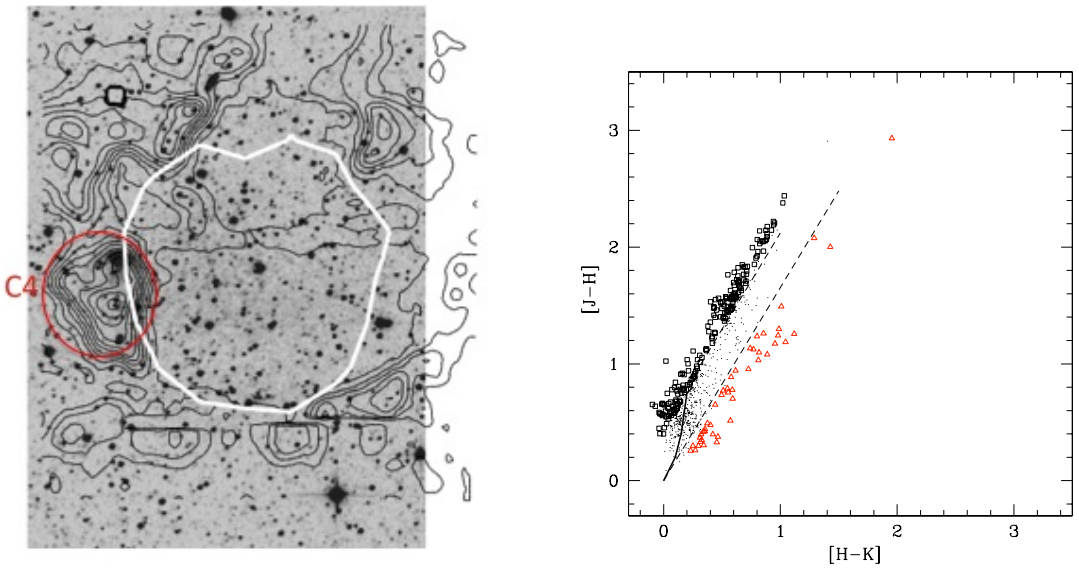

Figure 4.1 (left) Contours of the ^{12}CO(2-1) emission integrated between -10 and +10 km s^{-1} of S104 super-imposed on the 2MASS K_s band. A cluster associated with the hot dense clump C4, is detected at the East (left) side of the image. The thick white curve presents the visible boundary of the ionized gas from DSS red images. (right) The JHK colour-colour diagrams of the stars within Figure 4.1. The thick solid line presents the main sequence and the giant branch. The dashed lines are the reddening lines for B1V and M0V stars. The giants are presented with open squares. Red open triangles show the sources with red excess and black dots are main sequence stars.

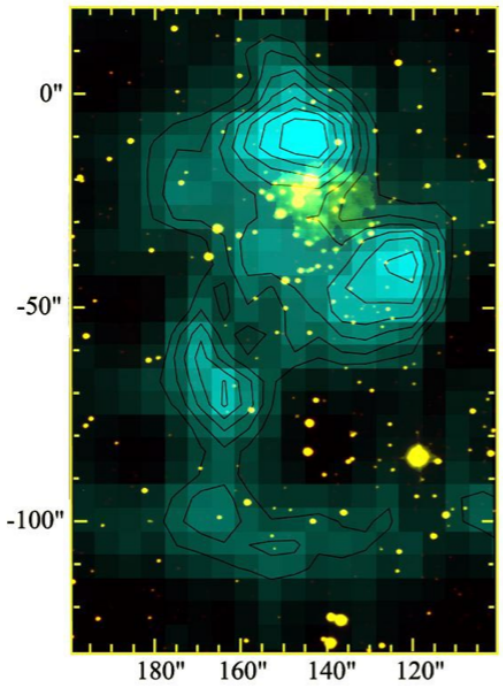

Figure 4.2 Map of the $C^{18}O$(2-1) of the molecular cloud fragment associated with the cluster super-imposed on a CFHT K band image of the cluster by Deharveng et al. (2003). The cluster is likely a second generation of young stars formed within the compressed shells of molecular gas by the expansion of the ionized gas.

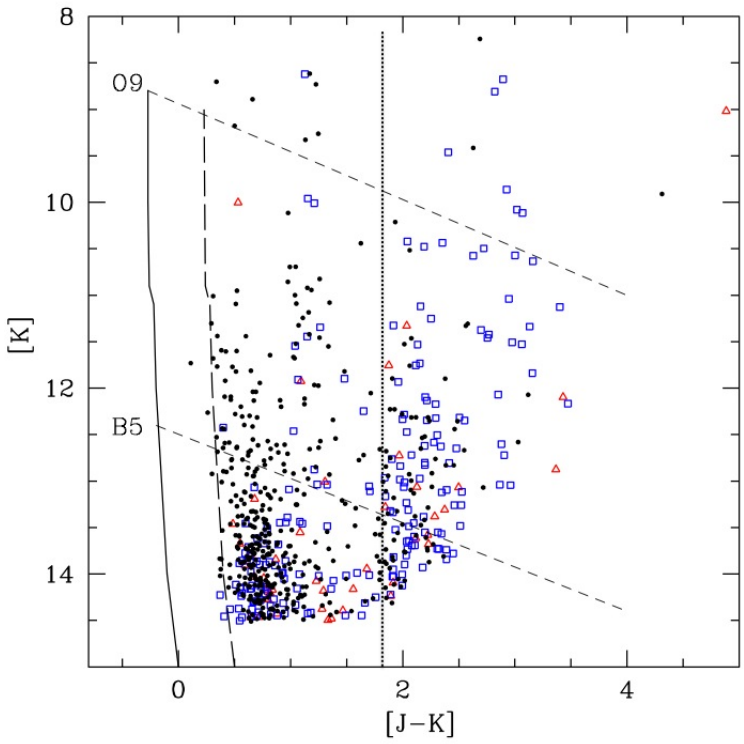

Figure 4.3 Colour-magnitude diagrams of the 2MASS sources toward S104. Black dots show the main sequence stars, blue squares show the giants and the red triangles show the sources with red excess. The reddening lines are drawn for an O9 and a B5 star. The solid curve marks the main sequence at the same distance of the exciting star of S104 with no extinction and the long-dashed curve shows the main sequence with a visual extinction of 3 mag. A second population of highly extincted stars is noticeable in the diagram with $(J-K) > 1.8$ (noted by vertical dotted line). Most of these sources are toward C4, the hot, dense clump at the borders of the H II region which contains a young cluster.

4.3 S148/S149

Figure 4.4 shows the contours of the ^{12}CO(2-1) emission of S148/S149 overlaid on the 2MASS K_s band image. The thick white curve shows the visible boundary of the H II region from DSS red images. The green circles note the positions of detected 2MASS objects. A cluster is detected at the position of the H II region. The B0V exciting star is probably a member of this cluster. That is consistent with the idea that massive stars form within the rich stellar clusters and the number density of the stars is well correlated with the H_2 density (e.g. Saito et al. 2007). The cluster associates with clump C5 which is the hottest clump in the mapped region (T_{ex} = 29.5 K). S148-C5 has a high column density of N(H) = 290 $\times 10^{20}$ cm^{-2} and a broad line width of ΔV_{12}= 3.27 km s^{-1}. The star formation efficiency of the clump is 5%, consistent with the general star formation efficiency in molecular clouds.

Figures 4.4 right panel and 4.5 show the colour-colour and colour-magnitude diagrams for the detected point sources (noted by green circles) in Figure 4.4 left panel. The overall extinction is about $A_V \sim 5$ mag. Three highly reddened sources (red triangles at the right side of both diagrams) locate roughly at the same position of C5 and could be YSOs candidates. A small number of giants are highly extincted but the nature of these sources cannot be determined without a NIR spectroscopy.

Stars with various masses may form from a single clump with large internal

motions. To form a dense core that can produce a massive star, the clump requires both a high gas density and large internal motion while it should also be gravitationally bound (McKee & Tan 2003). S148-C5 has a velocity integrated mass of $M_{int} = 960 \pm 196$ M$_\odot$ which considering uncertainties, is slightly larger than the Virial mass ($M_{vir} = 696 \pm 75$ M$_\odot$). The clump has enough mass to be gravitationally bound and satisfy the requirements of massive star formation.

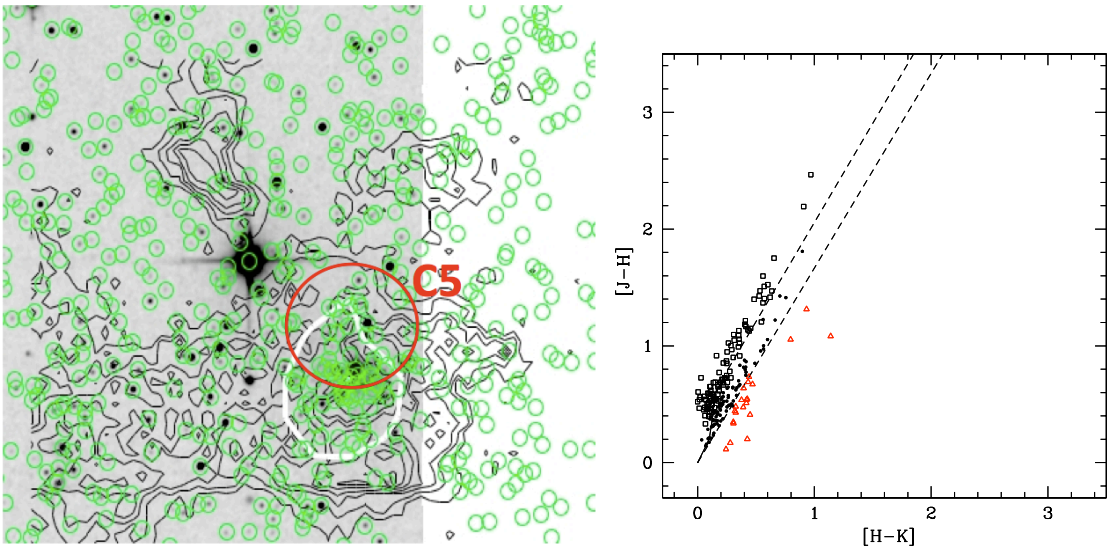

Figure 4.4 (Left) Contours of the ^{12}CO(2-1) emission of S148/S149 overlaid on the 2MASS K$_s$ band image. The thick white curve shows the visible boundary of the H II region from DSS red images. The green circles note the position of detected 2MASS objects. Note the high density of point sources at the centre of the H II region. The exciting star is probably a member of this cluster. (right) Colour-colour diagram for detected 2MASS sources in S148/S149 $7' \times 7'$ mapped area. The marks are the same as Figure 4.2.

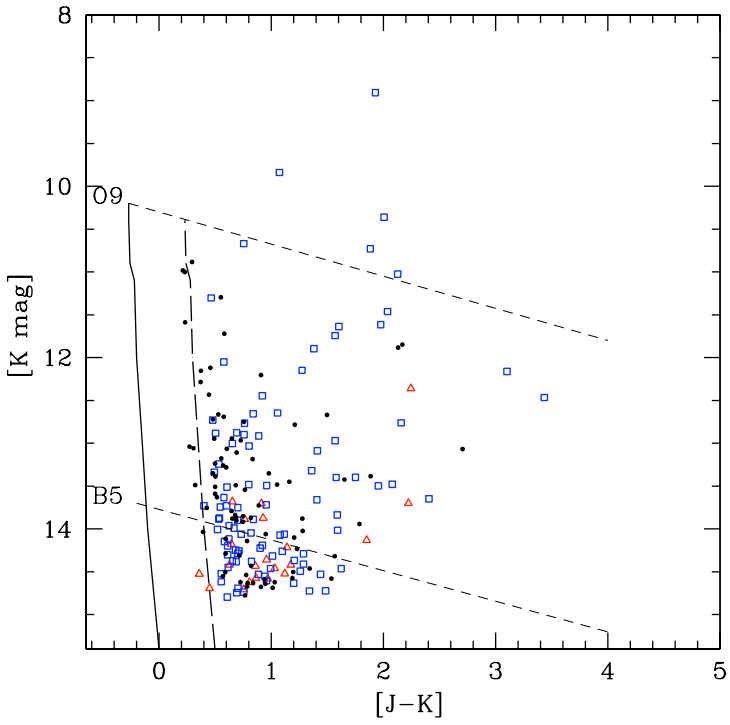

Figure 4.5 Colour-magnitude diagrams of the 2MASS sources toward S148/S149. The symbols and reddening lines are the same as Fig. 4.3.

4.4 S152

S152 is an active star-forming region. Several H_2O and one OH masers have been detected toward this molecular cloud (Heydari-Malayeri & Testor 1981). Similar to S148 the H II region is coincident with a stellar cluster. The O9V exciting star (Russeil et al. 2007) is probably a member of the cluster. S152 has large internal motions with large line widths (Table 3 in Chapter 3). The S152 cluster is also coincident with S152-C3 which has $\Delta V_{12} = 4.76$ km s^{-1} and $\Delta V_{13} = 1.69$ km s^{-1}. The clump has a high temperature ($T_{ex} = 26K$) and high density (N(H)= 340 $\times 10^{20}$ cm^{-2}). The clump also has larger M_{int} compared to M_{vir} (190 ± 30 vs. 135 ± 11) and is gravitationally stable. The star formation efficiency for this clump is estimated about 12% which is consistent with general star formation efficiency in molecular clouds.

A second smaller embedded cluster is noticeable associated with S152-C4. In a recent near-IR study, Chen et al. (2009) have detected an IR nebula and several point sources embedded within it (Figure 4.7). S152-C4 has the highest density (N(H)= 466 $\times 10^{20}$ cm^{-2}) and the largest line widths ($\Delta V_{12} = 7.42$ km s^{-1} and $\Delta V_{13} = 3.15$ km s^{-1}) among S152 clumps. That large line width is maybe due to a proto-stellar outflow.

We have detected 24 2MASS sources with IR colour excess in our colour-colour diagram (Figure 4.6 right panel) . Thirteen of these objects form a new population of red sources on colour-magnitude diagram (Figure 4.8) and are

good YSOs candidates indicating that star formation is active in this region.

In their study of a smaller region $4.2' \times 4.2'$ Chen et al. have identified 21 sources with an IR colour excess which exhibits the characteristics of T Tauri stars, Herbig Ae/Be stars or Class I proto-stars. Both clusters show evidence of sequential star formation. The larger cluster at the position of the H II region is more evolved and has mostly main sequence stars, as expected, but the other cluster is young and embedded in the dense clump covered by an IR nebula (Chen et al. 2009).

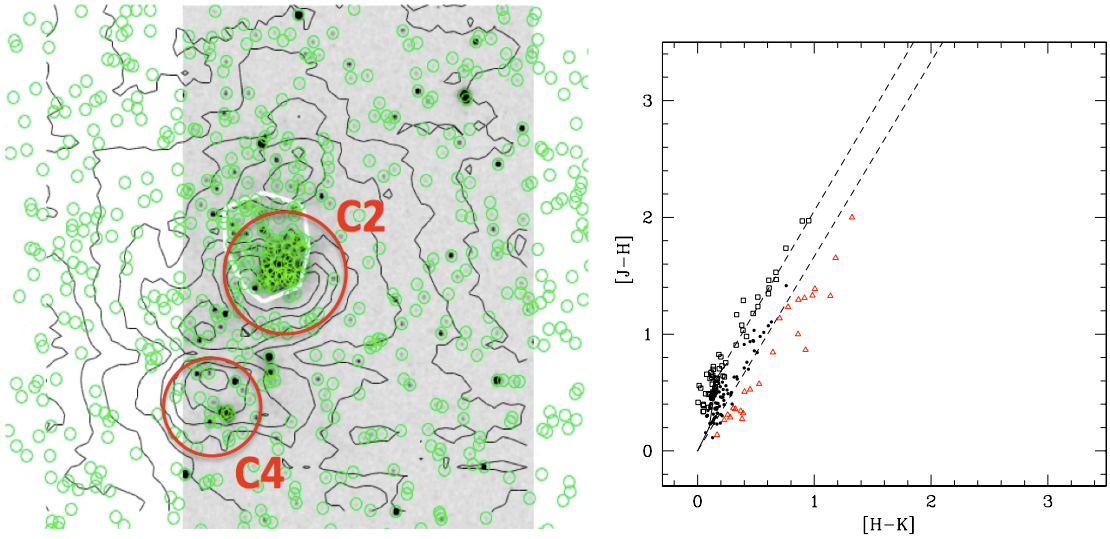

Figure 4.6 Same as Figure 4.4 for S152. A stellar cluster is located at the position of the H II region and the O9V exciting star is probably a member of the cluster. 24 2MASS sources with red excess has detected within the map.

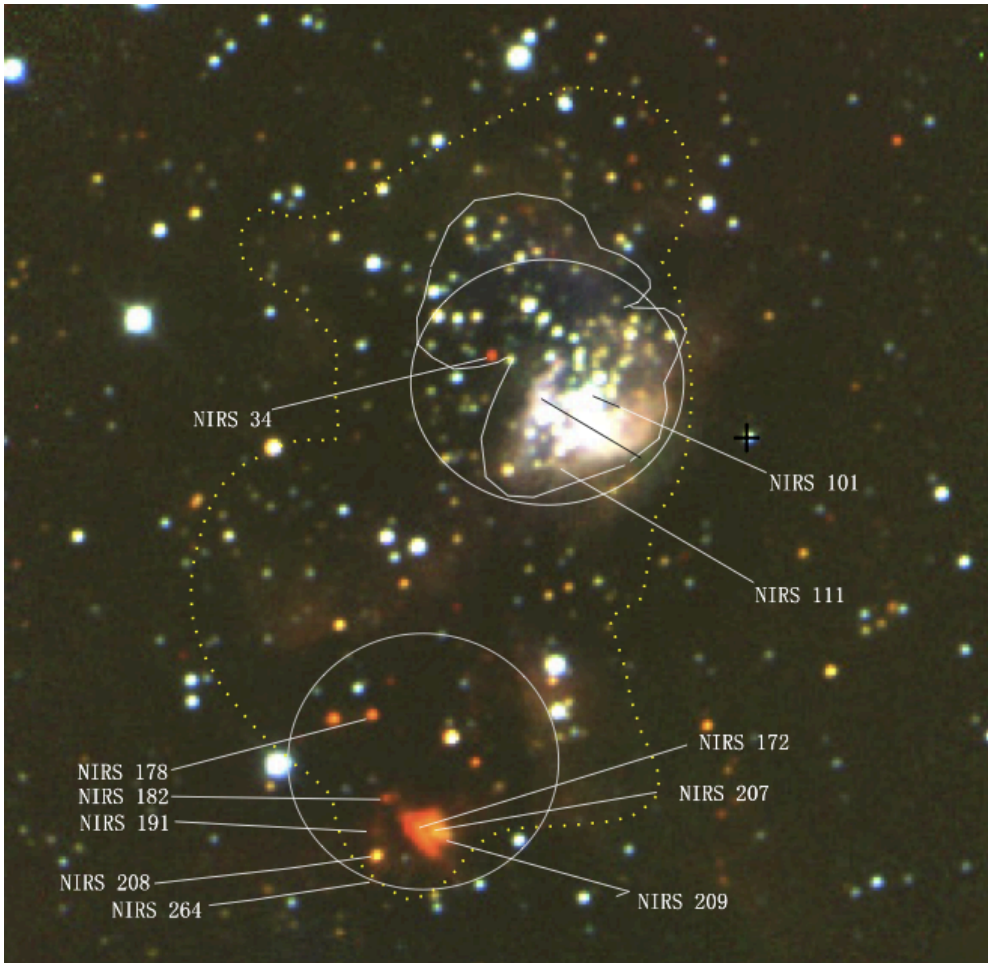

Figure 4.7 JHK' composite colour image of S152 in a $4.2' \times 4.2'$ field by Chen et al. (2009). The two circles identify the two clusters. The upper cluster associates with S152-C3 and the lower cluster is associated with S152-C4, CO clumps identified in our ^{12}CO(2-1) maps. The upper cluster which is covered by the H II region is more evolved while the lower cluster is embedded in an IR nebula and probably much younger.

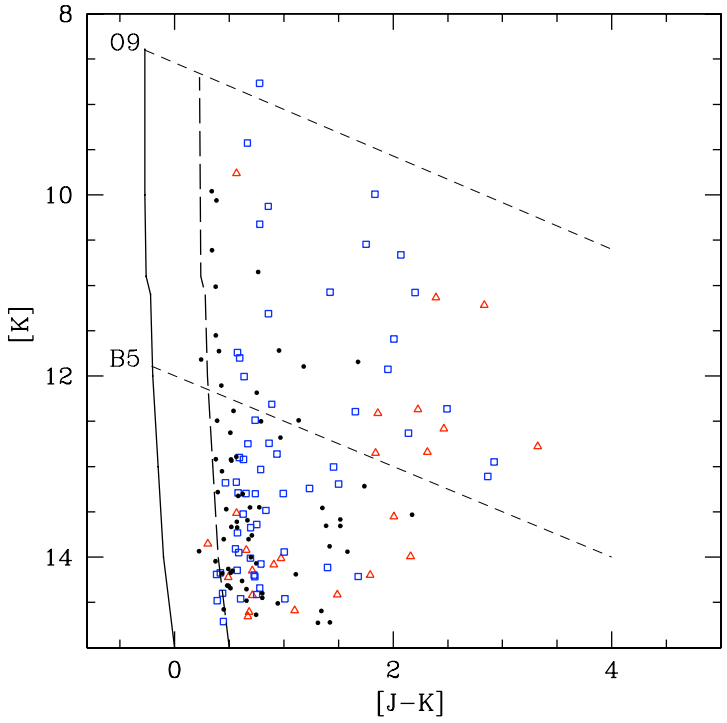

Figure 4.8 Colour-magnitude diagrams of the 2MASS sources toward S152. The symbols and reddening lines are the same as Fig. 4.3. Thirteen point sources (right side of the diagram) with IR excess form a new population of YSO candidates

4.5 175A / S175B

S175 is a small H II region. The associated molecular cloud has been studied in detail by Azimlu et al. (2009) (Chapter 2 of this thesis). Figures 4.9 and 4.10 present the CO contours super-imposed on 2MASS images for S175A, associated with the H II region and S175B, within the same molecular cloud but $\sim 20'$ farther. The most massive clumps in S175A (C6) with $T_{ex} = 47K$ and $N(H) = 243 \times 10^{20} cm^{-2}$ locates at the edges of the H II region. The star formation efficiency in this clump is lower ($\sim$ 2%) than the most turbulent clump, C1, in S175B ($\sim$ 6%) and less than the general star formation efficiency in molecular clouds. A proto-stellar outflow has been detected associated with S175B-C1 in our molecular cloud study (Chapter 2, Azimlu et al., in preparation). We have detected an extended object perpendicular to the outflow direction in 2MASS K_s band data which is presented in the enlarged rectangular in right panel in Figure 4.10. A higher resolution image is required to study the structure of this extended object.

We have selected a third off field to compare the stellar distribution within S175A and S175B. Figure 4.11 presents the colour-colour diagram for S175B (left panel) and the off field (right panel). We see almost the same number of objects with infrared colour excess in both S175B and off field and also in S175A (Figure 4.9 right panel). The main sequence stars and giants are more shifted along the reddening line than the off field. More reddening is

seen for sources detected within S175B which indicates more gas in this region, consistent with our findings in Chapter 2. We have detected five sources within S175B (including the proto-stellar core with outflow and 4 point sources close to it) which have been detected only in K_s band and are possibly young embedded stars.

Figure 4.12 shows the colour-magnitude diagram for S175A, S175B and the off field. S175A is partially widened along the reddening line compared to the off field, while S175B contains a new population of lower mass stars with high IR colour excess. Detecting these sources associated with S175B-C1 and detection of the proto-stellar outflow at the position of this clump indicates that star formation is in progress in this region but none of the YSO candidates are massive proto-stars. S175B is too far from the ionized gas to be affected. contrarily, we have found no stellar cluster, candidates for proto-stars, turbulent or dynamically active regions in S175A, the closest part of the molecular cloud to the S175 H II region. These all means that star formation has not been triggered by the H II region and star formation process in S175B is probable spontaneous.

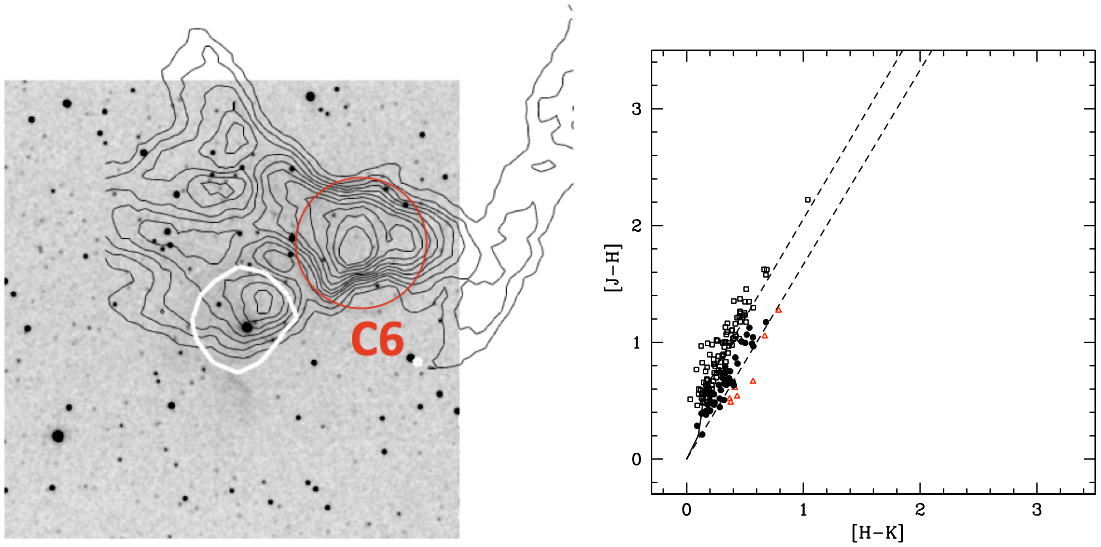

Figure 4.9 (left) Same as Figure 4.1 for S175A. No clustering or active star formation process has been detected in this region. (right) the colour-colour diagram for S175A.

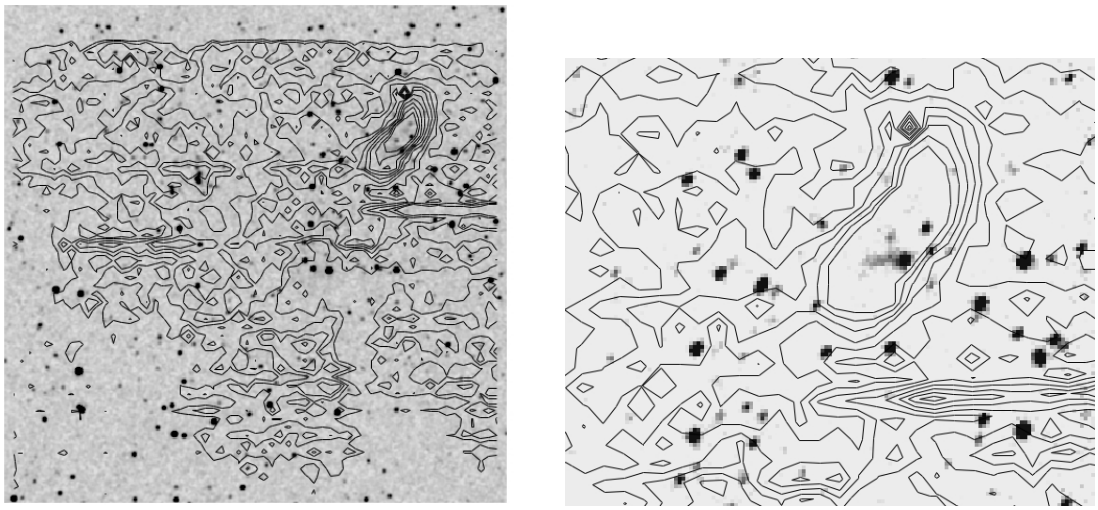

Figure 4.10 The ^{12}CO(2-1) contours overlaid on 2MASS K_s band image for S175B. An active star-forming region that has been detected in the top right corner of the map is enlarged in the right panel. An extended object has been detected within S175B-C1 at the position of a recently detected proto-stellar outflow and almost perpendicular to the outflow direction.

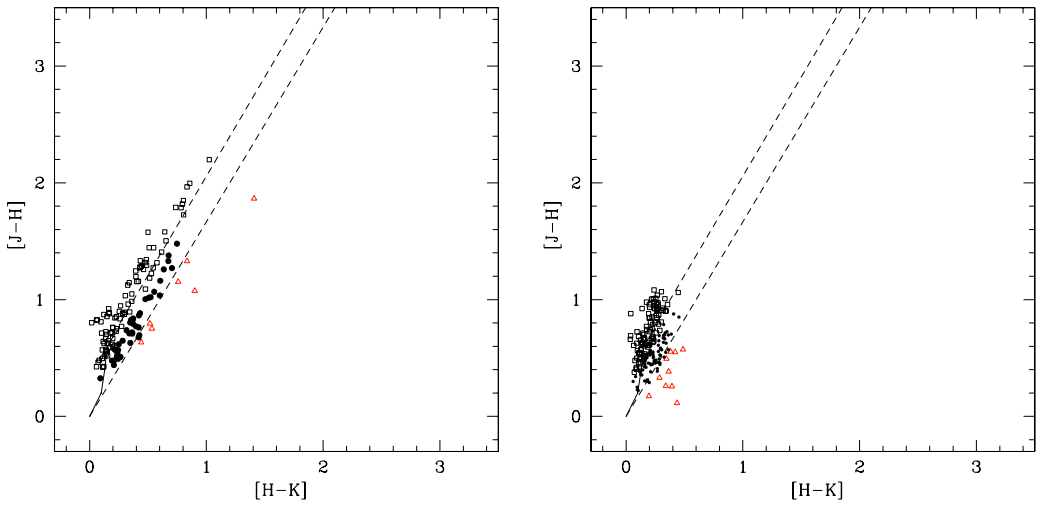

Figure 4.11 colour-colour diagrams for S175B (left) and a check off field (right). As was expected, the sources associated with the molecular gas have been shifted along the reddening lines.

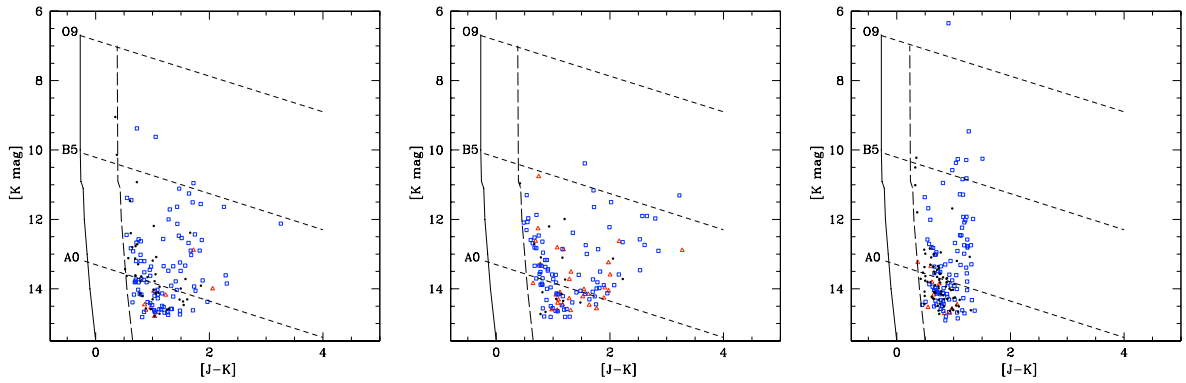

Figure 4.12 Colour-magnitude diagrams of the 2MASS sources toward S175A (left panel), S175B (middle) and off field (right panel). The symbols and reddening lines are the same as Fig. 4.3. All regions contain none or few massive stars. S175A sources are slightly reddened along the reddening lines compared to the off field, but it does not contain too many sources with IR colour excess. In contrast S175B contains lots of sources with red colour excess which form a new population of stars with high reddening. S175B is a good example of spontaneous low mass star forming region.

4.6 S192 / S193 / S194

The molecular gas in this region is associated with three H II regions. Figure 4.13 presents the ^{12}CO(2-1) contours overlaid on 2MASS K_s band image. The visible borders of three H II regions are shown by red curves. No clustering is seen in this region and probably most of the original cluster members have been evaporated and left the cluster. The central clump, S192-C6 which appears to be compressed by three H II regions has the higher temperature ($T_{ex} = 21$ K) and density (N(H)= 168×10^{20} cm^{-2}) in the cloud. It also has the largest line widths: $\Delta V_{12} = 3.45$ km s^{-1} and $\Delta V_{13} = 2.13$ km s^{-1}. The clump has a larger Virial mass compared to velocity integrated mass (M$_{vir}$ =300 $\pm$50 vs. M$_{int} = 22 \pm 7$) and is not gravitationally bound. The star formation efficiency is very high in this clump ($\sim$ 40%) and probably star formation has been triggered in this clump by the expansion of three H II regions.

A weak IR nebula is detected at S192-C6. Eight reddened objects appear associated with this nebula. The bright central source has the largest infrared excess in the colour-colour diagram. Figure 4.14 shows the colour-magnitude diagram for this region. Most of the 2MASS detected sources are main sequence or giants slightly reddened by a small extinction of $A_V \sim 3$ and just a few giants with larger extinctions up to $A_V \sim 15$. Only one source has been detected with high infrared excess which locates at the S192-C6. The cloud seems to be evolved and probably has lost most of its original gas, but the

central compressed high density gas with large external motion still favours a second generation star formation; however the clump mass is not high enough to produce a rich cluster or massive stars.

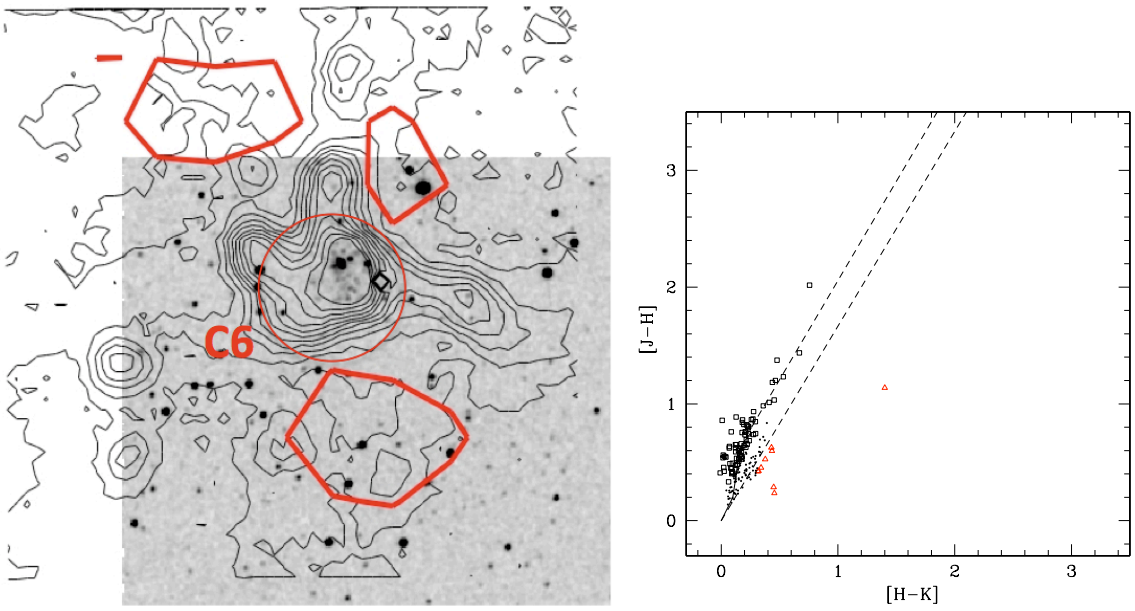

Figure 4.13 The molecular cloud associated with S192/S193/S194 H II regions is an evolved star-forming environ. The red curves present the visible borders of three H II region. The central compressed gas has high temperature and density and contains a few reddened objects. Despite the high density, external pressure from expanding ionized gas and large internal motions, the clump does not contain enough mass to produce a reach stellar cluster or massive stars.

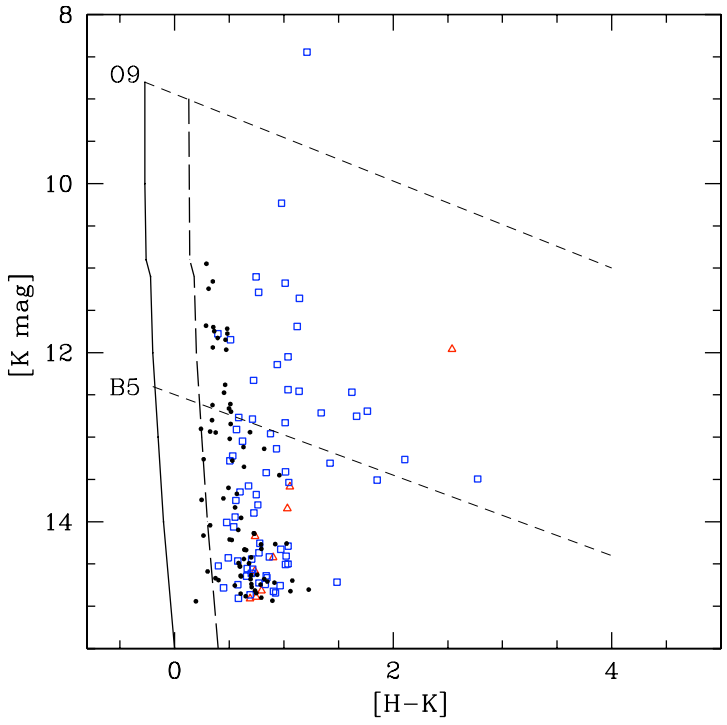

Figure 4.14 Colour-magnitude diagrams of the 2MASS sources toward S192/S193/S194. The symbols and reddening lines are the same as Fig. 4.3.

4.7 S196

S196 is an evolved H II region, similar to S192. Figure 4.15 shows a small amount of the molecular gas left around the expanded H II region. No exciting star has been identified for this bubble of ionized gas. It seems that the expansion of the H II region has swept the molecular gas to an area larger than our map and we need to extend the ^{12}CO(2-1) map to cover more of the molecular gas associated with this H II region. The only dense part of the cloud is located at the south-east corner of the mapped region (S196-C1 and S196-C2). We do not have ^{13}CO(2-1) data for these two clumps. They are not very hot ($T_{ex} = 15.5K$ and 16.5 K for C1 and C2 respectively) but contain more than 80% of the total mapped molecular gas but the star formation efficiency is not very high ($\sim$ 3%). The 2MASS sources with the highest infrared colour excess from colour-colour diagram lie within this region. The colour-magnitude diagram, Figure **??** also shows mostly main sequence foreground/background stars with an average extinction of $A_V \sim 3 - 4$.

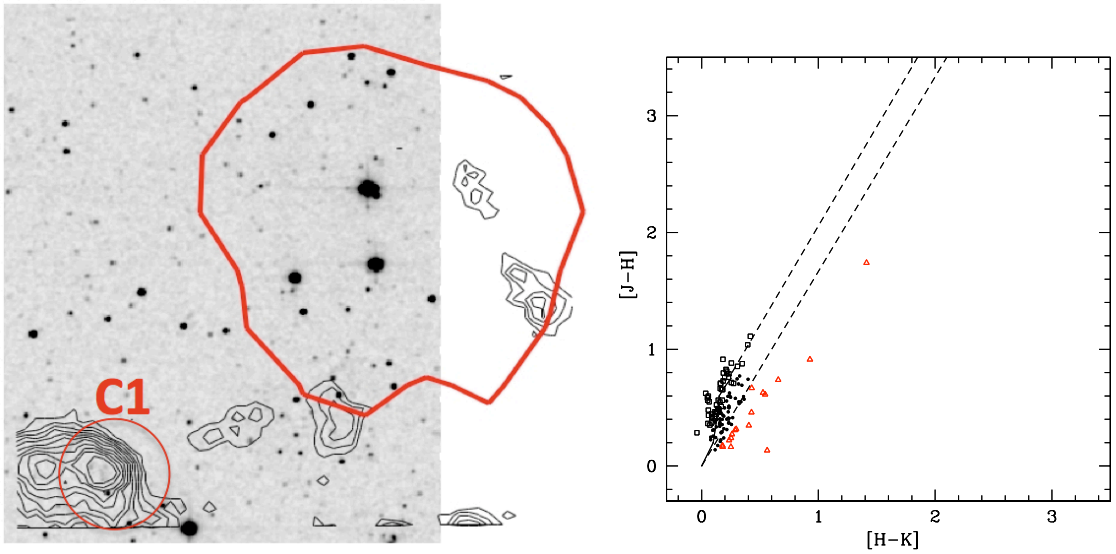

Figure 4.15 same as Figure 4.13 for S196. The H II region has swept most of the molecular gas to an area larger than the mapped region. No exciting star has been identified for this region. The original cluster has probably evolved and evaporated.

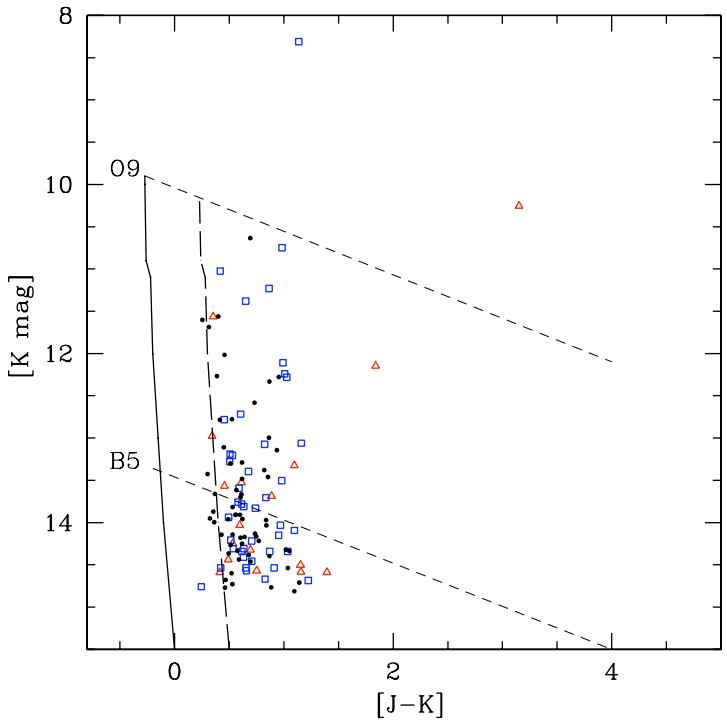

Figure 4.16 Colour-magnitude diagrams of the 2MASS sources toward S196. The symbols and reddening lines are the same as Fig. 4.3.

4.8 S212

S212 is a large H II region with a diameter of 10.2 pc. It has been excited by an O6 star which belongs to a stellar cluster. Figure 4.17 presents the ^{12}CO(2-1) map super-imposed on the 2MASS K_s band image. The molecular gas has a filamentary structure, only half of which has been mapped by us (compared to a more complete map by Deharveng et al. 2008). The H II region is also larger than the mapped area and the visible edges of the ionized gas is shown with the thick white curve. The exciting cluster is located at the west (right) side of the map. The molecular gas at the position of the H II region has been swept and collected in dense fragmented shells. These hot clumps (S212-C1 to C4) with high gas density and large line widths ($T_{ex} > 25$ K and $\Delta V_{12} > 3$ km $^{-1}$), are good candidates of sequential star formation. S212-C3 has the highest mass and temperature ($\approx 1030 M_{\odot}$ and $T_{ex} = 38$ K) however it is relatively small clump (2 pc in diameter). The star formation efficiency in this clump is about 8%, consistent with general efficiency of star formation in molecular clouds.

Deharveng et al. (2008) made a detailed study including CFHT observations in JHK broad band filters. Figure 4.18 presents the result of their near-IR observations. They have identified a YSO located at the periphery of the H II region. Their colour-magnitude diagram shows that the whole region is affected by a visual extinction of about 3 mag. They have observed red stars

all over the cluster but the density of red stars is higher at the direction of S212-C1 and S212-C2 in our study. They mark sources with infrared colour excess in colour-colour diagrams which are good candidates for YSOs. S212 is the farthest source in our sample at a distance of 7.1 K pc. The $A_V \sim 3$ is very low for such a large distance, therefore, Deharveng et al. (2008) conclude that there is little local dust in front of the exciting cluster. Our colour-colour and colour-magnitude diagrams (Figures 4.17 and 4.19) for 2MASS sources are not as deep as their CFHT study, but agree with their findings. We detect 6 point source with high IR colour excess which could be YSOs candidates.

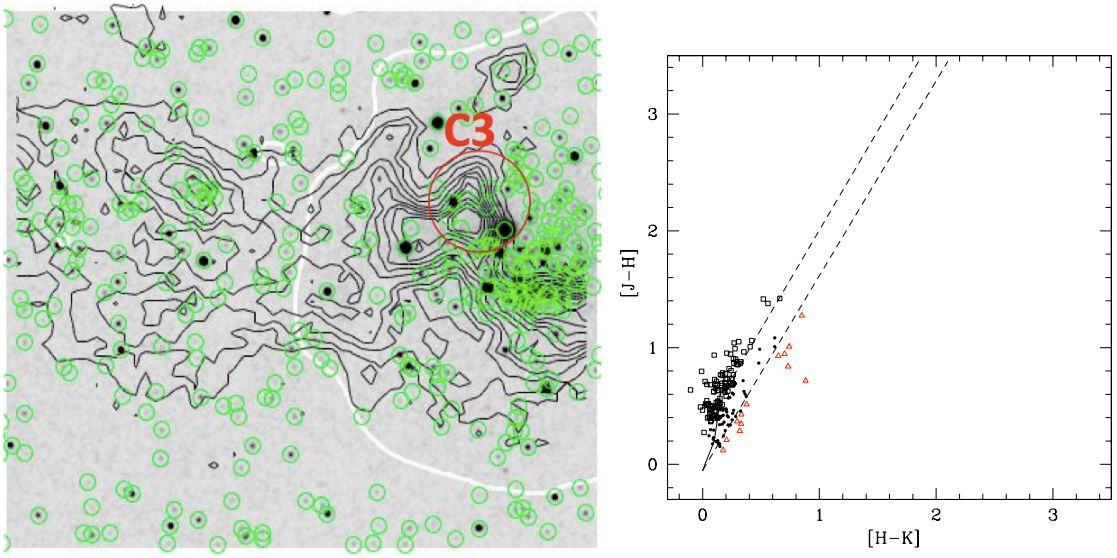

Figure 4.17 same plot as Figure 4.1 for S212. The H II region has been excited by a cluster containing an O6 star. The 2MASS data colour-colour diagram shows some sources with infrared colour excess that could be YSOs, but in total we do not see a high reddening for the whole cluster.

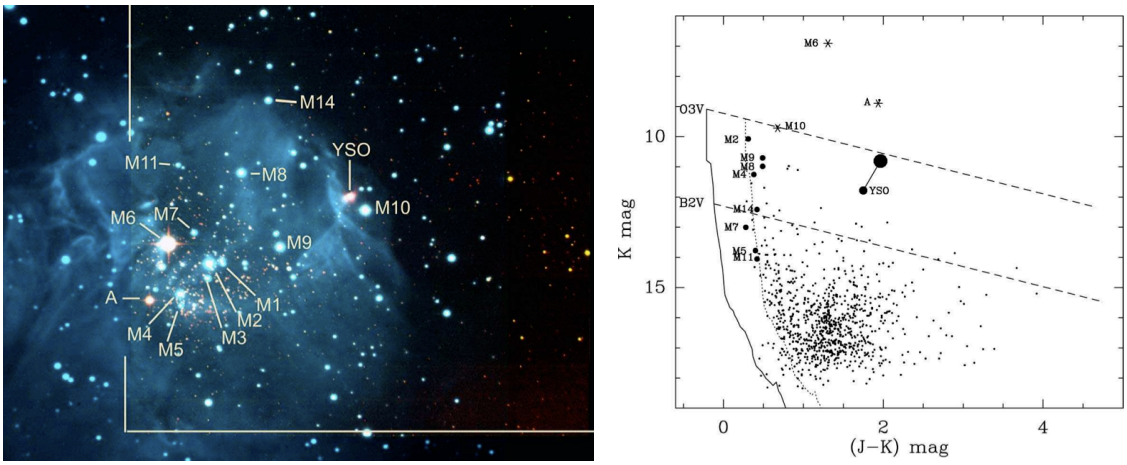

Figure 4.18 The exciting cluster of S212 with some identified sources. The colour-magnitude diagram shows a visible extinction of 3 mag for the whole field which is small for an object at the distance of S212 and probably caused only by the ISM. Thus the local dust is very little and has a small role in reddening (both pictures from Deharveng et al. 2008).

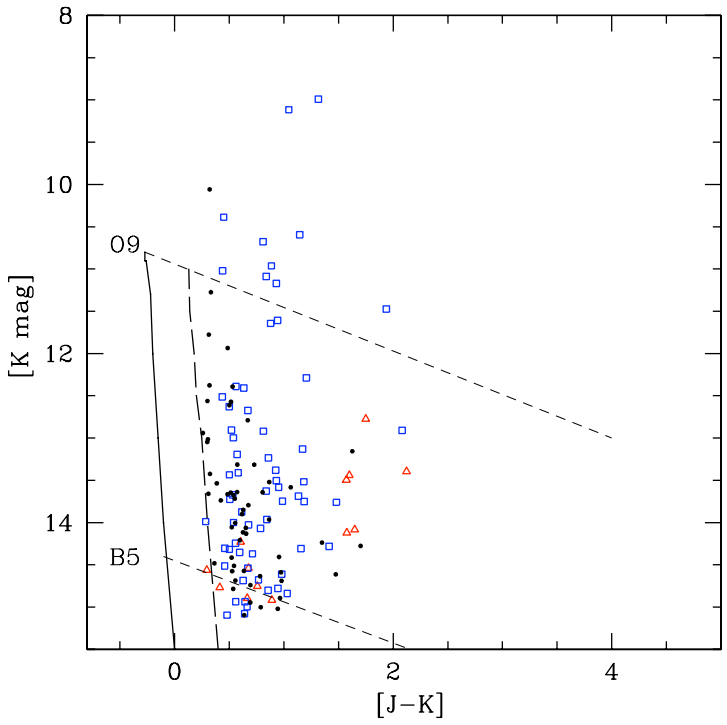

Figure 4.19 Colour-magnitude diagrams of the 2MASS sources toward S196. The symbols and reddening lines are the same as Fig. 4.3.

4.9 S288

S288 is a small H II region excited by a B1 star located in a stellar cluster. Similar to S212 the molecular gas associated with this H II region has a filamentary structure with only four identified clumps. The two central dense clumps, S288-C1 and S288-C2, seems to be two sides of a twisted filament with excitation temperatures of 22.5 K and 24.6 K respectively. They also have large ^{12}CO line widths of 3.84 and 3.44 km s^{-1}. We have no ^{13}CO data for this region. Star formation efficiency is moderate for these clumps ($\sim 6\%$) in agreement with general star formation efficiency in molecular clouds.

At a moderate distance of 3 kpc, the visible extinction due to the ISM is not very large and about $A_V = 2$ mag (colour-magnitude diagram, Figure 4.21). The colour-colour diagram (Figure 4.20) also does not show high reddening for the whole region indicating that similar to S212, there is little dust associated with the cluster and the whole region. Only one 2MASS source has been detected with high reddening which is located at the centre of the cluster and probably behind the dense central twisted part of the filament. The ^{12}CO(2-1) emission line at the centre of the cloud is double-peaked and probably self-absorbed. More observations in thinner emission lines such as ^{13}CO and C^{18}O will be needed to estimate the physical properties of the molecular gas (density, excitation temperature, mass).

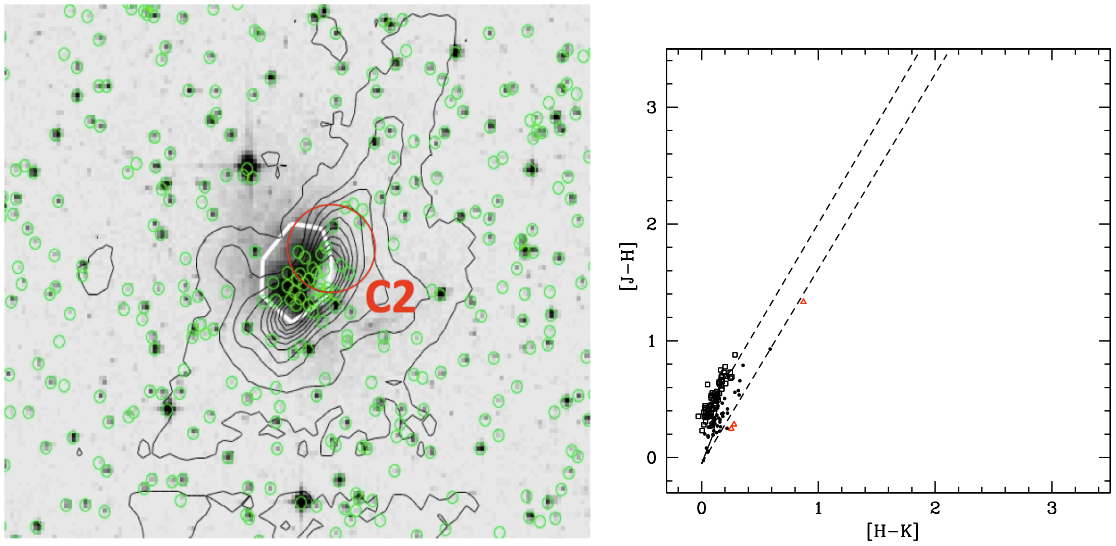

Figure 4.20 same as Figure 4.1 for S288. The exciting star belongs to a stellar cluster located at the dense central part of the filamentary structure of the molecular gas. The colour-colour diagram does not show a high extinction. The only high reddened 2MASS source in this diagram lies at the direction of the central dense clump which has signatures of self-absorption in ^{12}CO emission lines.

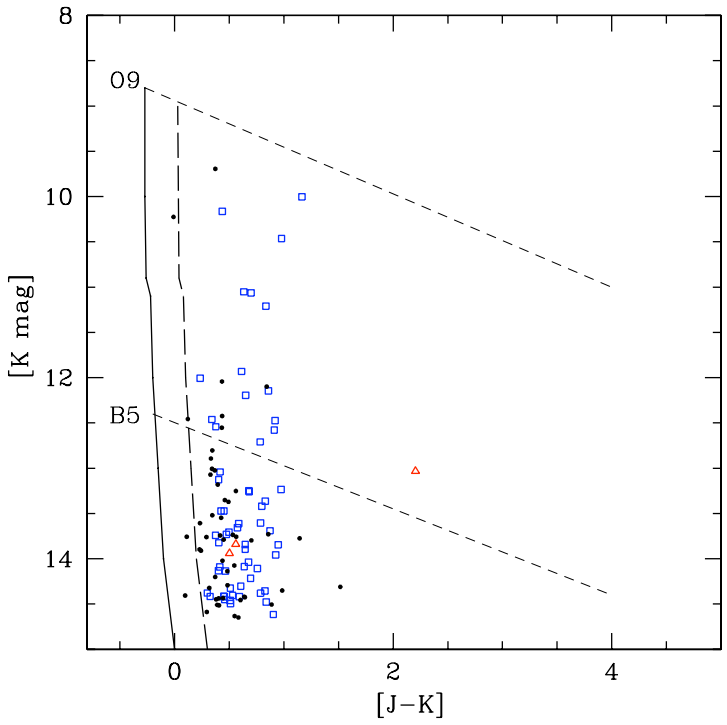

Figure 4.21 Colour-magnitude diagrams of the 2MASS sources toward S288. The symbols and reddening lines are the same as Fig. 4.3.

4.10 S305

Figure 4.22 presents the ^{12}CO(2-1) contours super-imposed on 2MASS K_s band images. The H II region covers a stellar cluster which probably contains the O9.5 exciting star. The molecular gas has partially collected at the edges of the ionized has and collapsed into dense clumps. The dense clump located at the west (right) edge of the mapped region, S305-C7, is the hottest clump detected in our entire sample of 10 H II regions with a T_{ex} = 46.4. Except for the outflow detected in S175B, S305-C7 is the only clump with high density that we have detected CS(5-4) at the position of highest ^{12}CO peak within the clump. Detection of CS(5-4) indicates a high central gas density of $2.8\times10^{7} cm^{-3}$ (Evans 1999). This clump with the total velocity integrated mass of 470±240 $M_{\odot}$, is a likely candidate for massive star formation. A small sub-cluster is identified at the direction of this clump in the 2MASS image, but it is not determined if the cluster is associated with the S305-C7.

The star formation efficiency is moderate ($\sim$ 6%) and probably underestimated as most of the newborn stars are embedded within the dense gas and not detected in 2MASS. S305-C2, the large central clump, is another candidate for a massive star-forming region. Located at the periphery of the H II region and probably compressed by the expansion of ionized gas, S305-C2 has a temperature of T_{ex} = 28 K. S305-C2 is the largest and the most massive clump in the region with $M_{int} = 760\pm390$ $M_{\odot}$ which is almost twice the $M_{vir} = 320\pm87 M_{\odot}$.

Although the clump has a large line width of $\Delta V_{12} = 3.42$ km s^{-1}, it is gravitationally bound. We have detected 26 sources with infrared colour excess in colour-colour diagram, Figure 4.23. Colour-magnitude diagram shows the main sequence and with a moderate extinction of $A_V \sim 4 - 5$ mag but interestingly we notice a second population of giants and sources with IR colour excess in Figure 4.23. Similar to S104, these highly extincted giants and red sources are good candidates of new born stars and YSOs peobably embedded within high density gas clumps.

The reddening is high within the field, indicating high density dust in the region. Most of the detected sources with red colour excess are in the direction of dense clumps.

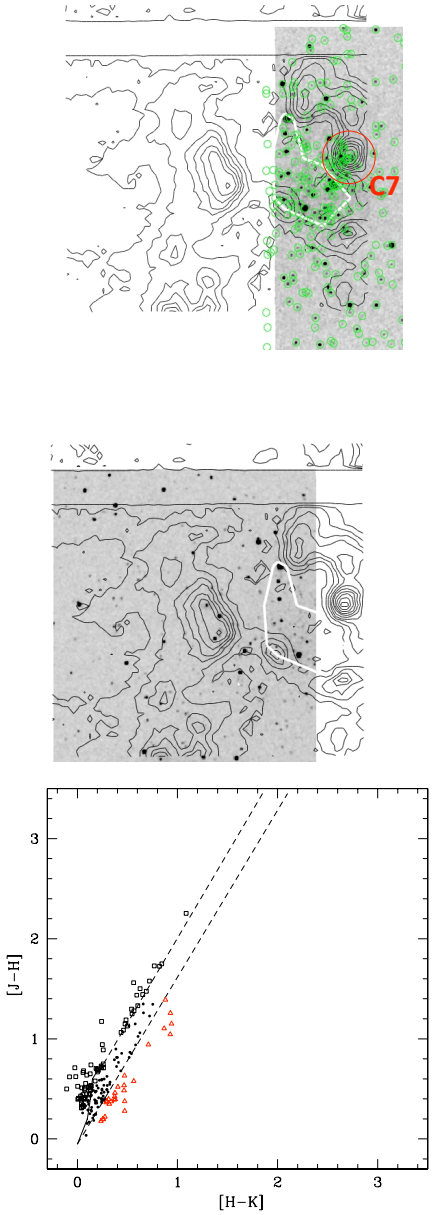

Figure 4.22 Same as previous Figures for S305. The H II region lies over a stellar cluster. The colour-colour diagram shows a high reddening in the whole field with 26 sources with red colour excess.

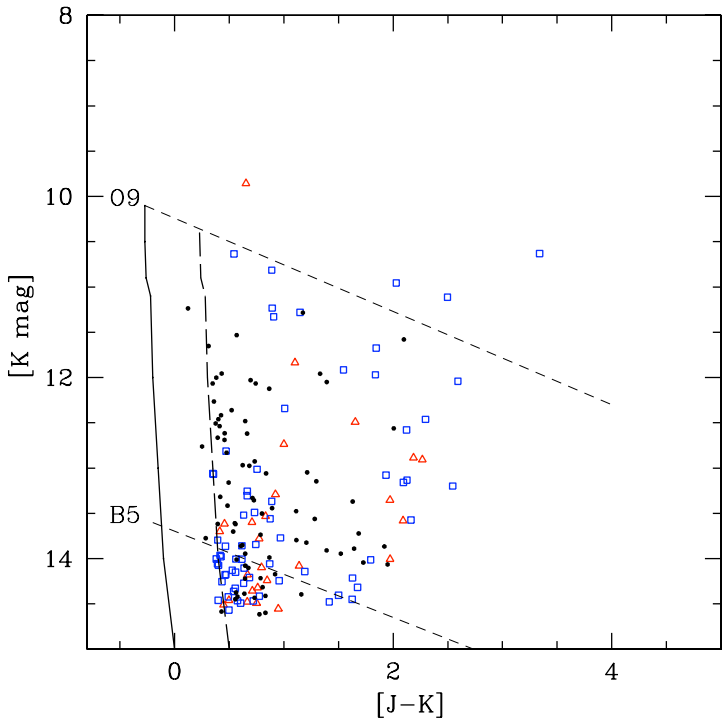

Figure 4.23 Colour-magnitude diagrams of the 2MASS sources toward S305. The symbols and reddening lines are the same as Fig. 4.3. similar to S104, a second population of giants and point sources with large IR colour excess is noticeable in this diagram. these are objects could be candidates for newborn massive stars or YSOs.

4.11 S307

Figure 4.24 presents the ^{12}CO(2-1) contours super-imposed on 2MASS K_s band images. The O9 exciting star belongs to a stellar cluster identified in 2MASS images at the same position as the H II region. The cluster is probably the result of a triggered star formation process as discussed in Appendix A. A second smaller cluster is identified in the south-east part of the cloud which is distant from the H II region and unlikely to be affected by the ionized gas. Different physical conditions within that dense clump may have caused a different stellar population. These two clusters are an interesting pair of objects to study in details in future. Deep and high resolution observation is required to study the faint embedded young stellar objects within this small part of the cloud.

Contrary to our expectations, S307-C4 which is distant from the H II region, has the highest temperature (T_{ex}= 50 K) and column density (N(H) = 513 $\times 10^{20}$ cm s^{-2}), the largest line width (ΔV_{12} = 3.35 km s$-$1) and the largest mass ($M_{int} = 250 \pm 108$ M$_\odot$). M_{int} is close to the $M_{vir} = 277 \pm 63$ M$_\odot$, therefore the clump is in Virial equilibrium. This physical conditions are suited for cluster formation (Lada et al. 1997) and massive star formation (McKee & Tan 2003). The star formation efficiency in this clump is about 12% which is consistent with the star formation efficiency in molecular clouds but smaller than the star formation efficiency in S307-C2 $\sim$ 27%, the central clump which contains the exciting star and a stellar cluster.

In a recent study of S307, Roman-Lopes (2009) confirmed the presence of an O9-O9.5V exciting star but they calculated a new heliocentric distance of 3.2±0.5 kpc for it. They estimated the dynamical age of the H II region to be 1.6×10^6 yrs. They also observed the cluster associated with the H II region in near-IR JHK bands and found that the stellar population is very young and a large fraction of YSO candidates with large excess emission in 2μm, are accreting pre-main sequence proto-stars. They estimated a mean age of 2.5 Myr for the cluster.

Our colour-colour and colour-magnitude diagram for 2MASS sources (Figures 4.24 and 4.25) are not as deep as Roman-Lopez (2009) but in agreement with their findings. We have detected 24 sources with IR colour excess 5 of which are also high extincted. The average extinction of the visible magnitude, A_V, is about 3 mag which is not very large but some giants and red sources with extinctions as large as 15 are noticeable in Figure 4.25. These objects are probably newborn embedded stars or YSOs.

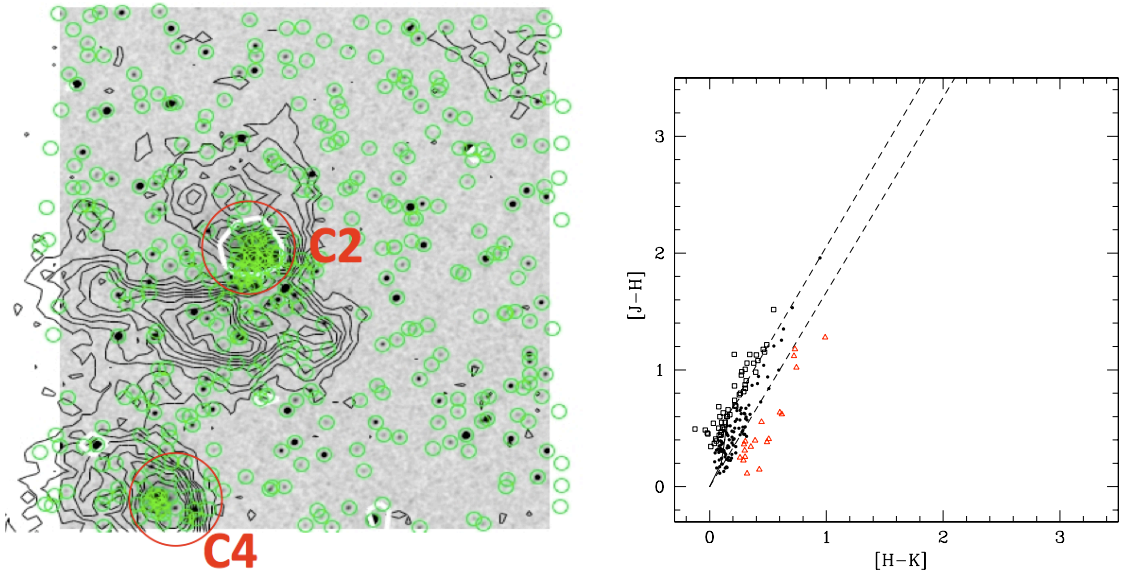

Figure 4.24 same as Figure 4.1 for S307. The exciting star locates at a young stellar cluster with an estimated age of 2.5 Myrs. The associated cluster and molecular gas are likely to be influenced by the exciting star. A second cluster is identified associated with the compact separated part of the cloud at East-Sout corner of the filed. The two parts of the molecular cloud have different internal dynamics and physical conditions and probably different stellar populations.

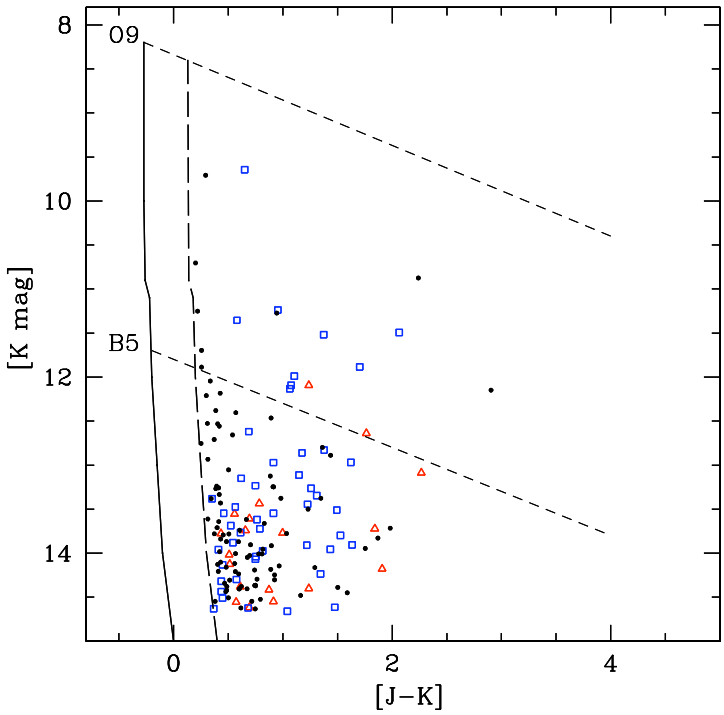

Figure 4.25 Colour-magnitude diagrams of the 2MASS sources toward S307. The symbols and reddening lines are the same as Fig. 4.3. Similar to S104, a second population of giants and point sources with large IR colour excess is noticeable in this diagram. these are objects could be candidates for newborn massive stars or YSOs.

4.12 Discussion and summary

We have studied the stellar population within and around our sample of H II regions using 2MASS JHK_s band images. Two types of clusters were identified in this study: the open clusters that mostly have main sequence stars and contain the exciting star and young embedded clusters whose formation is likely triggered by the expansion of the H II region.

The colour-colour and colour-magnitude diagrams show different stellar population within our sample. For example S104, S175B and S307 have noticeably a second population of young and highly extincted stars. Interestingly most of the young stars within S104 and S305 which are adjacent to the H II region are giants but the young population within S175B which is too distant from the H II region (10 times farther than the Stromgren radius) contains relatively more intermediate and low mass stars. We may conclude that the *massive star formation is favoured in molecular clouds nearby the H II regions* but it is not clear yet if this is a result of the initial conditions that have formed the first massive star in the first place or an effect of the previously formed massive star and the expanding H II region. S175B is a part of the same cloud that has produced a B star which excites S175 H II region and probably have the same initial conditions, but it is not a massive star forming site. We need to study more regions within the same cloud but far from the H II regions nearby other sources to examine that result.

The fact that half of the H II regions in our sample have the same position as a cluster that appears to host the exciting star is consistent with previous suggestions that massive stars are mostly formed within clusters. We also found that the hottest clumps with the high density and large line widths are generally very close to the H II regions. Most of these dense clumps are gravitationally bound and likely candidates for massive star formation. The star formation efficiency is very high in S192-S194 and S104. S104 seems to have star formation in process with high rate and efficiency but S192-94 is an evolved region and the high stellar mass to gas mass ratio is probably because most of the original gas within the cloud has evaporated.

Chapter 5

Summary and Conclusions

The main goal of this thesis was to gain an understanding of the effects of massive stars on the molecular clouds with which they are associated and to investigate how the star formation has been influenced. We studied the characteristics of the molecular gas by making ^{12}CO(2-1) maps of the clouds around H II regions excited by massive stars. We used these maps to probe out the structure of each cloud and to identify the dense clumps within. In particular we were interested in the clumps at the peripheries of the ionization fronts of the H II regions. Pointed observations in ^{13}CO(2-1) and CS(5-4) were made at the identified ^{12}CO(2-1) peaks within each clump. These higher density gas traces provide us with information on the properties of the dense cores within the clumps where star formation takes place.

We presented our CO maps in Appendix A and discussed special features

within each map. For example, the molecular gas is swept up by the ionization fronts and collected in shells in four sources in our sample: S104, S192/193, S212 and S305. The clumps formed within these shells are generally hotter and have higher density and larger line widths. We also found candidates for further massive star formation within the clouds.

In Chapter 2 we compare two mapped regions within the same cloud associated with S175. S175A is adjacent to the H II region and likely affected by the ionized gas while S175B is too distant to be influenced.

Chapter 3 presents the derived parameters for the entire sample. In this chapter we investigated how the physical properties of the identified clumps are related to each other. We also studied how the physical characteristics of the clumps change with distance from the ionization fronts of the H II region.

Finally, we looked at the stellar population within each region using JHK near-IR images from 2MASS survey and investigated how the stellar distribution is related to the cloud structure and the gas properties. We expected to see that star formation has been triggered at the edges of the expanding shells around the H II regions and did find evidence of young stellar objects in some of the dense collapsing clumps within the fragmented shells. In the following we summarize the results of our investigation.

- Massive star formation is favoured in molecular clouds nearby the H II regions at least in three active star forming regions in our sample. THe

only star forming region which is far from the massive star and the H II region contains only intermediate and low mass YSO candidates or stars. It is not clear yet if this is a result of the initial conditions that formed the first exciting massive star within the cloud or a feedback of the H II region and massive star itself that provides the environmental requirement to produce massive proto-stars.

- Our sources mapped in molecular gas can be divided into two categories, the sources which show a size-line width power law relation, called "type I" and the rest which do not have this relation, called "type II". The power law indices derived of the best fitted lines to examine this relation are generally larger than the previous studies. As we later conclude that the internal dynamics of the gas beyond the collected shells around the massive star is not much affected by the expanding H II region, we may conclude that this is an initial characteristic of massive star forming regions.

- In half of the sources in our sample molecular gas appears to be collected by the expanding H II region and collapsed in dense clumps within shells around the ionized gas in half of the sources in our sample. These clumps have been warmed up by the radiation from the exciting star and the compression by the ionized gas. The molecular gas in the shells is more fragmented and the clumps within the shells have higher density and line widths in general.

- Three different mass estimation methods were used in this study. The Virial mass which varies with $(\Delta V)^2$ is highly dependent on the internal dynamics of the cloud and generally over estimates the mass. Velocity integrated mass, which is dependent on ΔV, also relies on the cloud dynamics. M_{LTE} is calculated based on the column density and is independent of the internal dynamics of the cloud, but the LTE assumption is not appropriate for all star-forming cores. In our study M_{vir} is the largest mass for low mass clumps but tends to equal values with M_{int} and M_{LTE} for larger masses and becomes approximately equal to M_{int} at 100 $M_{\odot}$. The larger clumps are mostly the most distant ones in which we cannot resolve smaller structures. Therefore we examined the mass relations only for the distant sources to reduce the resolution effect, but no significant differences between different regions at different distances were observed. This suggests that the larger clouds might be in Virial equilibrium while the smaller fragments within them are not.

- The star formation efficiency is not very high except for S104 and S192-94. That might be a result of the incompleteness of the 2MASS data which is not deep enough and does not record the faint stars embedded within dense gas. S104 is an active star forming region and has a SFE of 35% while S192-S194 region is an evolved molecular cloud and it has probably lost most of the initial gas and that's the reason of a high stellar mass to gas ratio (40%) for this region.

- Clumps which are closer to the H II region have higher temperatures, although we can measure only the projected distance to the ionization fronts, which could be smaller than the true value. Therefore we compared our results with a Monte Carlo simulator of the clumps temperature at random distances from a heating source and found good consistency between the simulation and observations. We also investigated how the line width of the peaks at each clump varies with distance from the H II region and found no relation. However it appears that the clumps within the shells compressed by expanding ionized gas have generally larger line widths, although the internal dynamics of the cloud beyond the compressed shells is not much affected by the H II region.

- The exciting star of six H II regions in our sample belongs to a stellar cluster, confirming the previous theoretical models and observational studies that massive stars form within clusters in GMCs. The clusters are not young and most of their members are main sequence stars with still a few members having infrared colour excess that are probably pre-main sequence or young stellar objects.

- Within our sample, the exciting star or the cluster that contains the exciting star is generally associated with the most massive, hot clump identified in the molecular cloud which has high density and large line width. In some cases the ionized gas and the dense molecular gas clumps overlap in position which indicates one is in front of the other. Despite

the large internal motions, most of these clumps have enough mass to be gravitationally bound.

- Star formation appears to be triggered by the expansion of ionized gas in at least half of the sources in our sample. The young embedded clusters have been detected in the near-IR. They are located at the edges of the ionized gas front and associated with dense clumps within collected shells of molecular gas around the H II regions in S104 and S152. Some other dense clumps (for example S305-C7) compressed and warmed by the H II region are likely sites to form further massive stars.

- We have detected a proto-stellar outflow in a star-forming region within S175B. We have identified at least 5 very red objects detected only in K_s band in this region. One of these sources is an extended object associated with the outflow and almost perpendicular to the outflow alignment. The nature of this object is not identified due to poor resolution.

5.1 Future Work

We have recently observed 5 sources within our sample in deep near-IR images using CFHT WIRCAM to K_s magnitude of 20. Using these data we can identify the young embedded clusters, whose formation is probably triggered by H II regions, even if they are not very young (older than 10 Myrs) and highly extincted ($A_V > 20$ mag). We already have detected such stellar population in

raw data and so many other features in gas components in IR. Study of these population with our deep data may examine the results of this thesis that the number of massive YSOs or newborn stars is larger in association with H II regions. We will be also able to derive the IMF for detected young clusters to study if it has been affected by the environmental conditions or if there is a a cut off for low-mass or high mass ends.

We have identified hot, dense, massive clumps which are suited for massive star formation. We will look for candidates of forming massive stars within these clumps. We have started pointed observations in $C^{18}O$(2-1) at the peak position of ^{12}CO(2-1) within each clump which has a ^{12}CO(2-1) antenna temperature larger than 20 K. With this data set we can determine the density and other physical properties of deep embedded cores where the star formation actually occurs. Combining this information with the data from identified star-forming regions in the near-IR observation we will search for a better understanding of the star formation process and massive star formation in particular.

APPENDICES

Appendix A

An Overview of the Selected Sources

A.1 S104

S104 is the largest source in our sample with a diameter of 7′, and it is excited by an O6V star. Figure A.1 (right) shows the $9' \times 9'$ ^{12}CO(2-1) map of S104 integrated between -5 and 10 km s^{-1}. Double peaked line profiles like the one presented in the Figure A.1 show that the gas is expanding with a velocity of $\sim$ 3 km s^{-1}. The small picture at bottom left shows the same field from the Digital Sky Survey (DSS) red image and shows the ionized gas. The molecular gas has been swept by the ionization fronts and collected in shells around the ionized sphere. These dense shells have fragmented into several clumps which are likely to collapse and form proto-stars. S104 is a perfect example for the "Collect & Collapse" model, first presented by Elmegreen & Lada (1977).

S104 is a good example of a triggered star-forming region. The number of dense clumps that we have detected within the collected shells is more than twice what is seen in any similar area in other mapped regions within our sample. S104-C4, noted in the right hand picture by a red ellipse, is the hottest clump in our map with a T_{ex}=36 K. It also has the highest column density (N(H)$\sim$ 334 $\times$ 10^{20} cm^{-2}). High temperature and density provide suitable conditions for massive star formation.

Deharveng et al. (2003) studied the gas and dust component of the cloud associated with the ionized gas in S104 and found that a complete ring of dust emission surrounds the ionized gas. They detected a dense object at the position of S104-C4. Their near-IR observations at CFHT (Figure 4.2) show that a young cluster is deeply embedded within this clump (Deharveng et al. 2003). The cluster is associated with an Ultra Compact (UC) H II region, therefore it should contain a massive young star.

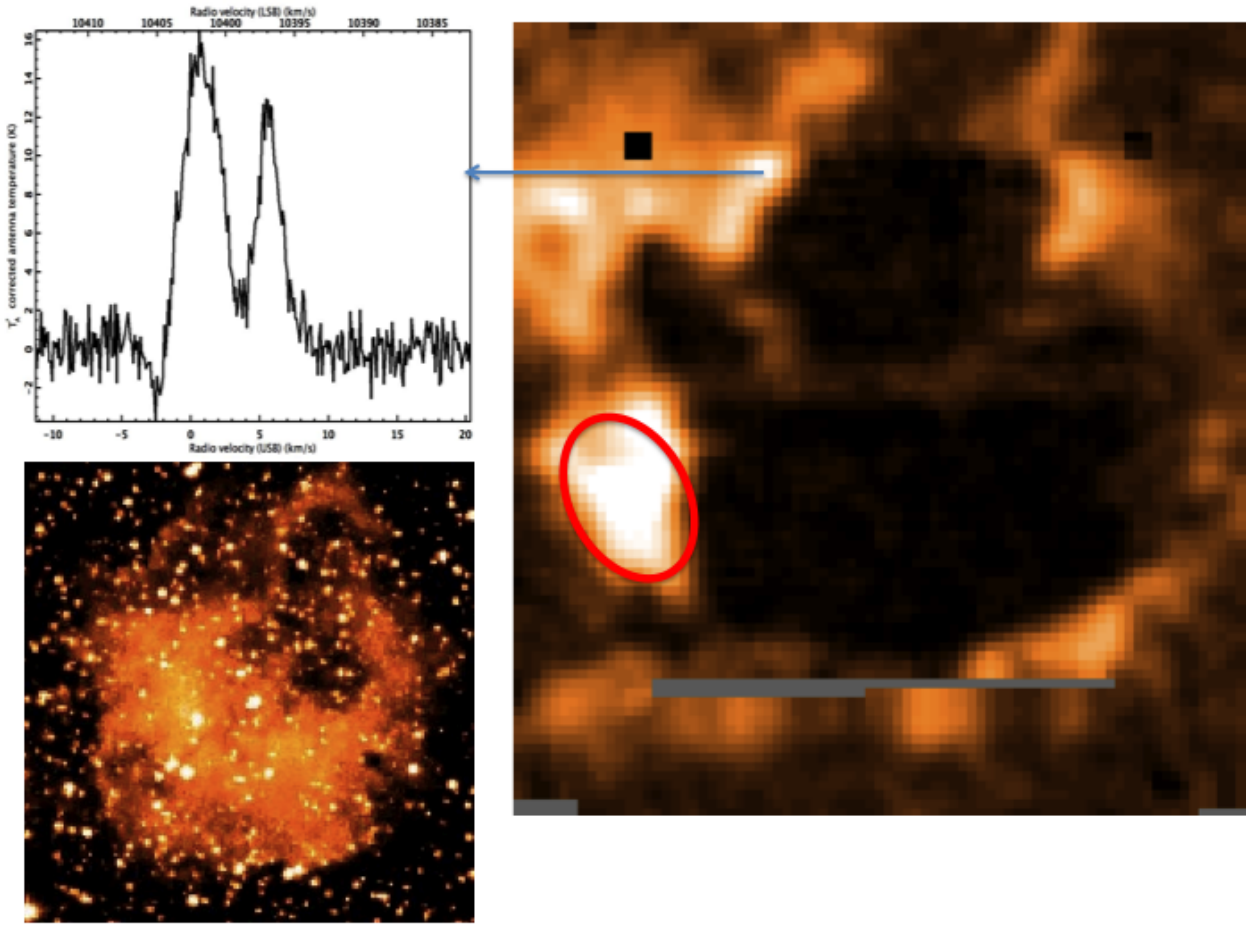

Figure A.1 : (right) $9' \times 9'$ map of S104 in ^{12}CO(2-1) . The line profile shows the expansion of the gas through red-shifted and blue-shifted emission. The bottom left image shows the same $9' \times 9'$ area from Digital Sky Survey-2 red filter. The molecular gas collected in shells at the front edges of the expanding ionized gas.

A.2 S148/S149

The molecular gas in our ^{12}CO(2-1) map (integrated between -45 and -60 km s^{-1}) covers two H II regions: S148 and S149 (Figure A.2). S147 is another component of this star-forming region which lies on south-east (bottom left in our map) but out of the field. S148 is excited by an O8V star within a cluster identified in 2MASS near-IR data (see chapter 4). S149 is smaller and excited by a B0V star (Caplan et al. 2000). S148-C5, at the same position as S148 (probably in front of the H II region) has the highest temperature and column density within our map (T_{ex} = 29 K and N(H)$\sim 290 \times 10^{20}$ cm^{-2}). This region had been studied by Pismis & Mampaso (1991) and they found it are very dusty young region with active star formation. They also calculated the star formation efficiency to be 0.08, close to the derived value of 0.1 by Hunter et al. (1990).

The identified clumps at the south-east part of the field have broadened line width and self-absorbed. These two clumps are probably affected by S147 which is out of our field but close to these two clumps. The wide line width of $\Delta V_{12} = 6.75$ km s^{-1} might be caused by multiple cores along the line of sight or signatures of an outflow. As this region is well known as an active star-forming region, it is probable we will be able to find outflows from young proto-stars associated with dense clumps within the cloud.

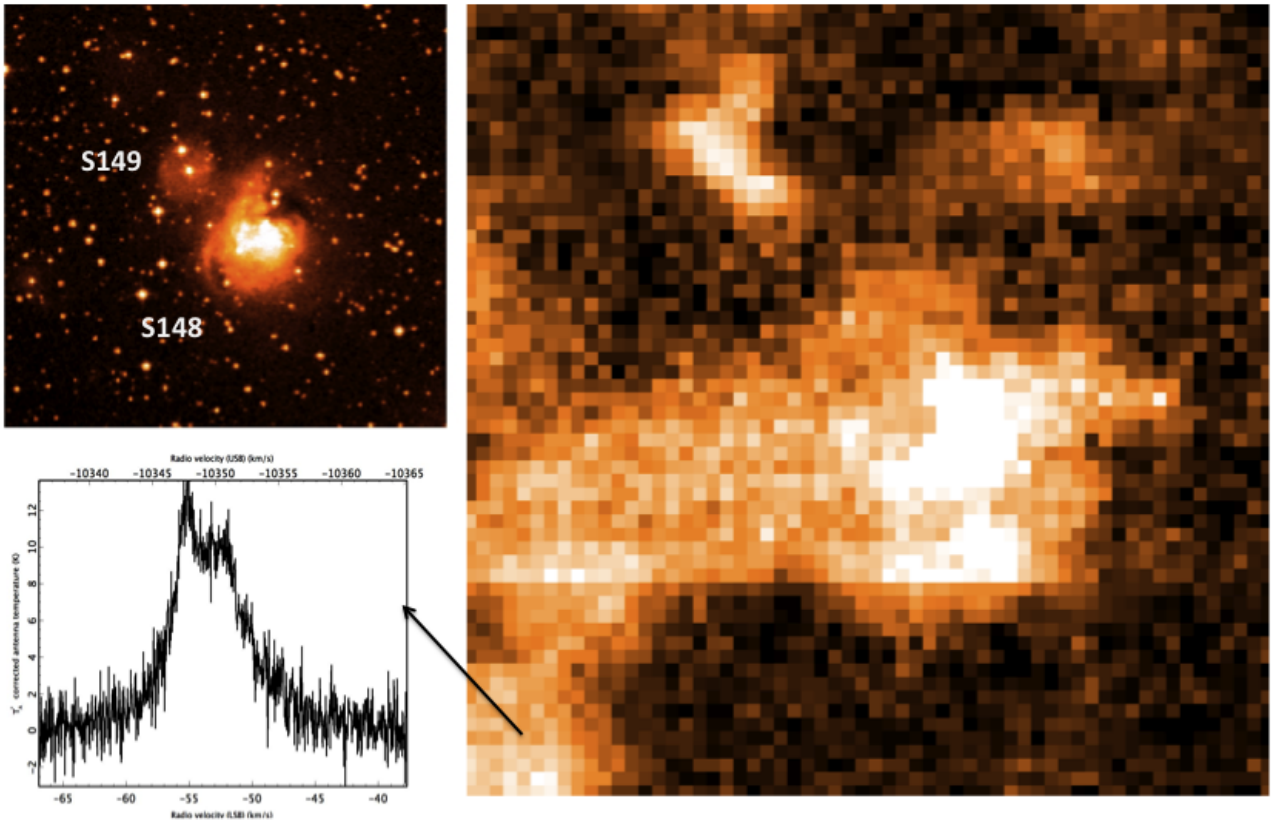

Figure A.2 : (right) $7' \times 7'$ map of S148/S149 in ^{12}CO(2-1) . The larger central clump is at the same position as S148 and probably in front of it. Two smaller clumps at the South-East (bottom-left) side of the map have broadened, double peaked line profiles. They are probably affected by the third component of this star-forming region, S147 which is out of this field but locate at the south-east.

A.3 S152

S152 is another component of the same star-forming region that contains S148/S149 . Figure A.3 shows the ^{12}CO(2-1) map (integrated between -45 and -58 km s^{-1}) and the DSS-2 red image of S152. The H II region is created by an O9V exciting star which is a member of rich stellar cluster (the near-IR image of cluster is presented in chapter 4). The mapped part of the cloud is not very fragmented and a weak ^{12}CO emission covers the whole field. Most of the identified clumps have a ^{12}CO peak in the range of -50 ± 2 km s^{-1}. All the line profiles are broadened and for some clumps like S152-C2 and S152-C3, shown in the picture, are double peaked or self-absorbed. S152-C5 is the hottest region in our map at the periphery of the H II region and probably warmed up by the ionized gas and radiations from the exciting star.

S152-C4 has the highest column density and line width in our map (N(H)$\sim$ 466×10^{20} cm^{-2} and $\Delta V_{12} = 7.42$ km s^{-1}). In a near-IR study by Romero & Cappa (2009) a deep young embedded cluster is identified at the position of S152-C4. The cluster is covered by a red nebula in their images. See chapter 4 for a reprint of the Romero & Cappa (2009) image and a detailed discussion about the detected stellar cluster.

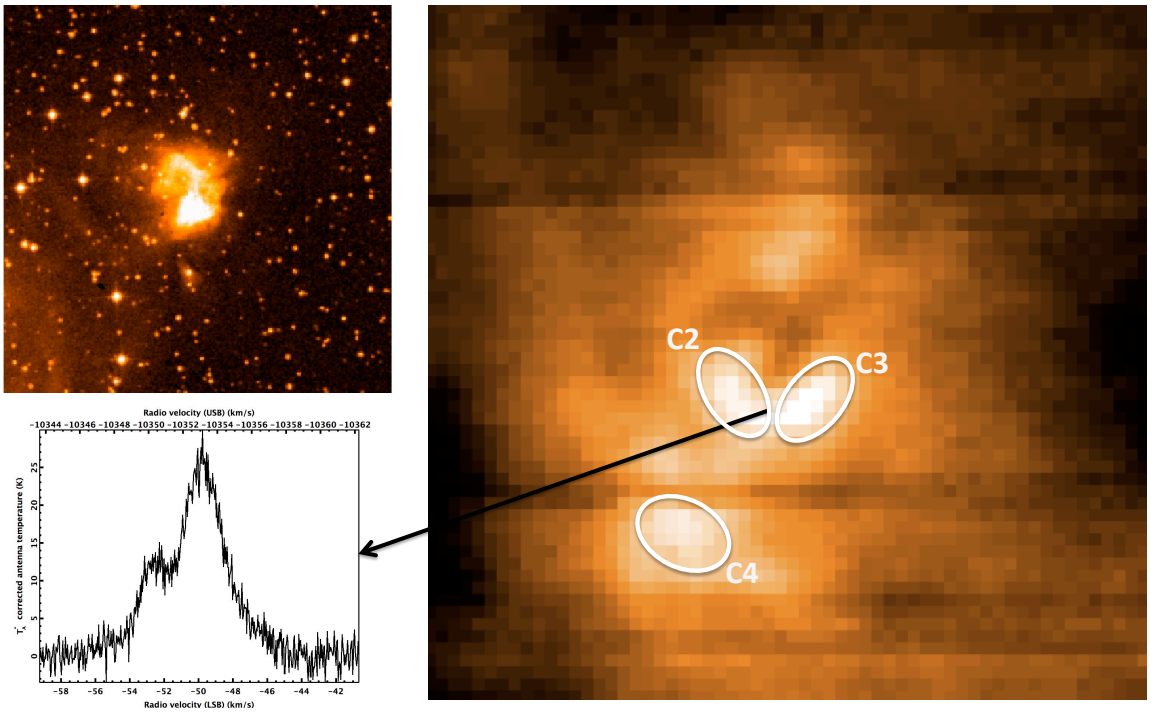

Figure A.3 : ^{12}CO(2-1) map of S152 (right) and the DSS-2 red image of the same field (left). S152-C2 and S153-C3, located at the edges of the H II region are the hottest clumps in our map and probably warmed up by the ionized gas and the O9V exciting star. The line emission over the map is very broad and for some clumps double peaked or self absorbed. S152-C4 has the largest line width and column density. A near-IR study shows a young embedded cluster within this clump.

A.4 S175

S175 is the closest source in our sample and we can therefore resolve smaller clumps within it. Two components, S175A and S175B, were selected within the molecular cloud associated with this H II region. S175A is adjacent to the ionized gas and influenced by the H II region and its exciting star, while S175B is too distant (10 times farther than the Stromgren radius of the H II region) to be affected. Figure A.4 shows the ^{12}CO contours of S175A and S175B, super-imposed on the IRAS 12μm image.

Figure A.5 shows the integrated ^{12}CO(2-1) maps (between -48 and -52 km s^{-1} for S175A and between -47 and -53 km s^{-1} for S175B). S175A is very fragmented, and as expected, has hotter clumps, warmed up by the ionized gas and the exciting star. S175B is less fragmented and a uniform gas with T$\approx$ 5-7 K covers the entire mapped field. The line profiles are also very broadened within S175B. Contrary to our expectation, S175A is a very quiescent region with relatively narrow line profiles, while S175B has active internal dynamics and appears very turbulent. In particular, three clumps, S175B-C1,C2,C3 within the rectangular marked in Figure A.5, had very wide double peaked line profiles. We made a sub-map in ^{12}CO(3-2) using HARP at JCMT to look for the source of turbulence in this region. A typical line profile for proto-stellar outflow was detected at the position of S175B-C1. The ^{12}CO(3-2) line profile shows a typical proto-stellar outflow, but the deep self-absorption at the middle of the emission line is unusual. Although it is far from the massive star

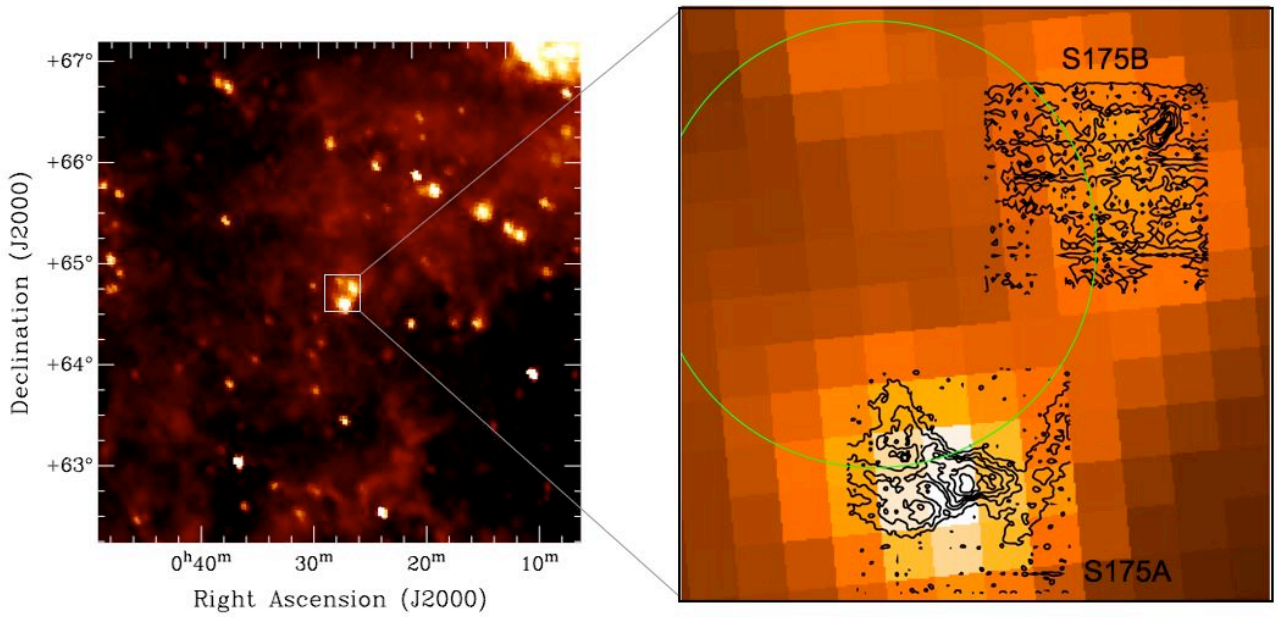

Figure A.4 : ^{12}CO(2-1) contours of S175A and S17B super-imposed on IRAS 12μm image. S175A is associated with the H II region and the brighter component in IRAS image. S175A has a filamentary structure and is fragmented. CO emission covers the entire field in S175B and the molecular gas in this region is less fragmented.

and the ionized gas, S175B is likely an active star-forming region. We have detected at least five very reddened point sources associated with S175B-C1, and an extended source in near-IR images at the position of the outflow and almost perpendicular to the outflow direction (image shown in chapter 4).

More details about the physical properties of S175A and S175B are discussed in chapter 2 (Paper I).

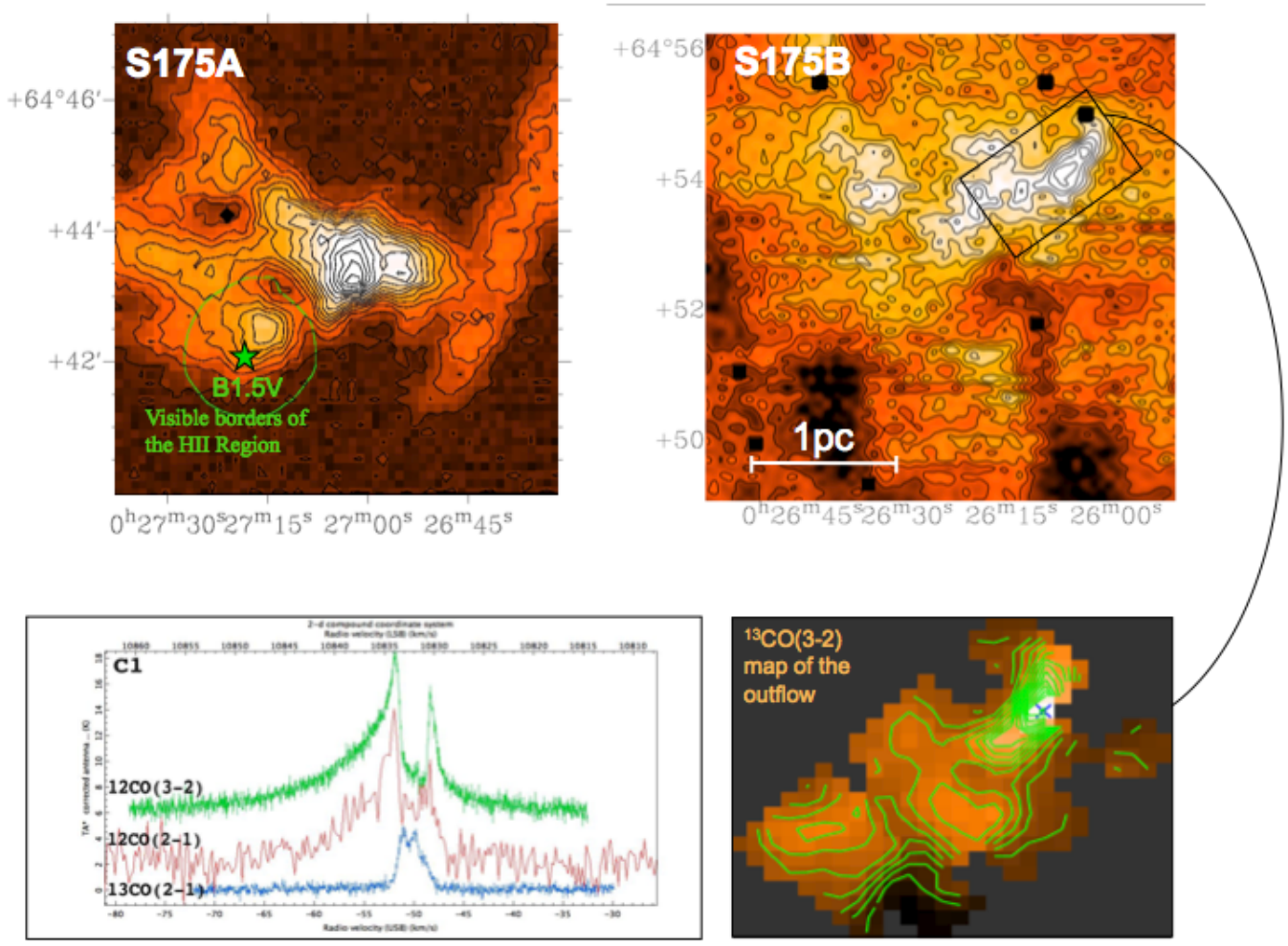

Figure A.5 : ^{12}CO(2-1) maps of S175A and S175B. S175A covers the H II region and therefore has a higher temperature, but the line profiles of the identified clumps within S175A are very sharp with small line widths. Contrarily, S175B has broadened, multiple peaked lines and is a dynamically active region. We looked for the source of turbulence by making a ^{12}CO(3-2) map of three more turbulent clumps, S175B-C1,C2,C3 (bottom-right). We found a proto-stellar outflow at the position of S175B-C1 with high self absorption.

A.5 S192/S193/S194

S192, S193 and S194 are three small adjacent H II regions (Figure A.6). S192 is excited by a B2.5V and S193 is excited by a B1.5V star (Russeil et al. 2007). No exciting star was found in the literature for S194. We have mapped the molecular cloud in between these three H II regions and have identified dense clumps along the edges of the H II regions. The molecular gas has been collected in dense shell around the ionized gas, but the average temperature and density are lower than in similarly mapped regions.

S192-C6, at the centre of the map, is surrounded and appears to be compressed by three expanding ionization fronts. Because of this, we expected to see a high temperature and density at this clump. S192-C6 is the hottest clump (T_{ex}=21.1 K) and has the larger line width (ΔV_{12}=3.45 km s^{-1}), but it is not as hot and dense as we expected compared to the other observed regions. A faint nebula is detected in near-IR (chapter 4) with finer structure within it, associated with S192-C6, but higher resolution and sensitivity is required to identify the nature of this object and its fine structure.

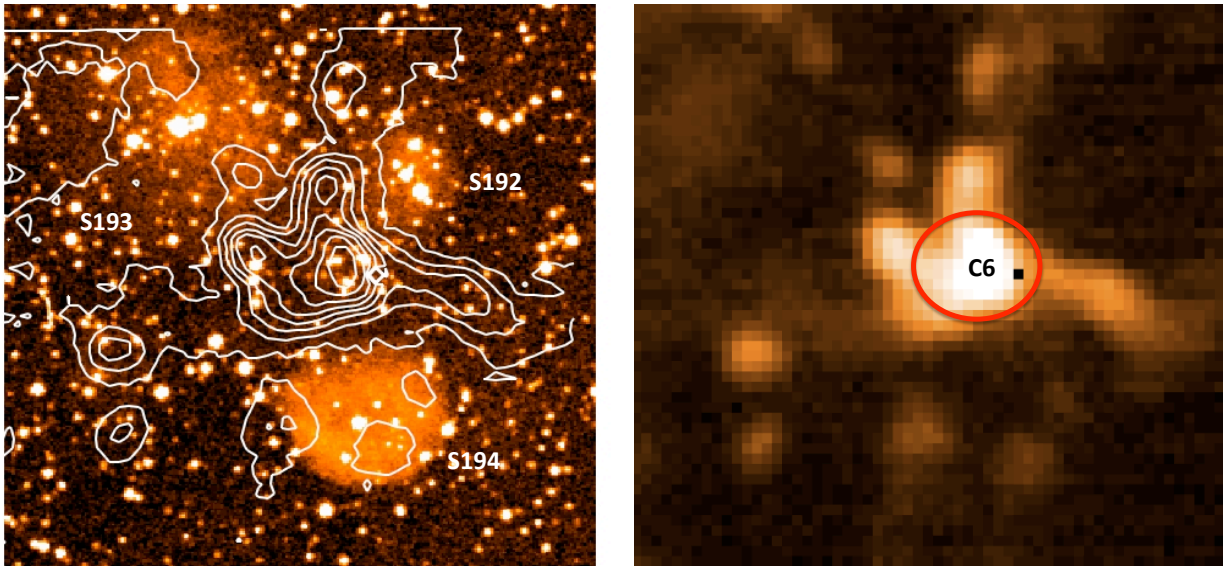

Figure A.6 : ^{12}CO(2-1) map of the gas surrounded by three H II regions (integrated between -42 and -47 km s^{-1}). The molecular gas has been swept up and collected in shells around the ionized gas. S192-C6 which is compressed by three ionized gas fronts has the highest temperature and density but still not very hot and dense compared to other regions in our sample.

A.6 S196

Figure A.7 shows the ^{12}CO(2-1) map integrated between -44 and -50 km s^{-1} and contours of ^{12}CO(2-1) super-imposed on the DSS-2 red image of the same field. The mapped region does not contain much molecular gas. S196-C1 and S196-C2 are the only large clumps, located at the south-east of the field. Even these two clumps are not very hot or dense. No exciting star has been identified in the literature for this spherical H II region. It is surprising that a massive star has been formed in isolation and not associated with a large molecular cloud.

There is a bright source detected in the IRAS 12μm image to the south of the H II region, but the resolution is very poor and not sufficient to recognize the structure of the cloud or investigate its association to the H II region. It seems informative to extend the ^{12}CO(2-1) map to the southern part to look for the origin of the massive star which excited S196. The mapped molecular gas has properties similar to those of S192/S193/S194 (V_{lsr} = -42 to -47 km s^{-1} for S196 and V_{lsr} = -44 to -49 km s^{-1} for S192-4) and might be related to the same complex. S196 might be a member of an evolved cluster that has originated in the same cloud.

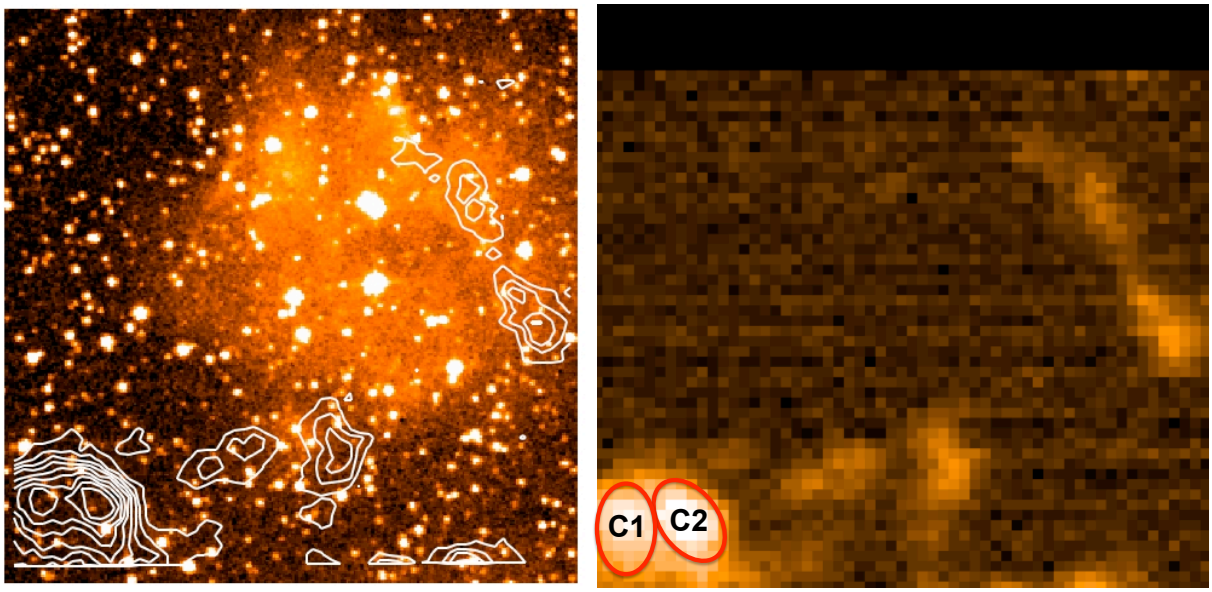

Figure A.7 : ^{12}CO(2-1) of S196 integrated between -44 and -50 km s^{-1} and the contours overlaid on DSS-2 red image of the same field. It is surprising that little molecular gas is associated with this H II region. No exciting star has been recognized in the literature. S196 might be an evolved region related to S192-4 complex.

A.7 S212

Figure A.8 presents the ^{12}CO(2-1) map integrated between -30 and -40 km s^{-1} and the CO contours overlaid on the DSS-2 red image of the same field. S212 is excited by an O6 star which is a member of a stellar cluster. S212 lies at the centre of a filament only half of which is shown in our map. The cloud has been completely mapped by Deharveng et al. (2008). They found that the ionized gas has expanded to the space beyond the molecular gas and has formed a Champagne flow[1]. They also suggest that S212 is a triggered star formation region through the "collect and collapse" process.

The molecular gas is swept and collected in shells by the expansion of the ionized gas. As expected, the temperature is higher in the clumps closer to the H II region. These clumps also have higher densities and multiple peaked line profiles. The peak emission line at S212-C1 is shown in Figure A.8. The double peaked line profile could be due to self absorption or could be a signature of infalling gas to the core. The double peaked profile, as seen in S104, might be due to the expansion of the gas which is less probable in the case of S212. Red-shifted and blue-shifted lines have been observed in this region which indicates an active internal dynamics. The eastern side of the cloud, which is distant from the H II region, is more uniform and less fragmented. The clumps have larger sizes but they are colder and less dense.

[1]If the ionized gas in an expanding H II region within a molecular cloud reaches the borders of the cloud, the ionized gas burst outward into the ISM; called the Champagne flow.

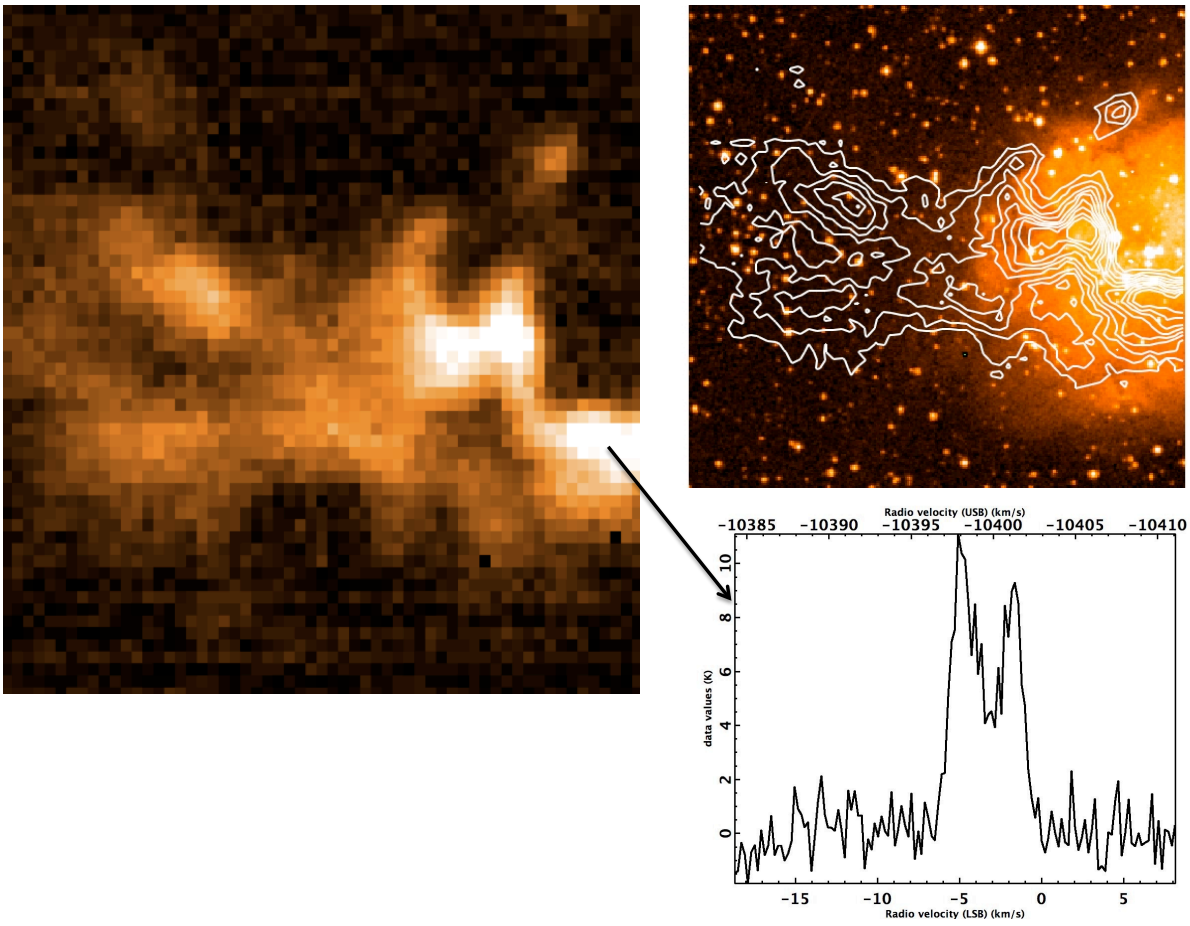

Figure A.8 : ^{12}CO(2-1) map of S212 (left) and the CO contours super-imposed on the DSS-2 red image of the same field (top right panel). Clumps closer to the H II region are more fragmented and have higher temperature and density. Double peaked line profiles, and red-shifted and blue-shifted lines indicate an active internal dynamics in this region.

A.8 S288

S288 is a small H II region at the centre of a filamentary molecular cloud (Figure A.9, integrated between 52 and 62 km s^{-2}). Like S212, it might have created a Champagne flow. The filament itself is not very fragmented. Only two dense clumps identified along the filament have different velocity ranges; S288-C1 emits between 52 and 58 km s^{-1} while S288-C2 appears between 56 and 60 km s^{-1}. While these two main clumps are slightly red-shifted and blue-shifted (relative to the central gas V_{LSR}), they do not have line profiles similar to an outflow. The two clumps seem to be parts of a bent filament. The line profile between the two clumps shown in Figure A.9 shows two components of the cloud.

S288 is excited by a B1 star which belongs to a stellar cluster. The cluster is shown in near-IR images from 2MASS in chapter 4.

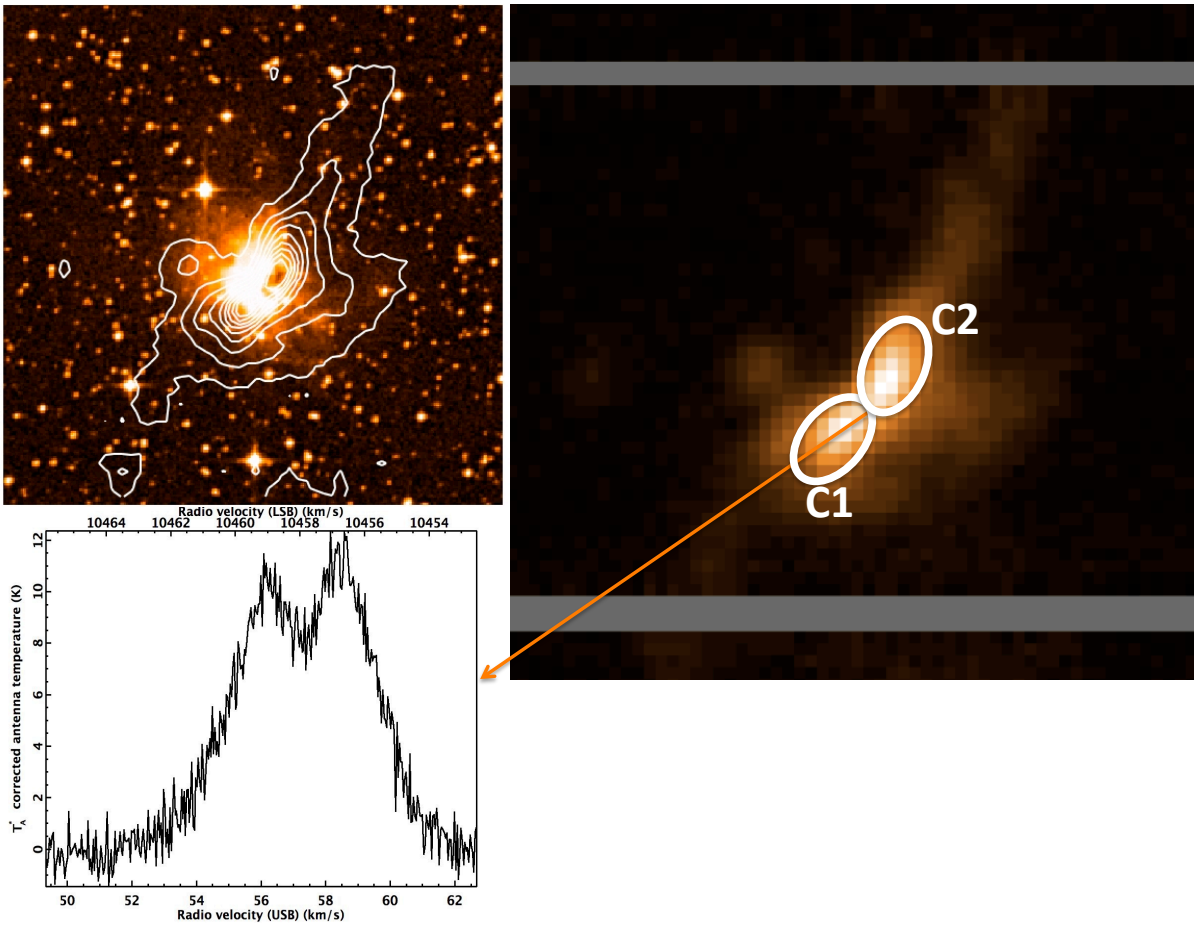

Figure A.9 : ^{12}CO(2-1) map of S288 (right) and the CO contours super-imposed on DSS-2 red image of the same field (upper-left). A filamentary structure from north-west to south-east is identified for the molecular cloud. Two main clumps S288-C1 and S288-C2 are slightly red-shifted and blue-shifted but their emission line profiles do not look like a proto-stellar outflow. They seem to be components of the bent centre of filament. The emission line profile between the two clumps shows the two components.

A.9 S305

Figure A.10 shows the ^{12}CO(2-1) map of S305 integrated between 40 and 50 km s^{-1}. S305 is another region that could be best explained by the collect and collapse model. Molecular gas appears to have been swept by the ionization fronts and collapsed in dense clumps. As expected these clumps have higher temperatures. S305-C7 at the west side of the map, is the hottest clump in our map with T_{ex}= 46.4 K. This is the only clump in the entire sample that we have detected CS(5-4) in it. Detection of this emission line indicates at least a density of 2.8×10^7 cm^{-3} (Evans 1999). S305-C7 is a good candidate for further massive star formation. The line profiles do not show multiple peaks or broadened lines. Many clumps within the S305 cloud are relatively quiescent, but hot and dense enough to be good signposts of further star formation. S305 is excited by an O9.5 star which belongs to a cluster. The cluster has been detected in near-IR data and is shown and discussed in chapter 4. More candidates of young stellar objects are also detected within S305.

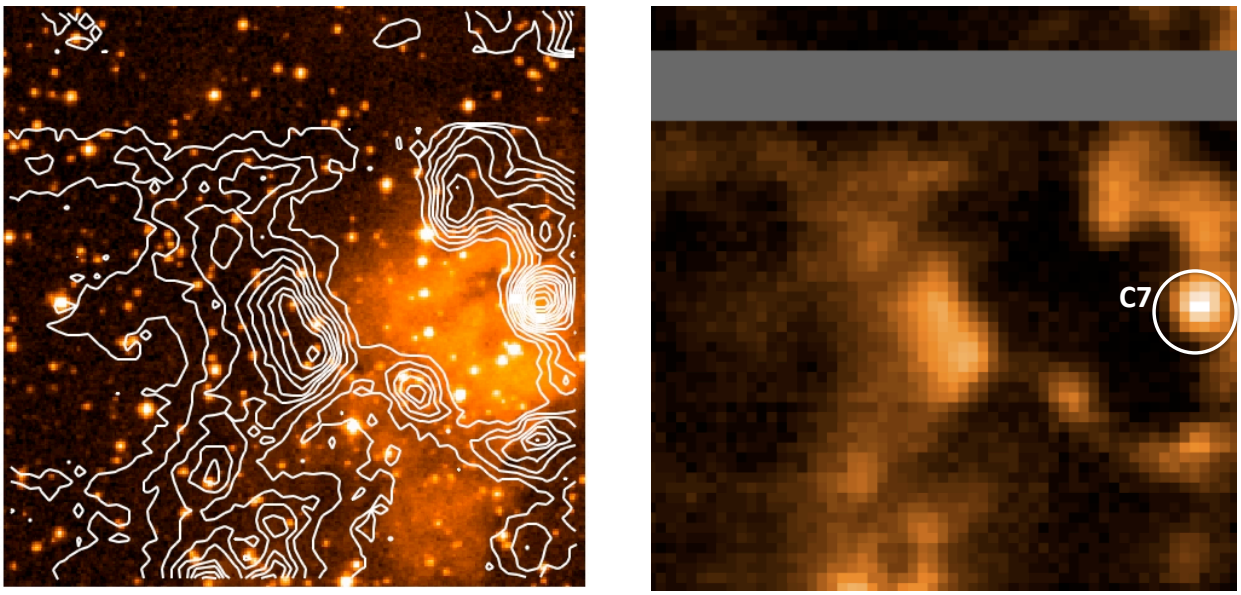

Figure A.10 : ^{12}CO(2-1) map of S305 (right) and the CO contours superimposed on DSS-2 red image of the same field (left). Molecular gas is collected along the borders of the H II region and has been collapsed in hot dense clumps. S305-C7, identified with a circle in right panel, is the densest clump with the highest temperature in our entire sample. This clump is a good candidate for more massive star formation.

A.10 S307

S307 has a bubbly structure as shown in the integrated ^{12}CO(2-1) map in Figure A.11. The cloud consists of two separated parts: a central bubble structured region and a compact region in the south-east. These two parts show a completely different velocity spectrum. It appears that the compact part is too distant (four times farther than the Stromgren radius) to be affected by the H II region. Evidence of expanding spheres is found in double peaked velocity lines with differences of ~ 3 km s^{-1}. Contrarily, the opposite sides of the compact part have almost the same velocity with a little blue or red excess. The spherical structure is more fragmented and ten clumps have been identified within this part of the cloud. A large expanding bubble (shown in Figure A.11) which probably has remained from an older generation of star formation, seems to have triggered a new generation of stars that have produced a second set of smaller expanding shells.

Most of the dense clumps are associated with the H II region and might be compressed by the fronts of the ionized gas. S307 is excited by an O9 star which lies within a stellar cluster. The cluster has been identified in near-IR images, but it seems to be old with evolved members. See chapter 4 for details of the stellar population within S307.

The line profiles are broadened and multiply peaked in S307. The bubbles

are expanding with a speed of ~ 3 km s^{-1}. S307-C4 noted in the Figure A.11 has a very different structure. It does not show the evidence of expansion, but has broadened red-shifted and blue-shifted line profiles that indicates a rotation within the clump. S305-C4 is the hottest clump in the map with T_{ex}= 36.1 K. It also has the highest column density and line width (N(H)= 400×10^{20} cm^{-2} and $\Delta V_{12} = 3.35$ km s^{-1}). S305-C7 is a good candidate to start star formation. An embedded cluster has been identified in near-IR images associated with this clump. See chapter 4 for details about the stellar population in S307.

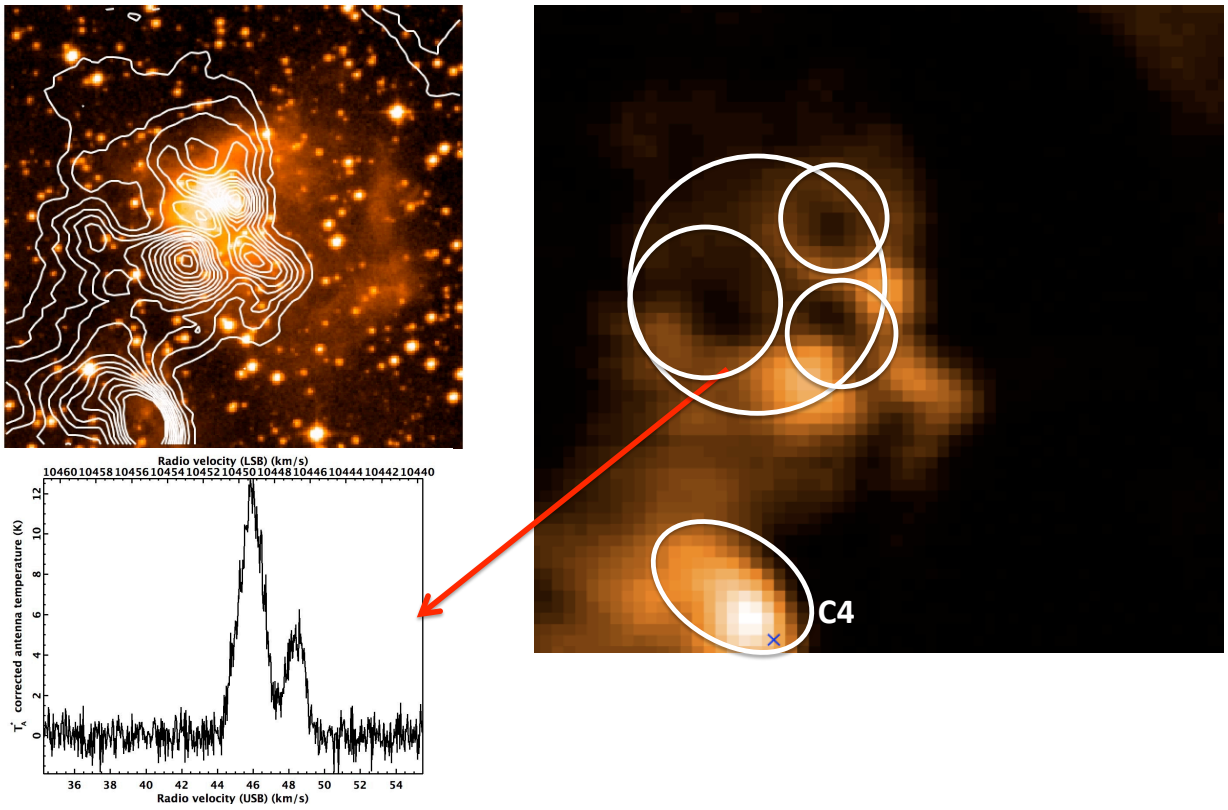

Figure A.11 : ^{12}CO(2-1) map of S307 (right) and the CO contours superimposed on DSS-2 red image of the same field. S307 is a bubbly structure and seems to have a second generation of triggered stars. The bubbles are expanding with a velocity of ~ 3 km s^{-1}. S307-C4 is the hottest clump in the map; it has a different structure and a good candidate to start star formation.

Appendix B

Declaration

Chapters 2 and 3 of this thesis are reprints of the original papers written by Mohaddesseh Azimlu. Chapter 2 was published in the Astronomical Journal in June 2009 and chapter 3 is ready to submit. The papers have been reformatted slightly to fit in the required thesis style.

The first part of the data (six CO maps) presented in this thesis and a part of pointed observations in the first observing run were taken by Michel Fich in 1998 and 2005. The rest of observations are the original work of the author. Data were taken during several observing runs from August 2005 to January 2009. I was the Principal Investigator on the proposals which I prepared under supervision of Dr. Fich for the JCMT observing time.

The first paper (chapter 2) is originally written by the author in consultation with Dr. Fich and Dr. Carolyn M^{c}Coey. The paper was edited in several

drafts by these co-authors. Paper II (chapter 3) is written originally by the author in consultation with Dr. Fich and edited in several drafts by him. The Monte Carlo code to simulate the temperature versus projected distances from a heating source in Paper II is the only component of the paper originally done by Dr. Fich, although I run the code for several initial conditions and show the results as plots here in this thesis.

Bibliography

[1] 2MASS All Sky Catalog of point sources.

Cutri, R. M., Skrutskie, M. F.; van Dyk, S., Beichman, C. A., Carpenter, J. M., Chester, T., Cambresy, L., Evans, T., Fowler, J., Gizis, J., Howard, E.; Huchra, J., Jarrett, T.; Kopan, E. L., Kirkpatrick, J. D., Light, R. M.; Marsh, K. A., McCallon, H., Schneider, S., Stiening, R., Sykes, M., Weinberg, M., Wheaton, W. A., Wheelock, S., Zacarias, N., 2003

The IRSA 2MASS All-Sky Point Source Catalog, NASA/IPAC infrared Science Archive: http://irsa.ipac.caltech.edu/applications/Gator/

[2] Alves J., Lombardi M., & Lada C. J., 2006, A&A, 462L,17

[3] Azimlu M., Fich M., & M^{c}Coey C., 2009, AJ, 137, 4897 (Paper I)

[4] Balog Z., Kenyon S. J., Lada E. A., Barsony M., Vinkó J. & Gáspár A., 2004, AJ, 128, 2942

[5] Banerjee, R., Pudritz, R. E., Holmes L., 2004, MNRAS, 355, 248

BB2005 Bate M.R, Bonnell I.A, 2005 MNRAS, 356, 1201

[6] Bell T.A., Roueff E, Viti S., & Williams D.A., 2006, MNRAS, 371, 1865

[7] Blitz L., Fich M., & Stark A.A., 1982, ApJS, 49, 183

[8] Bok, B. J., Reilly, E. F. 1947, ApJ, 105, 255

[9] Boldyrev S., 2002, ApJ, 569, 841

[10] Bonnell I. A., Bate M. R., Zinnecker H., 1998, MNRAS, 298, 93

[11] Bonnor, W. B. 1956, MNRAS, 112, 195

[12] Brand J., Cesaroni R., Palla F., & Molinari S., 2001, A&A, 370, 230

[13] Brand, J., & Wouterloot, G.J.A., 1998, A & A, 337, 539

[14] Caplan, J., Deharveng, L., Pena, M., Costero, R., and Blondel, C., 2000, MNRAS, 311, 317

[15] Casseli P., Myers P.C., 1995, ApJ, 446, 665

[16] Carpenter J. M., 2000, AJ, 120, 3139

[17] Chan G., Fich M., 1995 AJ, 109, 2611

[18] Chen Y., Yao Y., Yang J., Zeng Q., & Saito S., 2009, ApJ, 693, 430

[19] Comeron F, Pasquali A., 2005, A&A, 430, 541

[20] Dale J.E., Bonnell I. A., Whitworth A. P., 2007, MNRAS, 375, 1291

[21] Dapp W. B., Basu S., 2009, MNRAS, 395, 1092

[22] Deharveng L., Lefloch B., Zavagno A., Caplan J., Withworth A.P., Nadeau D., & Martin S., 2003 A & A, 408L, 25

[23] Deharveng L., Zavagno A., and Caplan J., 2005, A & A, 433, 565

[24] Deharveng L., Lefloch B., Kurtz S., Nadeau D., Pomares M., Caplan J., and Zavagno A., 2008, A & A, 482, 585

[25] Deharveng L., Zavagno A., Schuller F., Caplan J., Pomares M., De Breuck C., 2009, A & A, 496, 177

[26] Dobashi K., Yonekura Y., Matsumoto T., et al., 2001, PASJ, 53, 85

[27] Draine B.T., 2003, ARAA, 41, 241

[28] Ebert, R. 1955, Z. Astrophys., 37, 217

[29] Elmegreen B.G., & Lada C.L., 1977, ApJ, 214, 725

[30] Elmegreen B. G., 2000, ApJ, 539, 342

[31] Evans N. J., 1991, ASPC, 20, 45

[32] Evan N. J., 1999, ARAA, 37, 311

[33] Ferriere K.M., 2001, RevModPhys, 73, 1031

[34] Fich M., Treffers R.R., and Dahl G.P., 1990, AJ, 99, 622

[35] Hartigan, P., Edwards, S., Ghandour, L. 1995, ApJ, 452, 736

[36] Heydari-Malayer M., & Testor G., 1981, A & A, 96, 219

[37] Heyer M.H., Brunt C., Ronald L., Snell R. L., Howe J E., and Schloerb F. P., 1998, ApJS, 115, 258

[38] Holmgren D., Hadrava P., Harmenec P., Koubsky P., & Kubat J., 1997, A & A, 322, 565

[39] Hunter D. A., Harley A., Thronson J_R & Wilton C., 1990, AJ, 100, 1915

[40] Isobe T., Feigelson E. D., Akritas A. G., & Babu G. J., 1990, ApJ, 364, 104

[41] Jorgenssen J. K., Johnstone D., Kirk H., Myers P. C., Allen L. E. & Shirley Y. L., 2008 ApJ , 68, 822

[42] Kerton C.R., Arvidsson K., Knee L.B.G. and Brunt C., 2008, MNRAS, 385, 995

[43] Khanzadyan T., Smith M. D., Gredel R., T. Stanke T. & Davis C. J., 2002, A&A 383, 502

[44] Kim K.T., & Koo B. C. 2003, ApJ, 596, 362

[45] Kirsanova M.S., Sobolev A.M., Thomson M., Wiebe D.D.,Johnsson L.EB. and Seleznev A.F., 2008, MNRAS 388, 729

[46] Kobayashi N., Yasui C., Tokunaga A. T., Saito M., 2008, ApJ, 386, 178

[47] Koorneef J., 1983, A & A, 128, 84

[48] Krco M., Goldsmith P.F., Brown R. L., and Li D., 2008, ApJ, 689, 276

[49] Kroupa P., 2001, NRAS, 322, 231

[50] Krumholz M. R., McKee C., & Klein R. I., 2005, ApJ, 618, 757

[51] Krumholz M. R., 2006a, ASP Con. Ser. 352, Frank N. Bash Symposium 2005: New Horizons in Astronomy, ed. Kannappan, S. J., Redfeild, S., Kessler-Silacci J. E., Landriau M., & Dory N.

[52] Krumholz M. R., McKee C., & Klein R. I., 2006b, ApJ, 638, 369

[53] Krumholz M. R., Klein R. I., & McKee C. F., 2007, ApJ, 659, 959

[54] Lada, C.J., & Wooden, D., 1979, ApJ , 232, 158

[55] Lada E. A., DePoy D.L., Evans J.H., Gatley I. 1991, ApJ, 371, 171

[56] Lada E. A., Evans N. J., & Falgarone E., 1997, ApJ, 488, 286

[57] Lada C. J., Lada E. A., 2003, ARAA, 41, 57

[58] Langer W.D., Penzias A.A, 1993, ApJ, 408, 539

[59] Larson, R. B. 1981, MNRAS, 194, 89

[60] Larson R. B., 2005, ASSL, 327, 329

[61] Launhardt R., Evans N. J., Wang Y. S., Clemens D. P., Henning T., Yun J., 1998, ApJS, 119, 59

[62] Leisawitz D., Bash F. N., & Thaddeus P., 1989, ApJS, 70, 731

[63] Li W., Evans N. J. & Lada E. A., 1997 ApJ, 488, 277

[64] Li P. S., Norman M. L., Mac Low M., & Heitsch, F. 2004, ApJ, 605, 800

[65] Massey P., 1998, ASP Conf. Ser. 142: The Stellar Initial Mass Function (38th. Herstmonceux Conference), ed. G. Gilmore & D. Howell, 17

[66] Matzner D. C., 2007, ApJ, 659, 1394

[67] McKee C. F. & Tan J. C., 2003, ApJ, 585, 850

[68] MacLaren A., Richardson K.M., and Wolfendale A.W., 1988, ApJ, 333, 821

[69] Miller G. E., Scalo J. M., 1979, ApJS, 41, 513

[70] Moffat, A.F.J., FitzGerald, M.P., and Jackson, P.D., 1997, A&A. Suppl. 38, 197

[71] Moriarty-Schieven G. H., Johnstone D., Bally J. & Jennes T., 2006, ApJ, 645, 357

[72] Muench, A. A., Lada, E. A. & Lada, C. J., 2000, ApJ, 533, 358

[73] Myers P. C., Mardones D., Tafalla M., Williams J. P., & Wilner D. J., 1996, ApJ, 465, L133

[74] Onishi T., Mizuno A., Kawamura A., Ogawa H., Fukui Y., 1998, ApJ, 502, 296

[75] Padoan, P., & Nordlund, A., 1999, ApJ, 526, 279

[76] Pineda J. E., Caselli P., Goodman A. & Alyssa A., 2008, ApJ, 679, 481

[77] Plume R., Jaffe D. T., Evans N. J., Martin-Pintado J., and Gomez-Gonzalez J. 1997, apj, 476, 730

[78] Pomars, M.; Zavagno, A.; Deharveng, L.; Cunningham, M.; Jones, P.; Kurtz, S.; Russeil, D.; Caplan, J.; Comern, F., 2009, A& A, 494, 987

[79] Pismis P., & Mampos A., 1991, MNRAS, 249, 385

[80] Ragan S. E., Bergin E. A., Plume R., Gibson D. L. , Wilner D. J., O'Brien S. & Hails E., 2006, ApJS, 166, 567

[81] Reid M. A., Wilson, C. D. 2005, ApJ, 625, 891

[82] Reid M. A., Wilson, C. D. 2006, ApJ, 650, 970

[83] Reipurth, B. Bally, J. 2001, ARAA, 39, 403

[84] Ridge N. A., Di Francesco J., Kirk H., and the X team, 2006, AJ , 131, 2921

[85] Rohlfs, K., & Wilson, T.L. 2004, Tools of Radio Astronomy (Springer-Verlag, Berlin-Heidelberg)

[86] Roman-Lopes A., 2009arXiv0905.3822R

[87] Romero G.A., & Cappa C.E., MNRAS, 395, 2095

[88] Russeil D., Adami C., and Georgelin Y.M., 2007, A & A, 470, 161

[89] Saito H, Saito M., Moriguchi Y., Fukui Y., 2006, PASJ, 58, 343

[90] Saito H., Saito M., Sunada K., Yonekura Y., Nakamura F., 2008, ApJS, 178, 302

[91] Saito H., Saito M., Yonekura Y., 2007, ApJ, 659, 459

[92] Scaife A.M.M, et al., 2008, MNRAS , 385, 809S

[93] Scalo J., 1998, ASPC, 142, 201

[94] Scoville N.Z., Yun, M.S., Clemens, D.P., Saders, D.B., and Waller, W.H., 1987, ApJS, 63, 821

[95] Sharpless S., 1959, ApJS, 6, 257

[96] Shu F. H., 1977, ApJ, 214, 488

[97] Shu F.H., Adams F.C., Lizano S., 1987, ARAA, 25, 23

[98] Simon, R., Jackson J. M., Clemens, D. P., Bania, T. M & Heyer, M. H., 2001, ApJ, 551, 747

[99] Smith, R.J.; Longmore, S; Bonnell, I, 2009, MNRAS, 400, 1775

[100] Snow T. P., & and McCall B. J., 2006, ARAA, 44, 367

[101] Solomon, P. M., Rivolo, A. R., Barret, J., & Yahil, A. 1987, ApJ, 319, 730

[102] Stahler S.W. & Palla F. 2004, The formation of Satrs, (WILEY-VCH Verlag)

[103] Strong A., Mattox J.R., 1996, A & A, 308 ,L21

[104] Tachihara K., Onishi T., Mizuno A., Fukui Y., 2002, A&A 385, 909

[105] van den Bergh S., McClure R. D., 1980, A & A, 88, 360

[106] Whitworth A. P., Bhattal A. S., Chapman S. J., Disney M. J., Turner J. A., 1994, MNRAS, 268, 291

[107] Wouterloot J.G.A., and Habing H.J., 1985, A & A, 151, 297

[108] Yamamoto H., Onishi T., Mizuno A., & Fukui, Y., 2003, ApJ, 592, 217

[109] Yamamoto H., Kawamura A., Tachihara K., Mizuno N., Onishi T., Fukui Y., 2006, ApJ, 642, 307

[110] Zavagno, A., Deharveng, L., Comeron, F. et al. 2006, A & A, 171, 184

[111] Zuckerman, B., & Evans, N. J., 1974, ApJ, 192, L149